AFRL-AFOSR-VA-TR-2023-0388

3D laser absorption imaging of species and temperature in supercritical flames

Spearrin, Raymond
UNIVERSITY OF CALIFORNIA LOS ANGELES
11000 KINROSS AVE STE 102
LOS ANGELES, CA,
US

07/10/2023
Final Technical Report

Air Force Research Laboratory
Air Force Office of Scientific Research
Arlington, Virginia 22203
Air Force Materiel Command

REPORT DOCUMENTATION PAGE

PLEASE DO NOT RETURN YOUR FORM TO THE ABOVE ORGANIZATION.

1. REPORT DATE	2. REPORT TYPE	3. DATES COVERED	
20230710	Final	START DATE 20190215	END DATE 20230214

4. TITLE AND SUBTITLE
3D laser absorption imaging of species and temperature in supercritical flames

5a. CONTRACT NUMBER	5b. GRANT NUMBER	5c. PROGRAM ELEMENT NUMBER
	FA9550-19-1-0062	61102F
5d. PROJECT NUMBER	**5e. TASK NUMBER**	**5f. WORK UNIT NUMBER**

6. AUTHOR(S)
Raymond Spearrin

7. PERFORMING ORGANIZATION NAME(S) AND ADDRESS(ES)
UNIVERSITY OF CALIFORNIA LOS ANGELES
11000 KINROSS AVE STE 102
LOS ANGELES, CA
US

8. PERFORMING ORGANIZATION REPORT NUMBER

9. SPONSORING/MONITORING AGENCY NAME(S) AND ADDRESS(ES)	10. SPONSOR/MONITOR'S ACRONYM(S)	11. SPONSOR/MONITOR'S REPORT NUMBER(S)
Air Force Office of Scientific Research 875 N. Randolph St. Room 3112 Arlington, VA 22203	AFRL/AFOSR RTA1	AFRL-AFOSR-VA-TR-2023-0388

12. DISTRIBUTION/AVAILABILITY STATEMENT
A Distribution Unlimited: PB Public Release

13. SUPPLEMENTARY NOTES

14. ABSTRACT
The primary research objective of this project was to enable and apply a novel three-dimensional, quantitative imaging technique for species and temperature in high-pressure reacting flows. We proposed to achieve this objective via two advancements in laser diagnostics. First, we focused on expanding state-of-the-art laser absorption spectroscopy (LAS) methods in spatial resolution capability by utilizing high-speed infrared cameras to image flow fields backlit with tunable infrared laser radiation. The laser absorption imaging (LAI) technique provides for spectrally, spatially, and temporally rich datasets that can be reconstructed using tomographic methods. Second, we exploit the vibrational band and cluster narrowing effects of line mixing at high gas densities to extend laser absorption spectroscopy to pressures up to 100 atm for multiple combustion species. In this project, we work on both methods in parallel and aim to combine the novel imaging and high-density spectroscopic strategy for simultaneous measurements of both flame structure and quantitative thermochemistry (temperature, species concentrations) at extreme conditions, providing unique capability that does not exist with established diagnostic methods. In total, this project resulted in 10 peer-reviewed journal articles that reflect a progressive increase in dimensionality of the LAI method, integrated advances in data science and image processing, and spectroscopic studies at high pressures and temperatures. This report highlights the technical work primarily from the final year of the YIP award (other works were highlighted in prior progress reports). We built on the prior years to make progress on the two research fronts (laser absorption imaging and high-pressure spectroscopy) as described in this report.

15. SUBJECT TERMS

16. SECURITY CLASSIFICATION OF:			17. LIMITATION OF ABSTRACT	18. NUMBER OF PAGES
a. REPORT	b. ABSTRACT	c. THIS PAGE		
U	U	U	UU	52

19a. NAME OF RESPONSIBLE PERSON	19b. PHONE NUMBER *(Include area code)*
CHIPING LI	426-8574

Standard Form 298 (Rev.5/2020)
Prescribed by ANSI Std. Z39.18

Final Performance Report – AFOSR Young Investigator Program (YIP)

Title: 3D laser absorption imaging of species and temperature in supercritical flames
PI: R. Mitchell Spearrin (UCLA)

Abstract

The primary research objective of this project was to enable and apply a novel three-dimensional, quantitative imaging technique for species and temperature in high-pressure reacting flows. We proposed to achieve this objective via two advancements in laser diagnostics. First, we focused on expanding state-of-the-art laser absorption spectroscopy (LAS) methods in spatial resolution capability by utilizing high-speed infrared cameras to image flow fields backlit with tunable infrared laser radiation. The laser absorption imaging (LAI) technique provides for spectrally, spatially, and temporally rich datasets that can be reconstructed using tomographic methods. Second, we exploit the vibrational band and cluster narrowing effects of line mixing at high gas densities to extend laser absorption spectroscopy to pressures up to 100 atm for multiple combustion species. In this project, we work on both methods in parallel and aim to combine the novel imaging and high-density spectroscopic strategy for simultaneous measurements of both flame structure and quantitative thermochemistry (temperature, species concentrations) at extreme conditions, providing unique capability that does not exist with established diagnostic methods. In total, this project resulted in 10 peer-reviewed journal articles that reflect a progressive increase in dimensionality of the LAI method, integrated advances in data science and image processing, and spectroscopic studies at high pressures and temperatures. This report highlights the technical work primarily from the final year of the YIP award (other works were highlighted in prior progress reports). We built on the prior years to make progress on the two research fronts (laser absorption imaging and high-pressure spectroscopy) as will be described in this report.

1. 3D Laser Absorption Imaging with Deep Learning

1.1. Introduction

Laser absorption tomography (LAT) enables quantitative, spatially-resolved temperature and species measurements in reacting flows via the inversion of spectrally-resolved, line-of-sight integrated data [1]. Unfortunately, in non-axisymmetric, three-dimensional flow-fields, the inversion problem is typically ill-posed [2] due to practical limitations in optical access that yield sparse view angles [3, 4]. Solution methods for these ill-posed parameter estimation problems can be assisted by incorporating prior information about the flows [5] to facilitate reconstruction, either explicitly via linear regularization [6, 7, 8, 9, 10, 11] or Bayesian inference [12, 13, 14], or implicitly by assuming a simplified form of the parameter distribution to reduce the degrees-of-freedom in the problem [15, 16, 17]. As considerable physical information is typically known a priori about a reacting flow field of interest, it is desirable to integrate this information in the solution method to improve efficiency and accuracy.

In recent years, deep neural network (DNN) models have emerged as an alternative approach to the inversion problem, as they are efficient in capturing complex non-linear relationships, such as between species thermochemical properties and their associated spectra. A distinction in this approach is that priors are effectively introduced via the neural network training process which reflects a forward model of the projection measurement, introducing input-output pairs to train an implicit functional relationship [18, 19]. DNNs have been applied in both emission spectroscopy [20, 21, 22, 23] and laser

absorption tomography to predict species fields in dynamic flows using multiple beam configurations with varying view angles [24, 25, 26]. Previous learning-based absorption tomography studies have employed relatively simple stable distributions (e.g. Gaussian) in training data to represent absorption fields [24, 26, 25, 27]. However, such generic field distributions are inadequate representations of many reacting flow-field parameters such as intermediate species or gas temperature. These parameters require commensurate training fields that reflect the physics involved.

In this study, we integrate a mid-fidelity reacting fluid dynamic simulation into the forward model to capture end-to-end physics and generate projected absorption fields to train a deep neural network a priori, independent of flow-field measurements; allowing for incorporation of thermochemistry and transport properties that govern temperature and species distributions. We then apply this neural network to invert multi-angle 2D laser absorption images of a 3D reacting flow (doublet laminar flame) to quantitatively measure temperature and species fields. We first describe the deep learning method as coupled to the unique volumetric laser absorption imaging (LAI) optical setup. We then detail the training process and evaluate predictive capability through numerical simulation and experiment. Reconstructed or predicted fields of CO mole fraction and temperature are compared between the deep learning method and linear tomography with various numbers of projection angles in terms of accuracy, artifacts, and computational efficiency.

1.2. Methods

1.2.1. Volumetric laser absorption imaging

Here, we employ laser absorption imaging (LAI), a diagnostic method that produces spatio-temporally rich absorption datasets by capturing flows backlit by tunable laser radiation [28, 29] with a high-speed camera (Telops FAST-M3K), as shown in Fig. 30. Volumetric LAI involves the collection of 2D images at multiple angles, readily yielding thousands of unique lines of sight [30] that help constrain the 3D reconstruction of flow-field parameters with steep spatial gradients, as in the reaction zone of

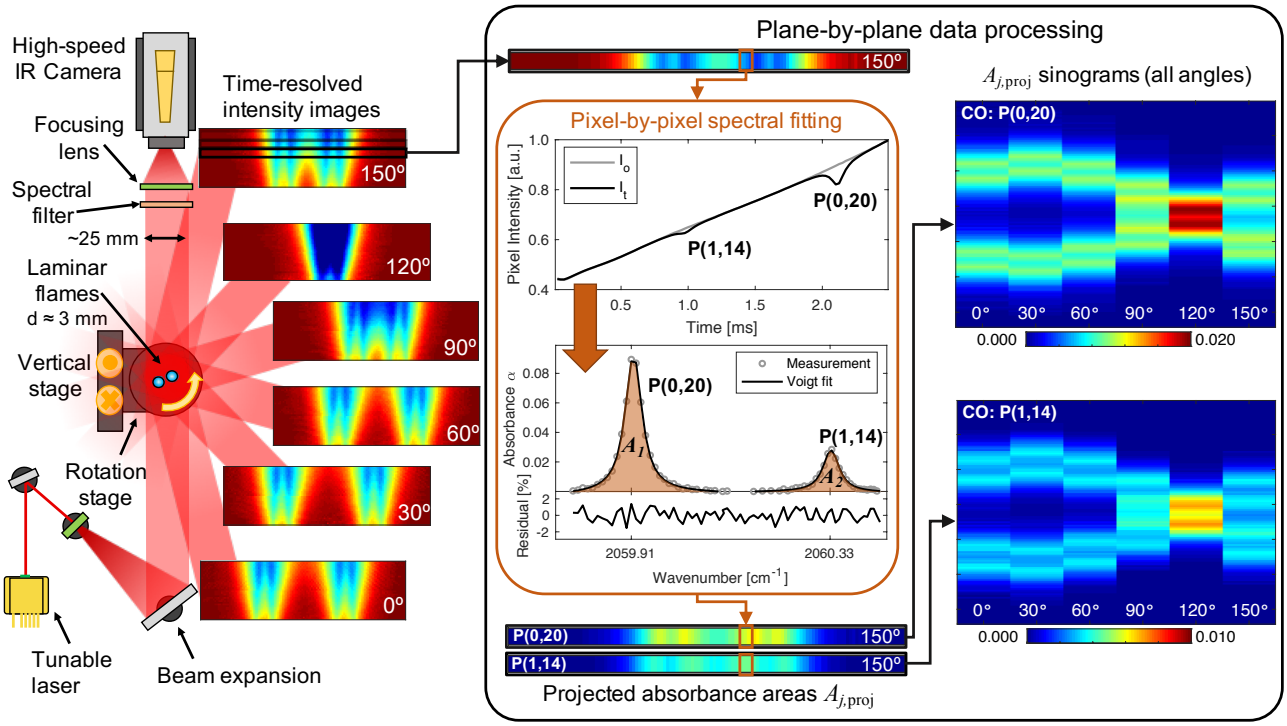

Figure 1 – *Left:* Optical arrangement and transmission images at varying rotation angles of Bunsen-style flames. *Right:* Flow chart of plane-by-plane processing, including incident (I_o) and transmitted (I_t) pixel intensity, spectral absorbance, Voigt fits, projected absorbance areas $A_{j,\mathrm{proj}}$, and resulting sinograms of $A_{j,\mathrm{proj}}$ for every angle.

small-diameter (<1 cm) flames.

In this configuration, we target carbon monoxide mole fraction and temperature with a distributed feedback (DFB) quantum cascade laser (QCL) near 4.85 μm that is spectrally scanned across the P(0,20) and P(1,14) rovibrational transitions in the fundamental band of CO in the mid-wave infrared [31]. The beam is horizontally expanded with a cylindrical lens and re-collimated with a concave mirror, then pitched through the flow-field comprising two Bunsen-style flames, each with flame brushes approximately 3 mm in diameter. The beam is spectrally isolated with a bandpass filter (4860 ± 96 nm), and a plano-convex lens focuses the expanded beam onto the detector array of the camera. The camera detector subwindow of size 128×24 captures the beam with a frame rate of 40 kHz and integration time of 5 μs. The QCL is injection-current tuned with a 400 Hz sawtooth waveform, resulting in 100 points per scan for subsequent spectral fitting, shown in the center of Fig. 30. The dual flame assembly is mounted on a rotational and vertical translation stage to capture multiple projection angles and heights for the tomography. 2D $A_{j,\text{proj}}$ images were collected at up to 11 different projection angles, yielding an aggregate of up to 50,688 unique lines of sight capturing the scene with a pixel resolution of approximately 70 μm, evaluated by imaging a wire mesh backlit with laser radiation [29]. Mass flow controllers (MKS MFC GE50A) supply reactants with overall flow rates of 128 sccm C_2H_4, 79 sccm N_2, and 101 sccm O_2, resulting in a fuel/oxidizer equivalence ratio of $\phi = 3.80 \pm 0.07$. After the tubing is split to the two burners, one flow is measured with a rotameter to ensure equal flow through each burner. The exit velocity of each flow is 0.41 m/s and the jet exits of the stainless steel burners are 1.6 mm in diameter, providing a laminar jet Reynolds number of ~44.

For each projection angle measurement, incident (I_0) and transmitted (I_t) intensity data is collected and averaged over 1 s (400 scans), an interval over which the flames are assumed steady. For a non-uniform gas medium, the Beer-Lambert law integrated over wavenumber ν [cm^{-1}]—or the projected absorbance area $A_{j,\text{proj}}$ [cm^{-1}]—can be expressed for each line-of-sight with pathlength L [cm] and related to thermodynamic gas properties in Eq. 1 [32],

$$A_{j,\text{proj}} = \int_{-\infty}^{\infty} \alpha(\nu) d\nu = \int_{-\infty}^{\infty} -\ln\left(\frac{I_t}{I_0}\right)_\nu d\nu = \int_0^L K_j dl = \int_0^L P S_j(T) X_{\text{abs}} dl \tag{1}$$

where $\alpha(\nu)$ is spectral absorbance and the thermochemical properties of interest are embedded in the spatially-resolved absorption coefficient K_j [cm^{-2}]. Total pressure P [atm] is assumed 1 atm, $S_j(T)$ [cm^{-2}/atm] is the linestrength of transition j at temperature T [K], and X_{abs} is the mole fraction. Each horizontal row of pixels can be treated independently for tomographic reconstruction, and the data are spectrally-fitted for every pixel at every angle, producing plane-by-plane sinograms of $A_{j,\text{proj}}$ for each transition j, as shown in the right of Fig. 30. These experimentally measured sinograms can then be used to reconstruct 2D fields of K_j and/or temperature and mole fraction, as discussed in the next section.

1.2.2. Tomographic inversion

We employ two approaches to the reconstruction process of LAI data, as depicted in Fig. 2. First, we apply Tikhonov-regularized linear tomography, which uses an analytical prior (smoothness) to assist the reconstruction of absorption coefficient (K_j) fields, from which we extract temperature and mole fraction via two-line thermometry [32]. We subsequently evaluate a novel physics-trained deep learning-assisted tomography method, which uses reacting flow simulations as training-based priors to assist in the prediction of temperature and mole fraction fields directly. While linear tomography is a more established laser absorption technique for spatially resolved measurements in non-uniform

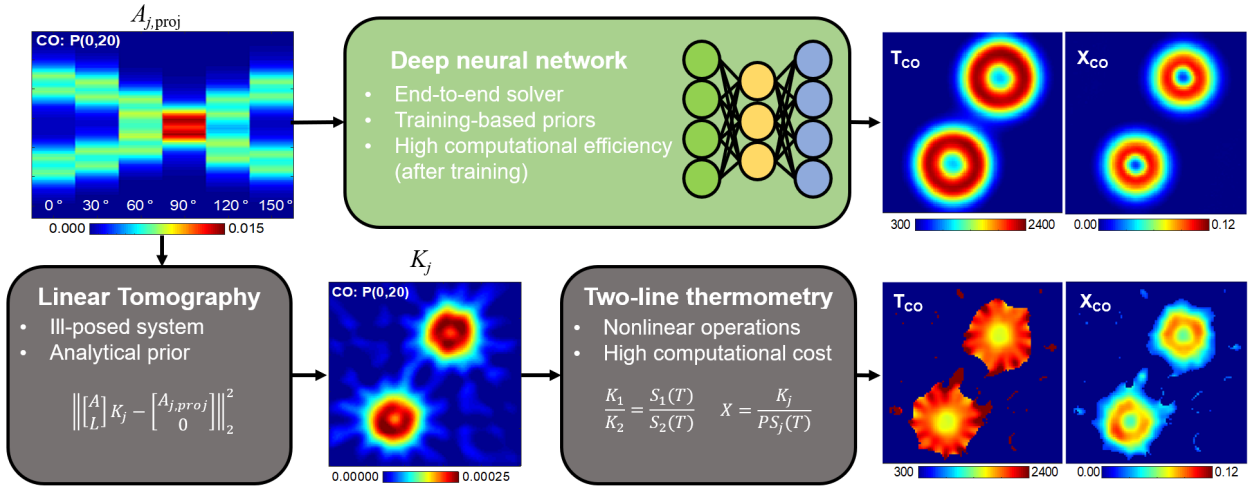

Figure 2 – Flowchart for deep learning (DL) and linear tomography (LT) approaches.

reacting flows [1], the deep learning approach (and associated training process) is hypothesized to enable convenient integration of prior knowledge related to combustion physics, the experimental setup, and spectroscopic properties, which are captured in the forward projection process. We detail both approaches in this section, with specific application to the volumetric LAI setup described in Fig 30.

As a basis for reference, the forward projection process is modeled as a linear parallel-beam tomography problem and the flow field is discretized into a 100×100 rectangular grid probed by 128 parallel lines of sight from N projection angles (nominally $N = 6$). Writing Eq. 1 for all $N \times 128$ lines of sight yields a system of linear equations:

$$\mathbf{AK_j} = \mathbf{A_{j,proj}} \tag{2}$$

where $\mathbf{A_{j,proj}}$ and $\mathbf{K_j}$ represent the projection sinogram and 2D field of the absorption coefficients, respectively, both in vector form. $\mathbf{A}$ is the projection matrix, where A_{ij} represents the absorption length for the ith beam passing through the jth pixel. Due to limited-angle measurements, matrix $\mathbf{A}$ is rank-deficient (and ill-posed), which is addressed here with Tikhonov regularization [5]. This linear tomography approach is well-established [6, 7, 8, 10, 11], and was previously used to perform initial volumetric laser absorption imaging [9].

In the learning-based approach, a deep neural network performs the inversion by predicting 2D temperature and species fields from the projected absorption measurements provided as inputs. In this work, we train the neural network by modeling the physics associated with the forward process to create an implicit function between input and output pairs. The forward model includes reacting fluid dynamics simulations (detailed in Section 1.2.3.) to generate temperature and concentration field data, shown in the top of Fig. 3. Spectral simulations using line-by-line parameters from the HITEMP database [33] are performed in each grid cell to simulate K_j fields, after which a forward projection using a Radon transform is applied to calculate path-integrated line-of-sight projections $A_{j,\mathrm{proj}}$ that reflect the VLAI setup depicted as sinograms in the top right of Fig. 3. The physics-governed data are used as a labeled dataset to train the neural network.

The neural network architecture is adapted from an implementation previously demonstrated to efficiently reconstruct species distributions directly from limited-angle spectroscopy data [26]. The number of convolutional layers and filter sizes are determined following this work, based on the convergence and the prediction accuracy of the test data set. The network comprises two convolutional layers, two pooling layers and one fully connected layer. As illustrated in the bottom of Fig. 3, the

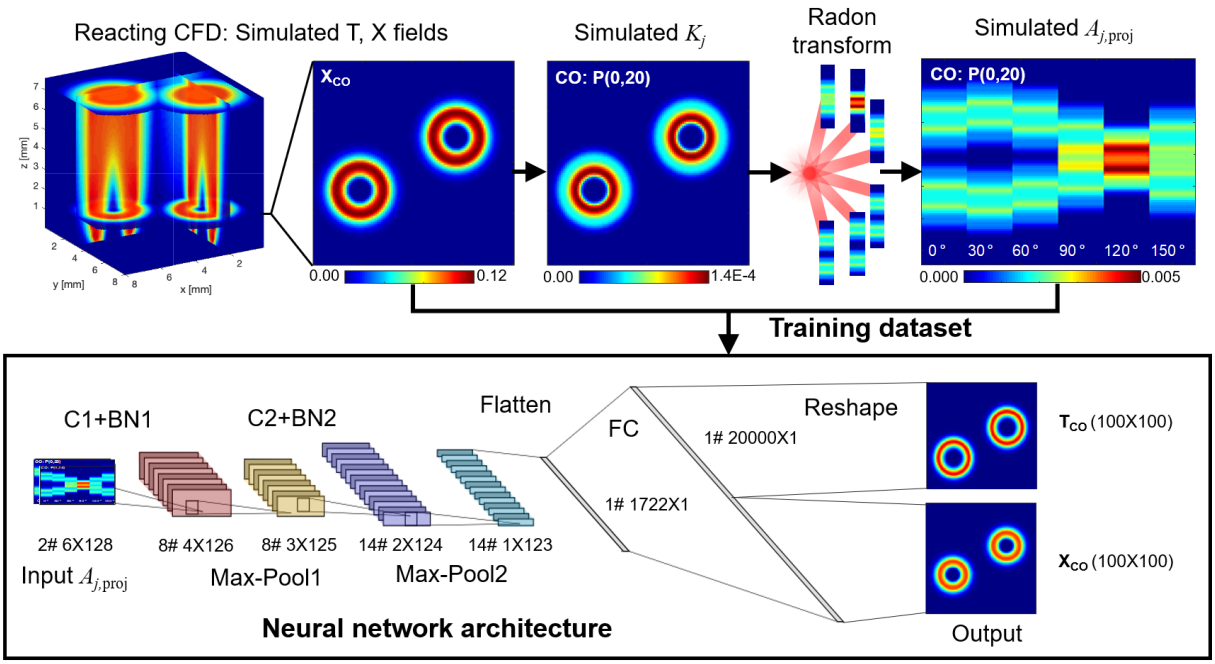

Figure 3 – Convolutional neural network architecture for temperature and mole fraction field predictions provided six different angles of projection data.

input to the neural network comprises 2 sinograms ($N \times 128$), one from each CO spectral transition. The first convolutional layer C1 convolves 8 filters of 3×3 with stride 1 followed by a rectifier nonlinearity, a batch normalization layer BN1, and a max pooling layer with filters of 2×2. The second convolutional layer C2 similarly convolves 14 filters of 2×2 with stride 1 followed by a rectifier nonlinearity, a batch normalization layer BN2, and a max pooling layer with filters of 2×2. After a flatten layer and a fully connected layer FC, an output vector of size 20000×1 is obtained, which can easily be reshaped as two 100×100 2D profiles of temperature and CO mole fraction, respectively. The loss function minimized during training was a simple mean squared loss between the network output and target normalized temperature and CO mole fraction values. The RMSprop algorithm is used with minibatches of size 16, learning rate 0.001, momentum 0.0, and decay 0.9. The network was trained for 100 epochs (typically 20–30 mins) on the Tensorflow deep learning framework using an 8 GB NVIDIA RTX 2080 graphics card. After the training process finishes, an effective inversion operator with implicit physical priors on combustion thermochemistry, transport, and flame symmetry is learned, and can be applied to new path-integrated measurements to reconstruct the temperature and concentration fields. This effectively bypasses the inversion of $A_{j,\mathrm{proj}}$ to K_j obtained through linear tomography [9], as well as two-line thermometry [32], and directly results in thermochemical profiles of the flow-field. Although DNN requires a 20–30 min training process as mentioned, once the networks are established the subsequent reconstructions are computationally efficient. When implemented on an Intel(R) Core(TM) i7-9700K 3.60 GHz CPU, DNN completed reconstructions of all pixel rows in ~1 s while linear tomography took ~30 s, largely due to the nonlinear operations required for two-line thermometry.

1.2.3. Neural network training

To provide a priori information for the DNN based on combustion physics, thermochemical fields are generated using NIST's *Fire Dynamics Simulator* (FDS), a large-eddy simulation (LES) code for thermally-driven, low-speed reacting flows [34]. The training dataset comprises 14,700 2D flow-field cross-sections of temperature and CO mole fraction, generated from 139 time-averaged (~1 s) LES predictions of a partially-premixed Bunsen-style flame in an axisymmetric 2D domain, as shown in

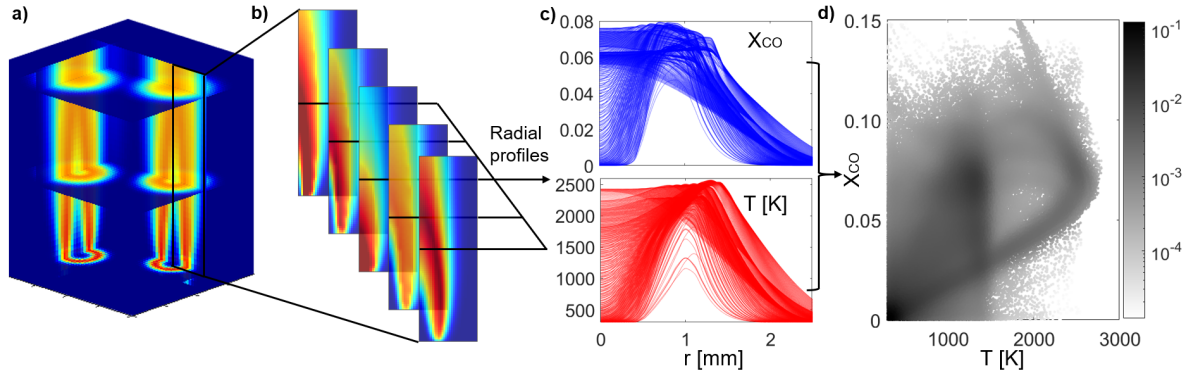

Figure 4 – Reacting CFD-based training dataset; (a) 3D flow-field in experimental geometry; (b) 2D fields for various flow conditions; (c) selected 1D profiles of CO mole fraction and temperature; (d) probability distribution of simulated thermochemical state space.

the top of Fig. 3. To obtain top-down cross sections from the axisymmetric flowfields, the 2D results are azimuthally projected to generate 3D flow-fields representative of the doublet flame experimental geometry, as shown in Fig. 4(a). In these simulations, the input parameters of fuel/oxidizer ratio, reactant gas temperature and flow rate, burner geometry, ambient oxygen concentration, and co-flow rate are systematically varied so as to produce a wide range of possible thermochemical fields, shown in Fig. 4(c). For data encompassing flame interactions, the training set is supplemented by a smaller number of 2D flow-field cross-sections (2,040) from 51 simulations of two partially-premixed Bunsen-style flames in a 3D domain. The inclusion of 3D doublet simulations was shown to improve reconstructions at higher planes where there is greater interaction between the two flames. A simplified diffusion-limited two-step combustion model is employed in the simulations, wherein all fuel is converted to CO prior to final oxidation to CO_2. For each of the 2D simulations, the domain comprises a 30×100 Cartesian mesh corresponding to 15 mm × 50 mm and encompassing burner diameters of 5.0–7.5 mm, while the domain for each of the 3D simulations comprises a 50×50×40 mesh corresponding to 40 mm × 40 mm × 32 mm and encompassing burner diameters of 8 mm each. These dimensions are larger than the corresponding experiments and were chosen to reduce computational effort in generating multiple distinct flowfields. The time-steps of the simulations were automatically varied to satisfy the Courant-Friedrichs-Lewy condition [34] (CFL $\leq$ 1). To avoid over-constraining flowfield priors and account for real parameter distributions that differ from the mid-fidelity LES model, we supplement the training dataset with mixed temperature and mole fraction distributions randomly selected from the results. This step is intended to build flexibility into the neural network (reduce stiffness) while learning the implicit functional relationship of temperature and species with absorbance fields. By mixing temperature and mole fraction distributions, prediction accuracy on a test set of 1000 samples (not included in the training set) is improved by a factor of 2 as measured by mean percentage error across all samples. Additionally, the two flames are allowed to be distinct to account for any potential differences in the flow rates encountered in the measurements. A representative 2D histogram of the thermochemical state-space captured in the training dataset is shown in Fig. 4(d).

Despite the numerical simplifications and adjustments, the mid-fidelity model provides key physical information that helps guide (via training) flow-field parameter solutions to the ill-posed inversion problem. First, the training data reflects a physical range of temperatures and mole fraction values governed by thermochemistry—e.g., the temperature range is bound by the mixture's adiabatic flame temperature, and CO mole fraction is limited by the amount of carbon in the reactant inlet stream. Second, the training data provide a general correlation among temperature and mole fraction; although the distribution of thermochemical states shown in Fig. 4 has significant spread (which is somewhat deliberate), field solutions in which temperature is high and CO mole fraction is low (and

vice versa) are improbable, thereby further informing more likely solutions. Lastly, the mid-fidelity model provides a relative spatial distribution of mole fraction and temperature by creating distinct regions of temperature increase associated with the oxidation of the fuel to CO, the oxidation of the CO to CO_2, and diffusive mixing with ambient temperature air. The flame geometry, including convoluted circular ring-like distributions of the mean CO and temperature properties, is also captured. The training process enables the neural network to recognize these physical features.

1.3. Results

In this section, we evaluate reconstructions produced by the deep learning approach in comparison to those calculated using linear tomography with respect to three key metrics: (1) overall flow-field parameter reconstruction accuracy given sparse view angles, (2) artifact reduction and sharp gradient resolution, and (3) geometric and thermochemical similarity to physical flames. These quantitative evaluations are performed via both simulated and experimental LAI-obtained non-axisymmetric flow fields using varying numbers of projection angles.

1.3.1. Reconstruction accuracy

To assess and compare the reconstruction accuracy of the inversion methods, both approaches (deep learning and 2D linear tomography) were applied to reconstruct "known" CO and temperature fields—independent of the training dataset—representative of measured flames. These known thermochemical fields were produced by first applying a Tikhonov-regularized Abel inversion [6] to projection measurements of isolated single flames assuming steady, axially-symmetric conditions, as demonstrated in prior work on LAI-obtained projection data [28]. Different pairs of these reference profiles of varying intensity were then combined to represent a non-axisymmetric doublet flame configuration, and serve as "ground truth" for the simulation study. These reference profiles were compared with reconstructions produced by both 2D linear tomography and the deep neural network. A mean percentage error within the domain of interest was used as a comparative metric, and representative results alongside simulated "ground truth" fields are shown in Fig. 5. As is typically

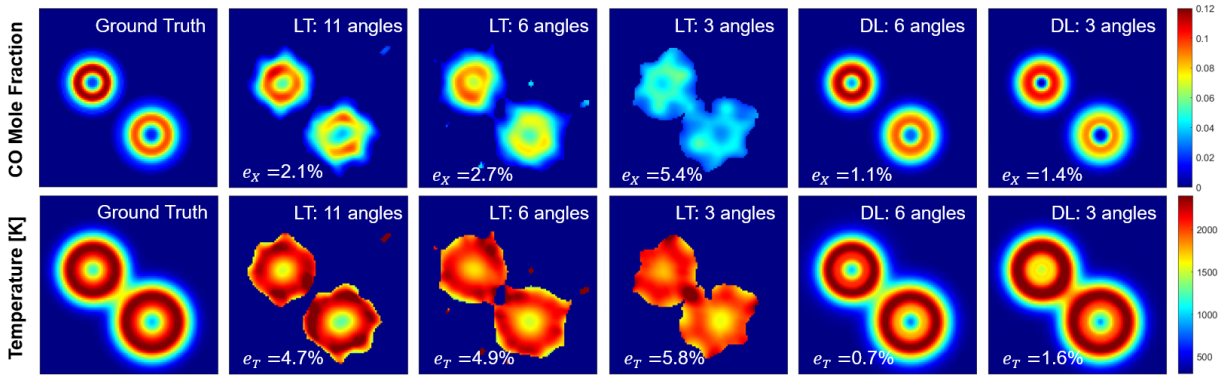

Figure 5 – Comparison of linear tomography (LT) and deep learning (DL) reconstruction methods for mole fractions (top) and temperatures (bottom) with representative case.

observed in ill-posed inversion problems [5], utilizing a greater number of projection angles was shown to increase the overall accuracy of the reconstructed fields. For example, in the CO mole fraction fields shown in Fig. 5, the mean percentage error reduced from 5.4% to 2.7% when using six instead of three angles in the linear tomography reconstruction; the corresponding error reduction for the neural network reconstruction was from 1.4% to 1.1%. For the corresponding temperature fields, the increased number of angles reduced the error from 5.8% to 4.9% using linear tomography; this error reduction using the neural network reconstruction was from 1.6% to 0.7%. Notably, even when trained with only three projection angles, the neural network was able to predict the high spatial

gradients in the flow-field with greater accuracy than 2D linear tomographic methods using 11 angles, significantly reducing the required number of projections for a reconstruction. For a given number of projection angles, the deep learning approach, on average, reduces mean percentage errors relative to linear tomography by a factor of at least three.

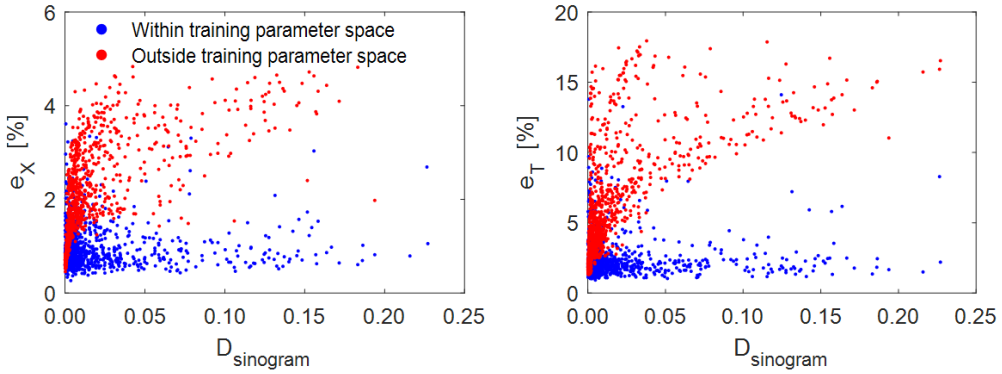

Figure 6 – Reconstruction accuracy of testing cases in mole fraction (left) and temperature (right) as a function of the L_2 distance to their nearest training case.

To further evaluate the interpolation and extrapolation capability of the trained DNN, additional LES simulations inside (500 cases) and outside (500 cases) the envelope of LES input parameter spaces are used as testing cases. These parameter spaces include ranges of mixture ratio, inlet temperature, burner inlet velocity, burner diameter, co-flow velocity, ambient oxygen concentration, and fuel type (ethane or ethylene). The reconstruction accuracy of the testing cases in temperature and mole fraction is evaluated as a function of their distance to the nearest training sinogram as shown in Fig. 6. The distance is quantified by the L_2 distance between the sinogram of the testing case and its nearest training sample:

$$\mathrm{D}_{\mathrm{sinogram}} = \left\| \mathbf{A}_{\mathbf{proj,testing}} - \mathbf{A}_{\mathbf{proj,training}} \right\|_2 \tag{3}$$

Within training parameter space, most testing cases are found to remain high reconstruction accuracy ($e_X < 2\%, e_T < 5\%$) even when they are different from the training cases (large $\mathrm{D}_{\mathrm{sinogram}}$), indicating good interpolation capability of the DNN. However, for cases outside training parameter space, the prediction errors are usually 3 times higher than cases within training parameter space. Additionally, the DNN predictions are less stable with out-of-sample inputs, with prediction errors increasing with distance to the training set. Such limitations on the extrapolative capability must be considered when developing and applying comprehensive physics-trained DNNs to measurements of experimental reacting flows.

With the deep learning approach validated via simulation, the neural network inversion was applied to experimental LAI-obtained projection measurements of various flame doublets such as those shown in the left of Fig. 30. Reconstructed 2D fields of temperature and mole fraction are shown in the left of Fig. 7 for both the 2D linear tomographic and deep learning-based inversion methods. Since a "ground truth" for the thermochemical fields determined from experimental measurements of the non-axisymmetric flowfield is unknown, the quality of the reconstructions was evaluated by re-projecting the predicted temperature and CO fields using the forward model described in Section 1.2.2. and comparing the result with the measured projected absorption areas, as shown in the right of Fig. 7. An aggregate root mean square error (RSME) was used as a comparative metric, calculated as the square root of the averaged squared differences between the re-projected absorbance image and the corresponding measurement image all over pixels. Despite the lack of an analytical relation, the re-projected absorbance fields using the deep learning method were shown to have comparable RSME, within 10%, to linear tomography results (which are analytically constrained) using experimental

VLAI data from the same number of projection angles, demonstrating the neural network's ability to well-capture the non-linear relationships associated with the end-to-end physics of the experiment.

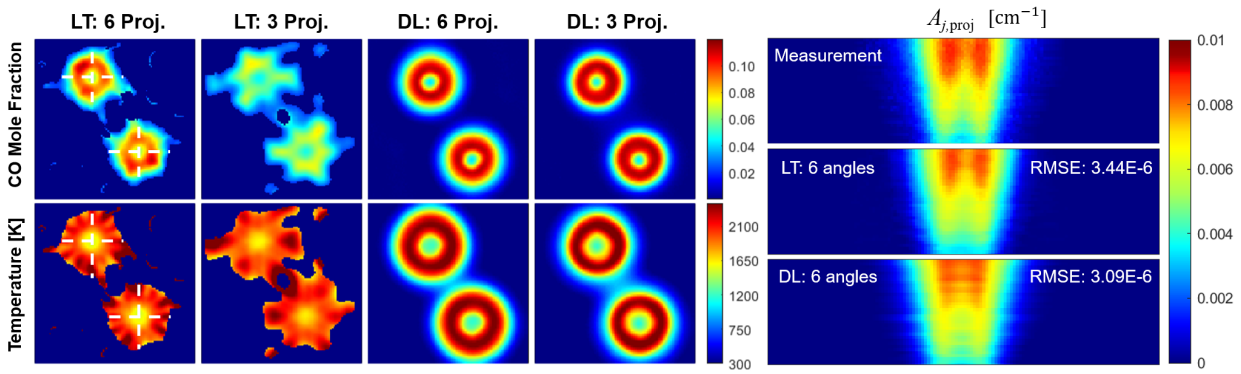

Figure 7 – *Left:* Two-dimensional tomographic reconstructions of CO mole fraction (top) and temperature (bottom) generated from linear tomography and deep learning methods; *Right:* Reprojection of reconstructed fields at an angle of 120°.

1.3.2. Blurring and artifact reduction

In linear tomographic reconstruction, the ill-posed nature of the inversion problem in conjunction with the smoothness constraint imposed by Tikohonov regularization will often result in blurring of reconstructed flow-field parameters as well as the presence of polygonal petal-like artifacts associated with the limited view angles [5]. These phenomena are seen in both the simulation results shown in Fig. 5 and the experimental results shown in Fig. 7 produced by linear tomography. Specifically, at 3 view angles, the peak values in the species field distributions are approximately 50% lower than the 11-angle LT solution, while the minimum values associated with the core of the flow are higher by approximately 30%. This reflects an apparent blurring and lower spatial resolution, and has the effect of increasing the size of the reconstructed flame brush—in Fig. 5, using three instead of six angles increases the flame brush width (here marked by 1% CO concentration) from 1.6 mm to 2.0 mm when using linear tomography, while this increase is imperceptible in the reconstructions produced by the neural network. Further, it can be noted that the polygonal petals of the field distributions for linear tomography are an apparent function of the number of view angles, where the number of polygonal corners or petals in circular or ring-like distributions equate to twice the number of view angles. Additionally, we note that in reconstructed regions in which the absorption coefficients K_j of both spectral transitions approach zero, the temperature sensitivity of the spectral transition pair can generate physically improbable temperature and mole fraction values via two-line thermometry (using the LT method) if the signal-to-noise ratio (SNR) in the projected absorbance area $A_{j,\mathrm{proj}}$ data is below ~ 5. By contrast, since the neural network need not satisfy Eq. 2 explicitly as is the case with linear tomography; this method mitigates artifacts in the periphery of the flames (which would not have shown up in the training data), reduces artificial polygonal bias in the reconstructed field, and ultimately yields sharper features in the regions of higher intensity, as seen in the left of Fig. 7.

Additionally, due to physical features and trends associated with the neural network training data, it is feasible to predict a larger domain of the species and temperature fields. Notably, the domain representing final oxidation of CO to CO_2 and diffusion into the ambient is difficult to resolve with linear tomography due to lower absorbance caused by both lower CO and declining temperature in the regions where ambient oxidizing air is entrained into the flow. Thus, in Figs. 5 and 7, neither the temperature nor the mole fraction are resolved in regions with very low values of absorption coefficient ($K_{\mathrm{P}(1,14)} < 0.0005$) for the 2D linear tomography reconstructions, and so these regions are not plotted for clarity (due to extensive non-physical results and artifacts). With six projection angles,

this limits the resolved peripheries of the flames to $r/D \approx 0.94$ from the flame centers ($D = 1.6$ mm), where the temperature is 2400 K. By contrast, the physics-trained neural network was able to predict thermochemical profiles beyond the domain constrained by the analytical solutions, as the method bypasses two-line thermometry of the K_j fields. Assuming a temperature cutoff of 850 K (the lowest temperature predicted in the flame cores by the deep learning method), this extends the resolved regions to $r/D \approx 1.25$ from the flame centers, representing a domain expansion of 33% compared to LT.

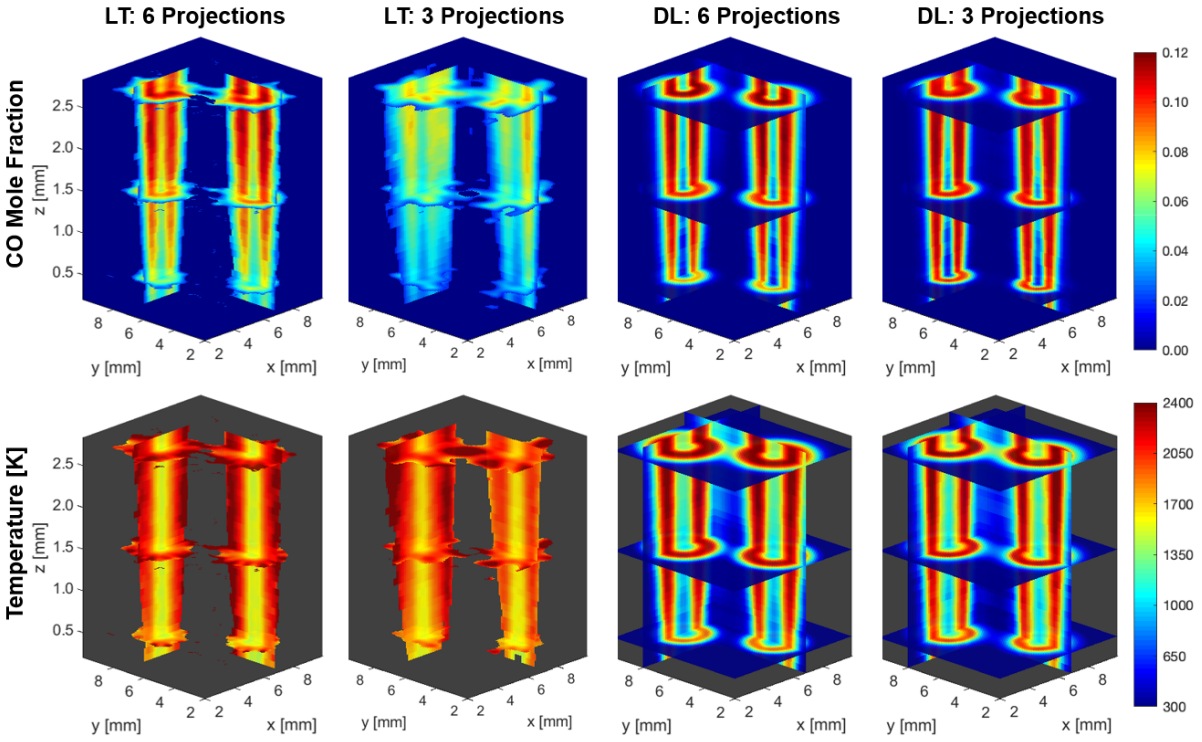

Figure 8 – Three-dimensional tomographic reconstructions of CO mole fraction (top) and temperature (bottom) generated from linear tomography and deep learning methods

These 2D fields corresponding to different rows of pixels are assembled into 3D images of mole fraction and temperature for the C_2H_4 flames, shown in Fig. 8 for both the 2D linear tomographic and deep learning-based inversion methods. Both linear tomography and the neural network results show that the cooler cores narrow as flame height increases and more of the unburned fuel is oxidized in the reaction layers of the flames, which is consistent with the general evolution of partially-premixed Bunsen-style flames [35]. Higher spatial gradients are resolved within the flames when using the deep learning-based method, revealing the flame cores of the flows containing lower temperatures and concentrations of CO, and sharper rings with higher temperatures and concentrations of CO. For example, when using six projection angles, the lowest temperature resolved by linear tomography in the core of the flames at the lowest measured flame height is 1500 K, while the neural network reconstruction produced 850 K. The corresponding CO mole fraction values were 0.034 for linear tomography and 0.012 for the deep learning-based method. This is most evident in the lower planes of the flames, where CO concentration and temperature are both lower, providing for weaker absorption and higher susceptibility to measurement noise.

1.3.3. Thermo-physical state space

In this subsection, we discuss the thermo-physical state space associated with the tomography results, including the range and correlations associated with species and temperature fields that relate

to thermochemistry and transport, as well as geometric features of the flame configuration. Flames possess steep spatial gradients associated with balancing diffusive heat and mass transfer, and intermediate species like CO usually exist in a very thin reaction zone (<1 mm) within a corresponding large temperature rise (>2000 K) during oxidation from reactants to products [35]. Correlations of temperature and concentration are often used to quantify overall flame thermochemistry and evolution [36], and blurring associated with limited angle tomography can bias these correlations by muting the steep gradients in flow-field parameter distributions in the reconstruction. Thus, the ability to quantitatively assess the combustion physics in these flames is directly coupled to the inversion method's ability to resolve sharp features in the flow-field parameters. Additionally, the Bunsen-style flames possess inherent symmetries associated with coupled mass, momentum, and heat transport phenomena. Except for planes with significant interactions between the two flames, the temperature and mole fraction distributions are expected to be approximately axially symmetric in each flame; that the distributions are not preferentially grouped on one side of the flame or the other. In reconstructions using linear tomography, however, such as in Figs. 5 and 7, axial asymmetries are present and worse when employing fewer projection angles, manifesting as the petal-like artifacts and azimuthal variation discussed in Section 3.2.

To quantitatively assess the individual flame symmetry, a Tikhonov-regularized Abel inversion [28] was applied to a projection measurement of an isolated single flame to reconstruct the radial temperature and mole fraction profiles assuming steady, axisymmetric conditions. It should be noted that this reference comparison is only valid at low flame heights, where the two flames minimally interacted. The left of Fig. 9 compares averaged 1D radial profiles of temperature and CO mole fraction for flames in the flow, obtained from both linear tomography and deep learning with respect to the reference Abel-inverted profiles. These profiles were generated by averaging different

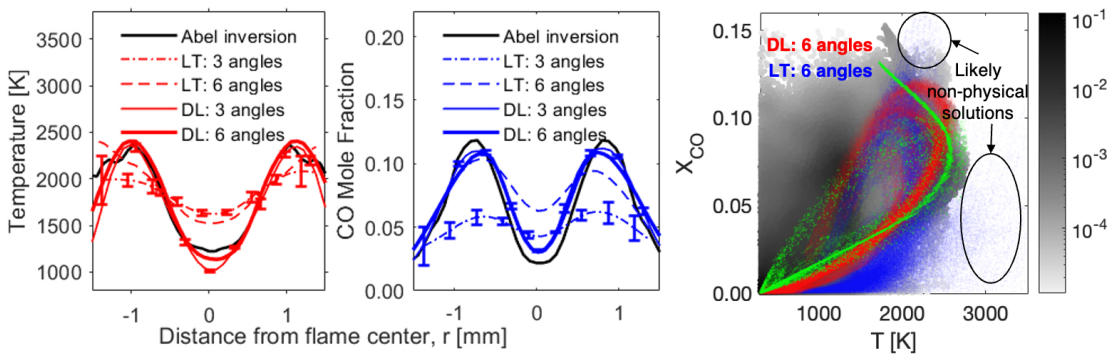

Figure 9 – *Left:* One-dimensional reconstructions of temperature and CO mole fraction from linear tomography and deep learning; *Right:* Thermochemical state-spaces of the deep-learning-based and linear tomography solutions alongside training data. Training samples with closest sinograms shown in green.

1D profiles marked by the white dashed lines in Fig. 7, and the error bars in Fig. 9 quantify the absolute deviations from this average in the azimuthal coordinate. When using three view angles, the mean deviations in temperature and mole fraction produced by linear tomography are 6% and 17%, respectively, while the corresponding deviations produced by the neural network are 2% and 4%, demonstrating that reconstructions performed with the neural network better capture the axial symmetry of the flames. With linear tomography, reducing the number of projection angles from six to three causes large absolute errors in temperature and mole fraction compared to the reference Abel results, while the deep learning approach was found to be less sensitive to the number of projections used. Even with only three projection angles, the neural network predicts temperature and CO profiles closer to the reference Abel profiles than linear tomography with six angles, thereby effectively reducing the required number of unique projections for a parameter field reconstruction.

Notably, peak mole fractions are reduced more significantly than peak temperatures (−50% vs. −16% when using three projection angles, respectively) in the linear tomography reconstructions, which has the effect of producing physically improbable temperature and mole fraction flow-fields for the flames.

An analysis of the thermochemical state-space representation of the linear tomography and deep learning results is conducted by examining correlations between CO and temperature based on six projection angles, as shown in the right of Fig. 9. Scatter data from all measurement planes using both methods are plotted alongside the training data, and the training case with closest sinogram to the measurements is highlighted (green). Notably, linear tomography is found to produce many solutions that are likely non-physical—the thermochemical state space produced by linear tomography contains points with temperatures greater than 2000 K and CO mole fractions lower than 0.05, which are unlikely to simultaneously occur in physical flames in the captured domain. Conversely, the thermochemical state-spaces of the reconstructions predicted by the deep learning-based method largely stay within the reacting CFD-generated state space; however, the neural network predictions do not strictly follow the most probable regions of the 2D histogram produced by the CFD or their nearest samples in the training set. Notably, the temperature / CO state-spaces of the deep learning-predicted reconstructions are generally consistent with those measured in analogous laboratory flames by coherent anti-Stokes Raman spectroscopy and two-photon laser induced fluorescence [37], though peak CO concentrations are much higher in the present study (∼12% vs. ∼5%) due to the fuel-rich mixtures used. Given the sparse number of view angles, these results highlight the ability of the neural network to assist in capturing complex relationships associated with combustion physics when trained with mid-fidelity reacting CFD simulations. Moreover, these simulations do not appear to overly bias the DNN results given that even the closest simulation cases do not match the resulting predictions, suggesting that the variation in the training data provides for flexibility in the implicit functional relationships of the network.

1.4. Conclusions

A deep neural network trained with mid-fidelity reacting flow simulations and a forward absorbance model was applied to enhance the measurements of CO and temperature fields in steady flames using a relatively limited number of viewing angles. Notably, the DNN training was performed a priori—without inclusion of measurement results—while effectively introducing end-to-end physical priors that inform the implicit functional relationships. When paired with the spatially-rich projection data provided by the volumetric laser absorption imaging optical configuration, the neural network helps resolve steep thermochemical gradients associated with the intermediate CO in the thin reaction zones (<1 mm) of small diameter flames. Resulting 3D images of thermochemical structure suggest that this physics-trained neural network inversion has potential to more accurately predict complex temperature and concentration fields of intermediate species in flames with less blurring and artifacts than linear tomographic methods, while concurrently reducing the required number of projections and computational load. The use of a deep learning-based approach and associated reduction in optical hardware requirements expands the possible future developments of the LAI method; 3D flame measurements presented here represent 1-s averaged data from steady flames—to expand the 3D tomographic LAI method to time-resolved capability, as has been demonstrated previously in two dimensions [30], multiple projection angles must be imaged simultaneously. The use of deep learning assistance may reduce the number of high-speed IR cameras required and increases the practicality of utilizing time-resolved 3D tomographic LAI for investigations of unsteady, convoluted flame structures.

2. Methane Line Mixing Model

2.1. Introduction

Methane (CH_4) is an important molecule in biology, planetary astronomy, climatology, agriculture, and combustion chemistry. As a principal fuel component of natural gas, intermediate in the oxidation of larger hydrocarbons, and—increasingly—a promising future rocket fuel [38, 39], CH_4 plays a key role in energy conversion systems globally, and high-temperature spectroscopy of CH_4 is particularly relevant to combustion research [40]. Additionally, temperature-dependent spectroscopy of CH_4 is relevant for both remote and in-situ sensing of terrestrial [41, 42, 43], extraterrestrial [44, 45], and extrasolar [46, 47] planetary atmospheres. CH_4 is one of the most substantial contributors to Earth's greenhouse effect, after CO_2 and H_2O [48], and its accurate detection and spectroscopic modeling is key to understanding its environmental impact on Earth [49]. This work documents an experimental investigation of $^{12}CH_4$ spectra from 3.14 μm to 3.28 μm at elevated pressures relevant to energy conversion systems over a wide range of elevated temperatures (up to 1600 K), with the goal of developing a predictive model of the target spectral domain that accurately captures the pressure- and temperature-dependence of collisional line mixing effects.

Several researchers have utilized absorption by methane for quantitative in-situ measurement of species concentration and/or temperature at elevated temperatures [50, 51, 52, 53, 40, 54, 55, 56, 24, 57]. Many of these studies [53, 40, 54, 55, 56] employ empirical peak-to-valley absorption methods or cross-section correlations for quantitative interpretation of specific wavelengths, an approach that avoids the complexity of the underlying line-by-line spectroscopy of CH_4 but lacks in scalability over varying thermodynamic conditions or bath gases. Line-by-line modeling offers greater utility, but the spectroscopic complexities must be addressed.

Though the simplest stable hydrocarbon, CH_4 poses numerous spectroscopic modeling challenges, particularly at elevated temperatures and pressures. The tetrahedral molecule exhibits a complicated series of interacting vibrational states (polyads) as a consequence of the approximately similar energies of two fundamental bands and two overtone bands ($\nu_1 \approx \nu_3 \approx 2\nu_2 \approx 2\nu_4$) [58]. As a result, the spectra of a given polyad of CH_4 often comprise overlapping fundamental bands, hot bands, overtone bands, and combination bands, complicating measurements of spectroscopic parameters such as linestrength, collisional broadening and shift coefficients due to local spectral blending. Moreover, the abundance of spectral transitions in these bands poses computational challenges for comprehensive and accurate predictive modeling of CH_4 spectra at elevated temperatures; only recently has a high-temperature line list for CH_4 that balances both accuracy and computational efficiency been compiled and made available via HITEMP [59]. Notably, however, even with a comprehensive line list significant disagreement in spectral absorbance, relative to that predicted by conventional lineshape summation of individual transitions, can be observed for measured CH_4 spectra at moderately elevated gas densities. This is largely attributed to line mixing, a band or manifold narrowing effect in spectrally dense regions that occurs at high gas densities resulting from collision-induced changes in the populations of energy states [60]. We focus this experimental study on the characterization of line mixing behavior from 300–1600 K in the R-branch of the ν_3 band of CH_4 over a wide range of pressures and gas densities with the simple goal of developing an accurate empirical model.

Line-mixing in the ν_3 band of CH_4 at temperatures at or below 300 K at a variety of pressures has been investigated previously [61, 62, 63, 64, 65, 66, 67, 68, 69, 70, 71, 72, 73, 74, 75, 76], owing to its relevance in sensing of the atmospheres of Earth [70], the Jovian planets [71], and Titan, a natural satellite of Saturn. Line mixing is notably pronounced in the Q branch, as well as in the higher rotational energy manifolds (J-manifolds) of the P and R branches due to the

multiplicity of ro-vibrational transitions in close proximity. Various line mixing models have been developed and employed to describe CH_4 spectra for ranges of temperatures and pressures relevant to in-situ and remote atmospheric sensing. First-order line mixing models based on the perturbative treatment proposed by Rosenkranz [77] have been shown to adequately characterize line mixing at low pressures [78, 61, 62, 63, 66, 67, 69, 73, 74, 75, 76]. At higher pressures, energy-gap scaling models which correlate the population transfer rates that comprise the relaxation matrix have been used [64, 65, 66, 68, 69, 70, 71]. Though successfully implemented for some linear molecules [79, 80, 81], energy-gap laws [82, 83] have been found less appropriate for modeling non-linear molecules such as CH_4 at low to moderate densities [64].

To the authors' knowledge, the temperature dependence of line mixing effects on CH_4 ν_3 spectra has not been previously investigated above 300 K. Some temperature-dependence studies of line mixing for CH_4 have been performed in the ν_3 region between 200 K and 300 K [65]. Line mixing parameters and temperature dependence in the P(9) manifold of the ν_3 band were measured between 90 and 296 K by Mondelain et al [72]. The line mixing parameters in the $R(6)$ manifold of the ν_3 band were also recorded over the temperature range from 213.5 K to room temperature [73]. In general, the collective of previous CH_4 line mixing studies have been focused on examining behavior near ambient temperature (~300 K) or below.

This paper describes experimental measurements and modeling of the aforementioned line mixing effects in the triply degenerate antisymmetric C-H stretch ν_3 band of CH_4 at temperatures up to 1600 K, relevant to combustion environments. R-branch spectra from $R(0)$ to $R(18)$ are initially examined at various pressures (2–25 atm) and temperatures (298–1021 K) using Fourier transform infrared spectroscopy (FTIR) combined with a heated gas cell. Line mixing and its temperature dependence in the $R(15)$ manifold are further examined using interband cascade laser absorption spectroscopy near 3.15 μm at low pressures (0.3–2 atm) and elevated temperatures (298–1610 K) in both a gas cell and shock tube. A modified exponential gap law and first-order line mixing approximation (perturbation theory) were both used to model the line mixing effects of CH_4 perturbed by N_2 and compared at different experimental conditions. The adequacy of the two empirical models for capturing the CH_4 line mixing effects under varying assumptions is also discussed, including non-ideal behavior observed over varying pressure and temperature.

2.2. Theory

2.2.1. Line mixing

Spectral absorbance, α_ν, accounting for line mixing collisions can be written within the impact approximation in the following form:

$$\alpha_\nu = -\ln\left(\frac{I_t}{I_0}\right)_\nu = \frac{NL}{\pi}\,\mathrm{Im}(\mathbf{d}\cdot\mathbf{G}^{-1}\cdot\boldsymbol{\rho}\cdot\mathbf{d}) \tag{4}$$

where N [molec·cm^{-3}] is the total number density of the absorbing species and L [cm] is the path length, ρ is a diagonal matrix with nonzero elements ρ_i defined by the lower state Boltzmann population fraction:

$$\rho_i = \frac{N_i}{N} = \frac{g_i''}{Q}\exp\left[\frac{-hcE''}{k_BT}\right] \tag{5}$$

Here, N_i [molec·cm^{-3}] is the number density at a certain energy level, g_i'' is the lower state degeneracy, E'' [cm^{-1}] is the lower state energy, Q is the total internal partition function, h [J·s] is Planck's constant, and c [cm/s] is the speed of light, and $\mathbf{d}$ [cm^{-1}/(molec·cm^{-2})]$^{1/2}$ is a vector of transition

amplitudes with elements d_i given as:

$$d_i = \sqrt{\frac{S_i(T)}{\rho_J}} \tag{6}$$

The dependence on wavenumber, ν [cm^{-1}], is within $\mathbf{G}$ [cm^{-1}], a complex matrix defined as:

$$\mathbf{G} = \nu\mathbf{I} - \mathbf{H} \tag{7}$$

Where $\mathbf{I}$ is the identity matrix and a frequency-independent matrix $\mathbf{H}$ [cm^{-1}] is defined as:

$$\mathbf{H} = \boldsymbol{\nu}_0 - i\mathbf{W} \tag{8}$$

ν_0 [cm^{-1}] is a diagonal matrix of transition frequencies and $\mathbf{W}$ [cm^{-1}] is the relaxation matrix which captures collisional effects on the spectra and is given by:

$$\mathbf{W}_{ij} = \begin{cases} \Delta\nu_{c,i} - i\Delta_i & \text{if } i = j \\ PA_{RR}R_{i\to j} & \text{if } i \neq j \end{cases} \tag{9}$$

Where P is the total pressure in units of [atm], the real diagonal elements of $\mathbf{W}$ are the collisional half-widths $\Delta\nu_{c,i}$ [cm^{-1}], and the imaginary diagonal elements are the pressure shifts Δ_i [cm^{-1}]. The real off-diagonal elements are linearly proportional to the state-specific population transfer rates, $R_{i\to j}$ [cm^{-1}/atm], between two states i and j. The off-diagonal components of $\mathbf{W}$ represent contributions from rotational dephasing, which are neglected here and set to zero. In Eq. (5), $\mathbf{H}$ can be diagonalized using a similarity transform to obtain a diagonal eigenvalue matrix Ω [cm^{-1}] with diagonal elements ω_i [cm^{-1}] such that:

$$\boldsymbol{\Omega} = \mathbf{A}^{-1} \cdot \mathbf{H} \cdot \mathbf{A} \tag{10}$$

Since $\mathbf{G}$ only differs from $\mathbf{H}$ by a constant diagonal matrix, $\mathbf{G}^{-1}$ is also diagonalized by $\mathbf{A}$. Eq.(1) can now be written as a function of ν spanning all relevant spectral transitions i:

$$\alpha_\nu = \frac{NL}{\pi} \operatorname{Im}\left[\sum_i \frac{(\mathbf{d}\cdot\mathbf{A})_i(\mathbf{A}^{-1}\cdot\boldsymbol{\rho}\cdot\mathbf{d})_i}{(\nu - \omega_i)}\right] \tag{11}$$

If we define, $\Lambda_i = (\mathbf{d}\cdot\mathbf{A})_i(\mathbf{A}^{-1}\cdot\boldsymbol{\rho}\cdot\mathbf{d})_i$, α_ν becomes a sum over Lorentzian and dispersion terms:

$$\alpha_\nu = \frac{NL}{\pi}\sum_i \frac{\operatorname{Im}\boldsymbol{\Omega}_i \cdot \operatorname{Re}\boldsymbol{\Lambda}_i + \operatorname{Im}\boldsymbol{\Lambda}_i(\nu - \operatorname{Re}\boldsymbol{\Omega}_i)}{(\nu - \operatorname{Re}\boldsymbol{\Omega}_i)^2 + \operatorname{Im}\boldsymbol{\Omega}_i^2} \tag{12}$$

2.2.2. Perturbative treatment theory

The perturbative treatment (PT) theory for modeling line mixing consists of making a perturbative expansion of the eigenvalues and eigenvectors of the matrix $\mathbf{H}$ in powers of $W_{ij}/(\nu_i - \nu_j)$. They can be introduced in Eq. 12, which gives the first order treatment:

$$\alpha_\nu = \frac{NL}{\pi}\sum_i \frac{S_i[\Delta\nu_c + Y_i(\nu - \nu_0)]}{(\nu - \nu_{0,i} - \Delta_i)^2 + \Delta\nu_c^2} \tag{13}$$

with

$$Y_i = 2\sum_{j\neq i}\frac{d_j}{d_i}\frac{W_{ij}}{\nu_i - \nu_j} \tag{14}$$

where S_i, $\Delta\nu_c$, Δ_i and Y_i are the linestrength, collisional width, pressure shift and line mixing coefficient for the spectral line i. The expression in Eq. 13 will have different forms depending on the lineshape model assumed. When accounting first-order line-mixing, the spectral absorbance assuming the Voigt profile (a convolution of the Doppler and Lorentzian profiles) becomes:

$$\begin{aligned}\alpha_\nu =& \frac{NL}{\pi}\sum_i \left(\frac{S_i}{\Delta\nu_{D,i}}\right)\left(\frac{\ln(2)}{\pi}\right)^{1/2} \\ & (\mathrm{Re}[c(\nu,x_i,y_i)] + Y_i\cdot \mathrm{Im}[c(\nu,x_i,y_i)])\end{aligned} \tag{15}$$

where $\Delta\nu_{D,i}$ is the Doppler half-width (HWHM), c is the complex error function, and

$$\begin{aligned}x_i &= \frac{\nu-\nu_{0,i}-\Delta_i}{\Delta\nu_{D,i}}(\ln(2))^{1/2} \\ y_i &= \frac{\Delta\nu_{c,i}}{\Delta\nu_{D,i}}(\ln(2))^{1/2}\end{aligned} \tag{16}$$

At low pressures, it may be necessary to consider the influence of narrowing mechanisms, such as Dicke narrowing and speed-dependent effects [84, 85]. When considering first-order line-mixing for the Rautian profile, the corresponding absorbance is given by:

$$\begin{aligned}\alpha_\nu =& \frac{NL}{\pi}\sum_i \left(\frac{S_i}{\Delta\nu_{D,i}}\right)\left(\frac{\ln(2)}{\pi}\right)^{1/2} \\ & \times\left(\mathrm{Re}\left[\frac{c(\nu,x_i,y_i)}{1-\sqrt{\pi}\beta c(\nu,x_i,y_i)}\right]\right. \\ & \left.+Y_i\cdot\mathrm{Im}\left[\frac{c(\nu,x_i,y_i)}{1-\sqrt{\pi}\beta c(\nu,x_i,y_i)}\right]\right)\end{aligned} \tag{17}$$

When considering speed dependent effects, the collisional width becomes a function of molecular speed and is modeled with the following expression:

$$\Delta\nu_{c,i}(\upsilon) = \Delta\nu_{c,i}(\upsilon_m)\left(1+a_{s,i}\left[\left(\frac{\upsilon^2}{\upsilon_p}\right)-\frac{3}{2}\right]\right) \tag{18}$$

Where υ is the speed of the absorbing molecule, υ_m is the mean speed of the absorber, υ_p is the most probable speed of the absorbing molecule, and $a_{s,i}$ is the speed-dependent coefficient for line i. The absorption coefficient for the speed-dependent Voigt profile with line mixing becomes:

$$\begin{aligned}\alpha_\nu =& \frac{NL}{\pi^{3/2}}\sum_i S_i\int_{-\infty}^{+\infty} e^{-\upsilon^2}\upsilon \\ & \times\left(\tan^{-1}\left[\frac{\upsilon+x_i}{y_i(a_{s,i}(\upsilon^2-1.5)+1)}\right]^2\right. \\ & \left.+\frac{Y_i}{2}\ln\left[\frac{\upsilon+x_i}{y_i(a_{s,i}(\upsilon^2-1.5)+1)}\right]^2\right)d\upsilon\end{aligned} \tag{19}$$

It should be noted that the line mixing among transitions with different A, E, F symmetry are negligible for CH_4 because of the symmetry of the intermolecular potential [62, 76] and the line mixing parameter sum rule constraint $\sum_i S_iY_i$=0 [63] was used for each A, E or F symmetry block. The temperature

dependence of the parameter Y_i is given by the following empirical relation:

$$Y(T) = Y(T_0)\left(\frac{T_0}{T}\right)^n \tag{20}$$

Lastly, we note that in cases where the local linewidths substantially exceed the line spacing, a first-order treatment may not be adequate to fully capture line mixing effects [77, 86]. However, in this data-driven work, we constrain the perturbative treatment to a first-order empirical model framework for simplicity.

2.2.3. Modified exponential gap law

In the modified exponential gap (MEG) law, the real part of the off-diagonals of the relaxation matrix W_{ij} in Eq. (6) can be constructed using the following form:

$$\begin{aligned} W_{ij} = PA_{RR}R_{i\to j} = P \times a_1(T) &\left[\frac{1 + a_4\left(\frac{E_i''}{a_2 k_B T}\right)}{1 + a_4\left(\frac{E_i''}{k_B T}\right)}\right]^2 \\ &\times \exp\left[\frac{-a_3\left(E_j'' - E_i''\right)}{k_B T}\right] \end{aligned} \tag{21}$$

where $a_1(T)$ [cm^{-1}/atm], a_2, and a_3 are species-specific MEG law coefficients retrieved from spectral fits of the measured absorbance. a_4 describes the collision duration based on distance of closest approach and is kept constant for all the R manifolds in the spectral fitting performed in this study. A_{RR} is a scaling constant associated with mixing in the R-branch. Since collisions promote the Boltzmann population distribution, the upward and downward population transfer rates, $R_{i\to j}$ and $R_{j\to i}$, can be related through the detailed-balance principle [87]:

$$\rho_j R_{j\to i} = \rho_i R_{i\to j} \tag{22}$$

A single set of measured absorbance is sufficient to obtain the species-specific MEG law coefficients for a given temperature [88], and $a_1(T)$ can be modeled as a power law expression to determine the temperature dependence of the relaxation matrix components:

$$a_1(T) = a_1(T_0)\left(\frac{T_0}{T}\right)^m \tag{23}$$

where $a_1(T_0)$ is the MEG law coefficient at a reference temperature, T_0, and m is defined as the temperature exponent, obtained by fitting multiple sets of absorbance data over a range of temperatures.

In the present work, the broadening half width (HWHM) and the pressure shift for CH_4-N_2 are calculated using CH_4-air broadening and shift coefficients from the HITEMP database [59]. Only the line mixing coefficients are set as free parameters for both the MEG law and perturbative treatment models in fitting the measured spectra.

2.3. Experimental setup

An FTIR and tunable interband cascade laser near 3.16 μm were used to measure the CH_4 absorption spectra in a heated gas cell over a range of temperatures from 300–1000 K. A high-enthalpy shock

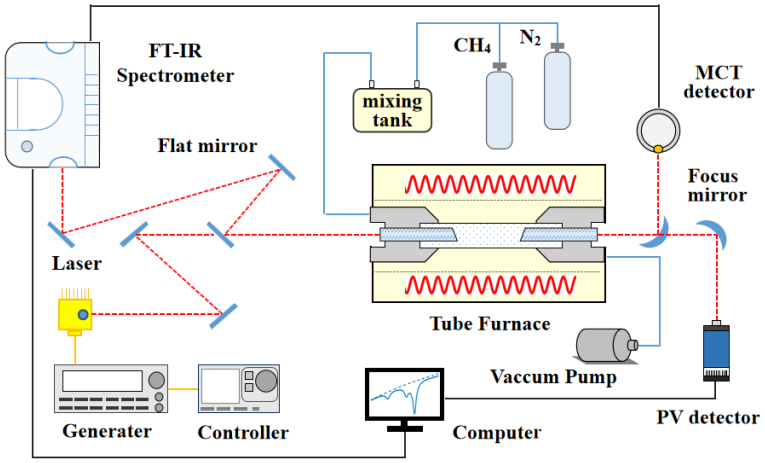

Figure 10 – Experimental setup for the laser and FTIR in the gas cell.

tube was additionally used for measurements at higher temperatures from 1000–1700 K with the laser source. Here we detail the experimental configurations.

2.3.1. FTIR gas cell measurements

To determine the line mixing parameters of the CH_4 ν_3 R branch, absorbance measurements were made using a high-temperature high-pressure optical gas cell at temperatures varying from 300–1000 K and pressures varying from 0.3–25 atm. The cell body is housed in a tube furnace and connected to a local gas delivery manifold leading to vacuum pumps, source gas bottles, and an agitated mixing tank used to barometrically prepare CH_4/N_2 mixtures for experimental measurements, as shown in Fig. 10. The gas pressure within the cell is monitored with a variable capacitance pressure transducer for high-pressure measurements and a dual-capacitance manometer for measurements below 1000 torr with accuracies of 0.25% and 0.12%, respectively. The cell temperature is monitored with multiple K-type thermocouples along the test region with an accuracy of 0.75%. More details about the mechanical design of the cell, including a thermal analysis of temperature uniformity, are described in previous work [89].

Over the full range of pressures, two different optical systems were used to measure the CH_4 absorbance spectra. At test pressures from 0.3–2.0 atm, a narrow linewidth laser was used to spectrally-resolve the $R(15)$ manifold, discussed further in Sec. 2.3.2.. For pressures ranging from 2.0–25 atm, a Fourier-transform infrared spectrometer (Nicolet iS50 FTIR) was used to capture the entirety of the ν_3 band. We focus our study and data analysis to the R branch in part due to poor transmission (and lower data quality) at the longer P-branch wavelengths which is attributed to the temperature-dependent transmission of the sapphire windows on the heated gas cell. The FTIR measurements shown here represent a spectral resolution of 0.125 cm^{-1} using the Happ-Genzel apodization function with Mertz phase correction and no applied zero-filling. Measured spectra were compared to experimental data by Pieroni et al. [64] to check that FTIR settings were appropriate for the conditions of interest, yielding accurate results with weak dependence on apodization function. For each temperature and pressure condition, the gas cell was initially vacuumed for the background measurements before introducing the test mixtures. Test measurements were taken with N_2 as the test gas to ensure no pressure dependence of the FTIR background signal and validate the use of vacuum for background measurements. The cell pressure and temperature was monitored to ensure thermal equilibrium of the test gas within the gas cell prior to data collection. The measured data represent 16 averaged scans with a total data collection time of 5 minutes with pressure constant and slight fluctuations in temperature recorded for use in the uncertainty analysis.

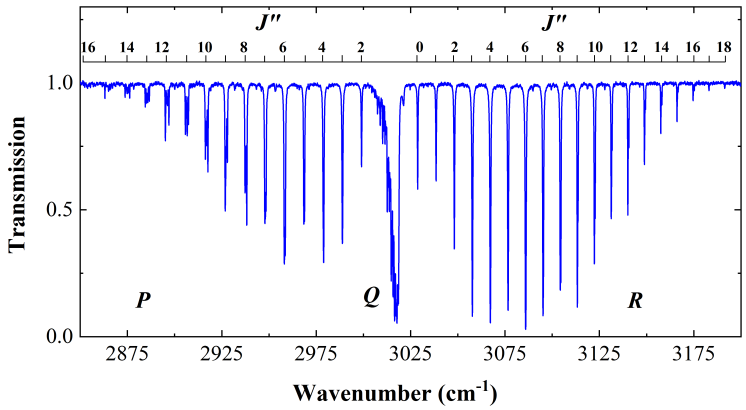

Figure 11 – The measured transmission of the CH_4 ν_3 band: $P = 2$ atm, $T = 298$ K, $X_{CH_4} = 0.0052$. The strong lines ($J'' = 0$–18) belong to the ν_3 band consisting of P, Q and R branches. Weak lines belong to the $2\nu_3$, $2\nu_4$ and $\nu_2 + \nu_4$ bands.

Fig. 11 shows an FTIR measurement of the CH_4 ν_3 band at the pressure of 2 atm and temperature of 298 K with 0.52% CH_4 diluted in N_2, which encompasses P, Q and R branches up to $J'' = 18$. Notably, each J'' consists of a manifold of transitions with varying symmetry and n quantum index [90], which increases with J''. The line mixing of the R branch from $R(0)$ to $R(18)$ manifold was measured using the FTIR at various pressures from 2 atm to 25 atm and the $R(15)$ manifold was more extensively measured at lower pressures from 0.3 atm to 2.0 atm using the laser source.

2.3.2. Laser absorption spectroscopy optical setup

For high spectral-resolution investigations of CH_4 near 3.16 μm in both the high-temperature optical cell and the high-enthalpy shock tube, a continuous-wave distributed feedback (DFB) interband cascade laser (ICL) (Nanosystems and Technologies GmbH) is used to access the individual rovibrational transitions comprising the $R(15)$ manifold. This specific wavelength is targeted for high-temperature combustion sensing applications. The ICL is tunable from 3162 to 3171 cm^{-1}, and has a nominal output power of 15 mW at 3166 cm^{-1}. A 10 kHz sawtooth waveform of injection current is used to tune the ICL across a 2 cm^{-1} wavenumber range to resolve the entire $R(15)$ manifold. Additionally, the injection current is scanned below the lasing threshold to account for thermal emission from the gases in both experimental devices.

The optical arrangement of the high-resolution sensor on both the high-temperature optical cell and the high-enhtalpy shock tube is shown in Figs. 10 and 12, respectively. The transmitted laser radiation is passed though an optical iris and a bandpass spectral filter (Spectrogon, 3160±60 nm) to minimize thermal emission before being focused onto a thermo-electrically cooled photovoltaic (PV) detector (VIGO System PVI-4TE-5). For each measurement I_t, a corresponding background I_0 is recorded in the absence of a mixture to establish a baseline for calculation in Eq. 4. The relative frequency of the laser light is determined by placing a germanium etalon with a free spectral range of 0.0241 cm^{-1} in the path of the beam using an optical flip-mount.

2.3.3. Shock tube measurements

A high-enthalpy shock tube is used to generate higher temperatures (>1050 K) via near-instantaneous shock heating of test gases. The shock tube is described in previous work by the authors [91, 80, 81], and shown in Fig. 12. Analogous to the gas cell experiment, the driven and driver sections of the shock tube are connected to vacuum pumps, an agitated mixing tank, and a gas delivery manifold used to barometrically prepare the mixtures for the experimental measurements. The test section of

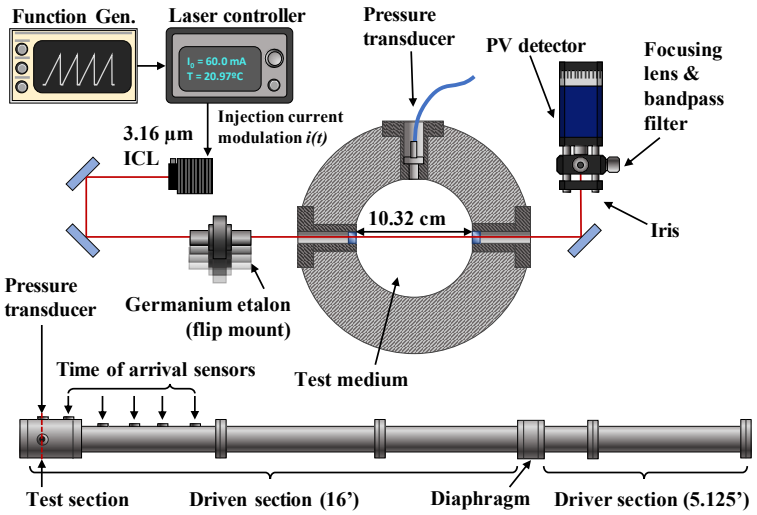

Figure 12 – Experimental setup for the laser alignment on the shock tube.

the device has an internal diameter of 10.32 cm, defining the path length L in Eq. 4. Interchangeable ports holding a dynamic pressure transducer (Kistler 601B1) and optical windows circumscribe the test section 2 cm from the shock tube end wall. The pressure transducer records the pressure time history of the incident and reflected shock wave through a charge amplifier (Kistler Type 5018A), and five piezoelectric sensors (Dynasen CA-1135) record the time of arrival of the incident shock wave, from which the incident shock velocity and reflected shock test conditions are determined [92]. When accounting for non-ideal gas dynamics, the uncertainties in reflected shock temperature T_5 and pressure P_5 are typically about 1% [93]. Once the ICL, germanium etalon, and photovoltaic detector were aligned, a series of tests were performed. Example raw voltage data from the detector and transducer charge amplifier, shown in the top of Fig. 13, were recorded at 10 MHz using a PicoScope 4000 series data acquisition module, triggered to record by the time-of-arrival sensors. Spectrally-resolved CH_4 absorption measurements at 10 kHz were conducted in the shock tube for the temperature range 1050–1610 K and the pressure range 0.4–1.3 atm using scanned-wavelength techniques. For these high-temperature shock tube studies, a mixture of 5% CH_4 in an N_2 bath gas was used as the test gas.

2.4. Results and discussion

Empirically-determined line mixing coefficients of CH_4 perturbed by N_2 are reported for the ν_3 R branch between 3024–3200 cm^{-1} over a range of conditions. Models based on the modified exponential gap (MEG) law and perturbation theory were used to fit the experimental absorbance spectra and determine temperature and pressure dependence of the line-mixing parameters. For all spectral modeling and fitting, values for the transition line centers $\nu_{0,i}$, linestrengths $S_i(T_0)$, lower state energy levels E_i'' and collisional broadening coefficient $\gamma_{air,i}$ were taken from the HITEMP database for CH_4 [59]. Natural abundance of $^{12}CH_4$ is assumed for all experiments. The following two subsections describe experimental results for the entire ν_3 R-branch at high pressures (2–25 atm) and the $R(15)$ manifold at lower pressures (0.2–2 atm), respectively.

2.4.1. Line mixing in the ν_3 R-branch at high pressures

Measured absorbance of the R branch and the best-fit MEG model at a pressure of 24.5 atm at room temperature are shown in Fig. 14(a), with stem plots (blue) showing the positions and linestrengths of the transitions comprising each J-manifold. Each manifold from $R(0)$ to $R(18)$ was fit separately using MEG model with no line mixing considered between different manifolds. Within each manifold,

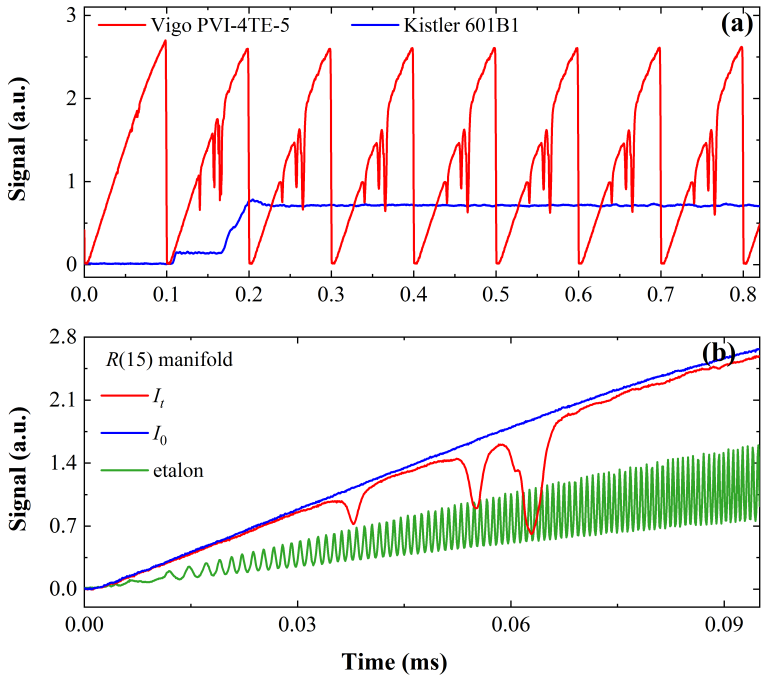

Figure 13 – (a) Raw detector and pressure transducer signals during non-reactive shock heating of CH_4 in a N_2 bath gas. (b) Example scanned-wavelength detector signal in the shock tube for incident light I_0, transmitted light I_t, and incident light through the etalon.

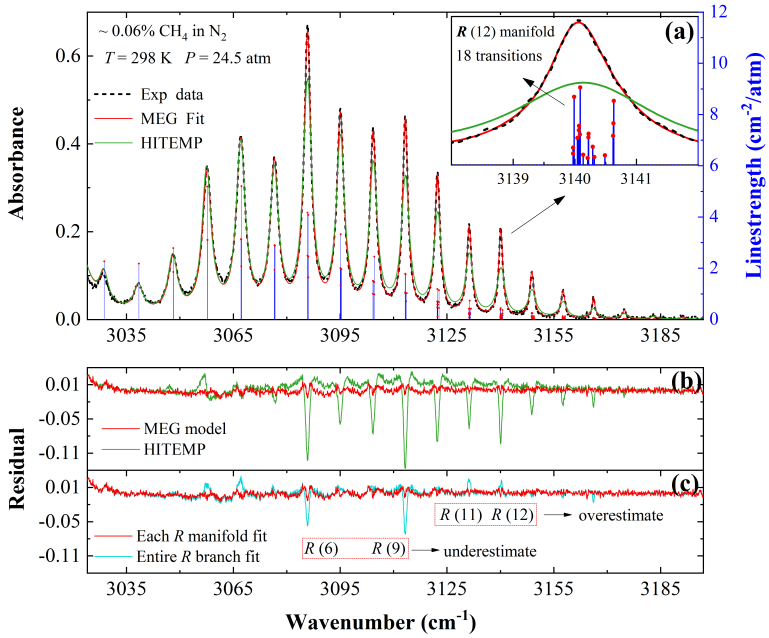

Figure 14 – (a) Measured absorbance for $R(0)$ to $R(18)$ at 24.5 atm and 298 K with corresponding MEG model fits (red) alongside prediction using HITEMP without considering line mixing (green). Note: The air-broadening coefficients and their temperature exponents in HITEMP were used in place of N_2-broadening. (b) Residuals from the fits considering line mixing (red) and predictions not considering line mixing (green). (c) Residuals from the fits considering line mixing within each manifold individually (red) and considering intra-branch mixing in the entire R branch (blue).

only lines within three orders of magnitude of the strongest line were evaluated for mixing. The line strength of the weakest line included in the line mixing model for each manifold is denoted $S(T_0)_{min}$ in Table 1. The inset in the top-right corner of Fig. 14(a) shows the $R(12)$ manifold absorbance in

greater detail, considering 18 transitions. Absorbance from weak lines below the specified linestrength cutoffs was calculated using the HITEMP database parameters assuming Voigt profiles at the gas cell condition; this absorption was fixed in the fitting procedure used to obtain the line mixing parameters of the stronger transitions. For all simulations, the entire spectral range of interest (2850–3200 cm^{-1}) is simulated for each line considered so as to account for absorption by the far wings of each transition.

Comparative residuals from the MEG model fits (red) and from HITEMP predictions not considering line mixing (green) in Fig. 14(b) highlight different levels of line mixing for various R manifolds. The level of disagreement observed by not accounting line mixing (as a percentage of peak manifold absorbance) tends to increase with J'', though not monotonically, associated with the increasing multiplicity of lines within each manifold. The entire R branch was also fit integrally using the MEG model with only one group of line mixing coefficients a_1 through a_4, with the residuals presented in Fig. 14(c). Considering line mixing amongst all measured spectra captures the line mixing behavior of some J-manifolds very well, such as $R(7)$, $R(8)$ and $R(10)$; however, the line mixing is underestimated for $R(6)$ and $R(9)$ and overestimated for $R(4)$, $R(11)$ and $R(12)$. For the subsequent results reported in this study, each J-manifold was fit independently when using the MEG model.

The R branch was also measured at elevated temperatures, from 541 K to 1021 K at pressures up to 25 atm. Representative absorbance measurements at 10 atm and multiple temperatures are shown in Fig. 15 with the MEG law fits and corresponding residuals. It can be observed that the MEG law model does not fully capture line mixing, with peak residuals (~4–8%) at T = 541 K shown in Fig. 15(b), but the model is significantly improved over a HITEMP simulation without line mixing (green). At these elevated temperatures, several hot band transitions are observed, most prominently at 809 K and 1021 K. The measured absorbance in these spectral domains between the fundamental band manifolds is reasonably consistent with expected values calculated using the updated HITEMP database, without accounting for line mixing, and sufficient for properly modeling the far wings of the primary manifolds of interest. We note that transitions of the naturally abundant (~1%) $^{13}C^{1}H_4$ are also included in the absorbance simulations, although no line mixing is accounted here due to the relative weakness of these lines being below the aforementioned linestrength threshold. Similarly, the fit provided by the MEG model at the highest pressure of 25 atm (and for these elevated temperatures) generally captures the line mixing behavior, although there remains small underestimation of peak absorbance in each manifold with peak residuals of ~0.8–5.6% at T = 541 K and ~4.9–10.6% at T = 1021 K.

The species-specific MEG law coefficients a_2, a_3, and a_4 for each J-manifold are obtained by fitting the absorbance at a single condition where the model works very well (room temperature and 25 atm) [64], and are held constant when fitting the spectra at different temperatures to obtain $a_1(T)$. The temperature dependence of $a_1(T)$ for each manifold was determined by applying a weighted least-squares fit [94] of the power-law expression in Eq. 29 to these $a_1(T)$ values at different temperatures (also at 25 atm). Representative experimentally obtained values of $a_1(T)$ for the $R(14)$, $R(15)$ and $R(17)$ manifolds are presented alongside corresponding power-law fits in Fig. 16. The calculated species-specific MEG law coefficients and temperature exponents for all the manifolds are given in Table 1, along with the number of lines considered in the fits and the minimum transition linestrength among those lines, $S(T_0)_{\min}$. Overall weaker absorbance in the ν_3 band at elevated temperatures contributes to increased measurement uncertainty in the coefficients as seen in Fig. 16, largely due to lower measurement signal-to-noise ratio (SNR). Although inter-manifold blending is present in the spectral regions surrounding the higher J'' manifolds, the restriction to intra-manifold line mixing (similar E'' at the same J'') in our fitting procedure enables improved spectral simulation compared to a single MEG model for the entire branch. As such, the listed coefficients for each manifold in

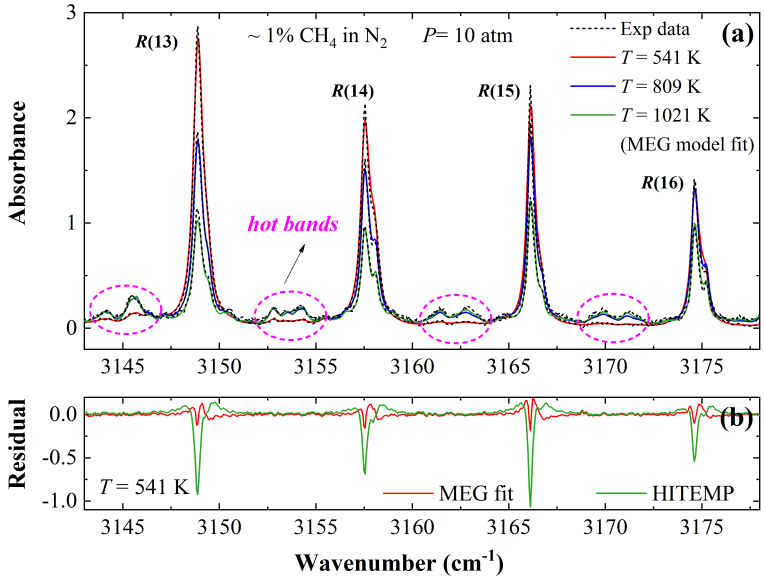

Figure 15 – (a) Measured absorbance from $R(13)$ to $R(18)$ for elevated temperatures (541 K, 809 K and 1021 K) at 10 atm with corresponding spectral fits from the MEG law model. Note: The air-broadening coefficients and their temperature exponents in HITEMP were used in place of N_2-broadening. (b) Residuals from the fits considering line mixing (red) and predictions without considering line mixing (green) at 541 K.

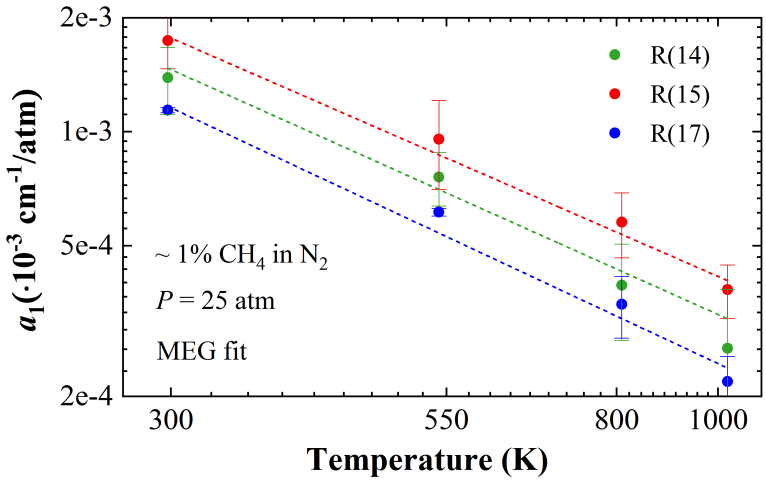

Figure 16 – Temperature dependence of the line-mixing coefficients a_1 [cm^{-1}/atm] and power law fits for the manifolds $R(14)$, $R(15)$ and $R(17)$ at the pressure of 25 atm. The temperature-dependent parameters for the other manifolds are given in Table. 1

Table. 1 are valid for transitions with the same J''. It should be noted that only manifolds for which line mixing is significant, $R(4)$–$R(18)$, are included in Table 1. $R(0)$ only has one transition, and the line mixing within $R(1)$–$R(3)$ is either restricted by transition symmetries (A, E, or F) or very weak ($a_1(T_0) < 10^{-14}$ cm^{-1}/atm).

To test the validity of the empirical MEG model, the reported coefficients were used to calculate the absorbance at $P = 24.4$ atm and $T = 298$ K for comparison with the measured and calculated results from Pieroni et al [64] as shown in Fig. 17. The spectrally-resolved absorption coefficient (α/P_{CH_4} [cm^{-1}/atm]) for the wavenumber region reported in that study was multiplied by the partial pressure of CH_4 and the pathlength of the present experiments to obtain a comparable spectral absorbance α_ν. The predicted spectrum from the MEG law-based line mixing model in the present work is in very good agreement with the absorbance measured by Pieroni et al [64] and shows consistent accuracy in

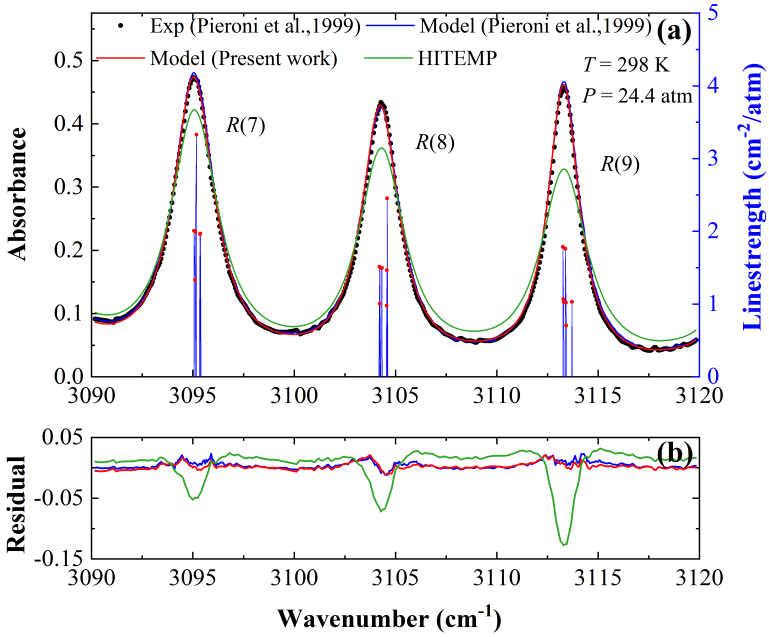

Figure 17 – (a) Absorbance ($X = 0.0006$, $L = 9.4$ cm) calculated from α / P_{CH_4} [cm^{-1}/atm] reported by Pieroni et al [64] at $P = 24.4$ atm and ambient temperature for $R(7)$–$R(9)$. Measured values (black points) shown alongside calculations [64] (blue), the MEG law model of the present work (red), and predictions without line mixing (green). Note: The air-broadening coefficients and their temperature exponents in HITEMP were used in place of N_2-broadening in the present work, while the N_2-broadening was deduced by multiplying the air-broadening in HITRAN by a factor of 1.02 [64, 70]. (b) Residuals from the two line mixing models and calculations without line mixing.

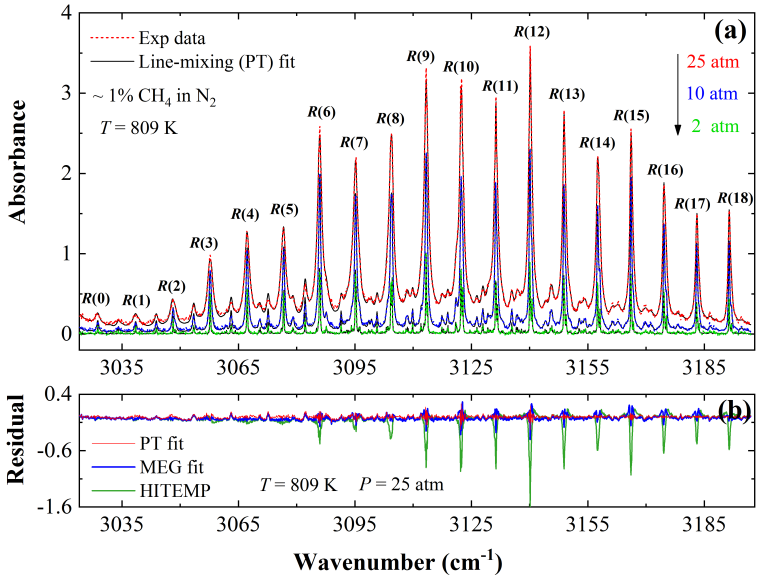

Figure 18 – (a) Measured absorbance from $R(0)$ to $R(18)$ at various pressures (2 atm, 10 atm and 25 atm) at 809 K with corresponding best-fits using first-order line-mixing with the Voigt profile (red). Note: The air-broadening coefficients and their temperature exponents in HITEMP were used in place of N_2-broadening. (b) Residuals from the fits of the first-order line-mixing model (red), MEG law model (blue) and predictions without considering line mixing (green) at 25 atm.

capturing the effects of line mixing among the various manifolds.

Fig. 18(a) shows the broader R-branch spectra ($R(0)$–$R(18)$) measured at 809 K for varying pressure, alongside corresponding spectral fits of the first-order line mixing model (PT) using the

Voigt profile. The residuals for both the PT model (red) and MEG law (blue) are shown in Fig. 18(b). While the MEG model produces larger residuals as pressure or gas density decreases, the first-order line mixing model derived from perturbation theory could fit the measured absorbance well at any pressure and temperature. However, this good agreement associated with the PT model fit should not necessarily be interpreted as a more physical representation of line mixing, but rather the simple result of many more free parameters. In perturbation treatment theory, Eq. 14 is only valid when the transition overlap is not severe [77]; strongly overlapping lines in the measured high-pressure FTIR spectra convolute the retrieved Y_i values obtained from the PT model fits such that they lose direct relation to the off-diagonal elements in the relaxation matrix and allow for multiple solutions. This convolution may be acutely pronounced for the high J'' R-manifolds, wherein more lines exist and line mixing effects are more significant. In floating the Y_i values over the range of high pressures (~5–25 atm) there was no clear pressure dependence (as would be expected) of the line mixing coefficients obtained from the PT model fit, with the exception of the $R(2)$–$R(4)$ manifolds (owing to fewer lines in each manifold). Multiple solutions to the PT fit could also be found given the large number free parameters and fewer distinct spectral features at elevated pressures. As such, a higher-resolution lower-pressure study was deemed necessary for utilization of perturbation theory.

2.4.2. Line mixing of the $R(15)$ manifold transitions

A detailed high spectral-resolution investigation of line mixing among the 13 transitions comprising the $R(15)$ manifold was conducted using interband cascade laser absorption spectroscopy near 3.16 μm at various pressures from 0.3 atm to 2.0 atm in the heated gas cell and shock tube. Fig. 19 highlights the transitions comprising the $R(15)$ manifold along with their ground-state symmetries C'' (A, E, F). The transitions can be grouped into three clusters, referenced by their left-to-right ordering in Fig. 19. Line mixing between the first and second cluster is observed at pressures as low as 0.6 atm, while line mixing between the third cluster and the other two clusters is relatively weak, and we show in this study that it can be neglected at pressures lower than 2 atm. The weak line mixing contribution by the third cluster is likely due to its relative spectral isolation [67], resulting in the constituent transitions with F_1 and F_2 symmetries following the sum rule independent of the other $R(15)$ transitions at each

Table 1 – Temperature-dependent MEG law parameters determined in this work

J''	$S(T_0)_{\min}$ [cm^{-2}/atm]	no. of lines	a_1 [10^{-3} cm^{-1}atm^{-1}]	a_2	a_3	a_4	$m_{CH_4-N_2}$
$R(4)$	$2.09\times10^{+0}$	4	0.99 ± 0.03	1.56 ± 0.06	10.00 ± 0.17	2.69 ± 0.15	1.31 ± 0.08
$R(5)$	$1.95\times10^{+0}$	4	1.32 ± 0.01	0.94 ± 0.02	9.99 ± 0.04	2.69 ± 0.15	1.35 ± 0.02
$R(6)$	$1.65\times10^{+0}$	6	1.97 ± 0.35	0.84 ± 0.24	10.04 ± 2.68	2.69 ± 0.15	1.98 ± 0.18
$R(7)$	$1.34\times10^{+0}$	6	1.24 ± 0.28	0.88 ± 0.09	10.15 ± 0.12	2.69 ± 0.15	1.39 ± 0.25
$R(8)$	9.85×10^{-1}	7	1.22 ± 0.17	0.86 ± 0.01	10.14 ± 0.08	2.69 ± 0.15	1.71 ± 0.15
$R(9)$	7.09×10^{-1}	8	2.06 ± 0.65	0.85 ± 0.01	9.95 ± 1.86	2.69 ± 0.15	1.41 ± 0.34
$R(10)$	1.22×10^{-1}	11	1.13 ± 0.02	0.82 ± 0.12	10.43 ± 0.15	2.69 ± 0.15	1.19 ± 0.02
$R(11)$	7.49×10^{-2}	13	1.07 ± 0.10	0.87 ± 0.10	10.15 ± 0.02	2.69 ± 0.15	1.41 ± 0.10
$R(12)$	3.87×10^{-2}	18	1.08 ± 0.09	0.83 ± 0.11	9.52 ± 0.20	2.69 ± 0.15	1.17 ± 0.09
$R(13)$	3.10×10^{-2}	14	1.29 ± 0.26	0.84 ± 0.09	10.20 ± 0.10	2.69 ± 0.15	1.24 ± 0.22
$R(14)$	3.92×10^{-2}	12	1.39 ± 0.33	0.84 ± 0.07	10.03 ± 0.09	2.69 ± 0.15	1.34 ± 0.26
$R(15)$	2.50×10^{-2}	13	1.74 ± 0.54	0.85 ± 0.03	9.78 ± 0.26	2.69 ± 0.15	1.21 ± 0.34
$R(16)$	1.21×10^{-2}	14	1.21 ± 0.18	0.84 ± 0.06	10.03 ± 0.13	2.69 ± 0.15	1.20 ± 0.16
$R(17)$	5.78×10^{-3}	14	1.14 ± 0.02	0.83 ± 0.10	10.02 ± 0.01	2.69 ± 0.15	1.31 ± 0.02
$R(18)$	2.37×10^{-3}	16	1.19 ± 0.05	0.84 ± 0.05	10.03 ± 0.13	2.69 ± 0.15	1.12 ± 0.04

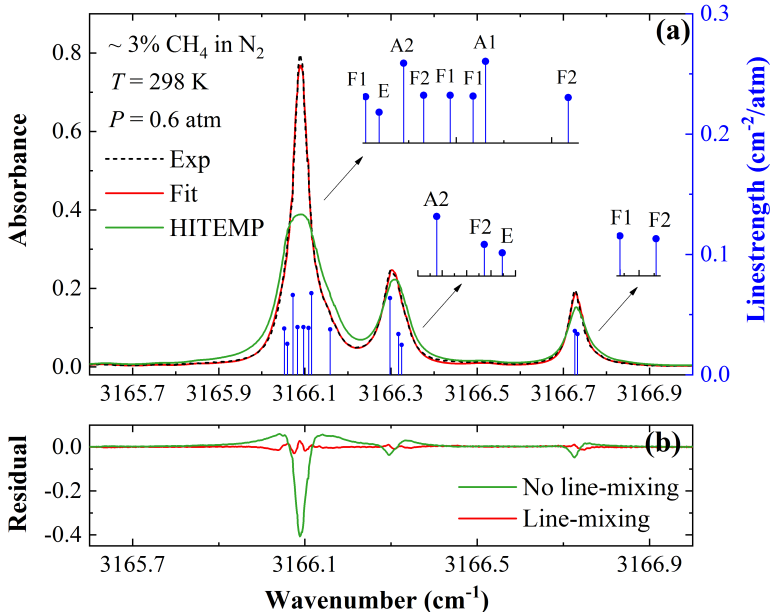

Figure 19 – (a) Measured absorbance of the $R(15)$ manifold at ambient temperature and 0.6 atm with corresponding best-fits from the PT-based line-mixing model using the Voigt lineshape profile (red) alongside prediction using HITEMP without considering line mixing (green). The stem plots indicate the symmetries of each transition. Note: The air-broadening coefficients and their temperature exponents in HITEMP were used in place of N_2-broadening. (b) Residuals from the best-fit of the line-mixing model and predictions without considering line mixing.

pressure.

2.4.3. Line mixing and lineshape model performance

The MEG model and the PT-based model were both used to fit the experimental laser absorption data, and Fig. 20(a) shows the measured absorbance alongside the best-fits from each model, with residuals shown in the lower panel. As expected from the FTIR study, the MEG model does not fully capture line mixing at these low pressures, and the resulting fits yield peak residuals of 5%–30%. The PT-based model, however, better captures line mixing in the R(15) manifold, yielding peak residuals less than 5.5% at any pressure. To examine the performance of the different line mixing models at different temperatures and pressures in more detail, the root mean square error (RMSE) was calculated from the best-fit residuals for both models, as shown in Fig. 21. The RMSE for the MEG model decreases with pressure, while there is no obvious trend for the RMSE obtained from the PT-based model, though the values are smaller for pressures lower than 1 atm. Fig. 21(b) shows that the performance of each model is not strongly dependent on temperature for the temperature range considered in this study, though the first order PT-based model outperforms the MEG model at all temperatures and pressures. The $R(15)$ manifold appears to demonstrate high selectivity in collisional effects for the examined pressure range; significant coupling among the F_1 and F_2 transitions is apparent in the first (strongest) cluster, while much less significant coupling is evident in the third (weakest) cluster. This selectivity renders statistically based fitting laws such as MEG model inappropriate for characterizing line mixing in CH_4 spectra [64], especially at low pressures. For this reason, the remaining discussion focuses on the results obtained from the first order PT-based line mixing model.

To confirm the appropriateness of the Voigt lineshape profile for this study, the first-order PT-based line mixing model using Rautian and speed-dependent profiles were also spectrally fitted against the experimentally measured absorbance at low pressures (≤2 atm). Fig. 22 shows the best fits and fitting residuals for the first-order model with the three profiles at 0.52 atm and 980 K with a

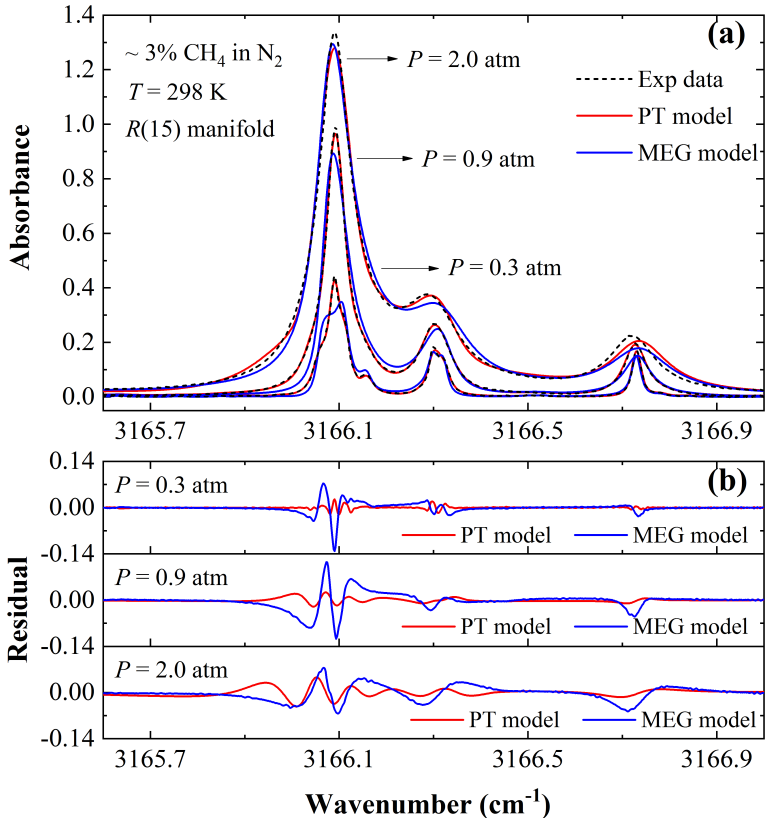

Figure 20 – (a) Measured absorbance of the $R(15)$ manifold for various pressures (0.3 atm, 0.9 atm and 2.0 atm) at ambient temperature (298 K) with corresponding best-fits from the first-order Line-mixing Voigt profile (red) and MEG model (blue). Note: The air-broadening coefficients and their temperature exponents in HITEMP were used in place of N_2-broadening. (b) Residuals from the best-fit of two line-mixing models for each pressure.

Lorentz-to-Doppler broadening ratio of 2.8. The RSME decreases from 1.23×10^{-2} for the original Voigt lineshape profile (VP) to 1.17×10^{-2} for the Rautian profile (RP) and 1.15×10^{-2} for the speed-dependent Voigt profile (SDVP). The inclusion of Dicke narrowing or speed dependence yielded little improvement, and the retrieved corresponding narrowing coefficients approach zero for the two profiles in most cases. For this reason, the Dicke narrowing and speed-dependent coefficients were not measured in this study, and we report only the line mixing coefficients obtained using the Voigt lineshape profile in subsequent plots and in Table 2. We note that collisional widths were calculated using data from HITEMP [59] instead of assigning them as free parameters when using the first-order line mixing profiles [66, 73] owing to unreliable fitting of a highly underdetermined system with significant line mixing effects.

2.4.4. Temperature-dependent line mixing in $R(15)$

The first-order PT-based model using the Voigt profile was spectrally fitted against the measured absorbance of the $R(15)$ manifold at ambient temperature from 0.3–2 atm, as shown in Fig. 23 alongside HITEMP predictions (not considering line mixing) for reference. Overall, we observe that line mixing in the $R(15)$ manifold is significant, even at the lowest pressure condition examined, typically resulting in a factor of two or more increase in the peak linecenter absorbance for the strongest line cluster. Calculations reveal that the collisional width is larger than the frequency spacing at pressures greater than 0.2 atm, associated with population transfers between the same rotational energy states with different levels α (where α is an integer corresponding to different levels of the same rotational quanta) [90]. The $R(15)$ manifold absorption was also measured in the heated gas cell at 541 K, 809 K and 1021 K, and fit with the first-order PT-based model using the Voigt

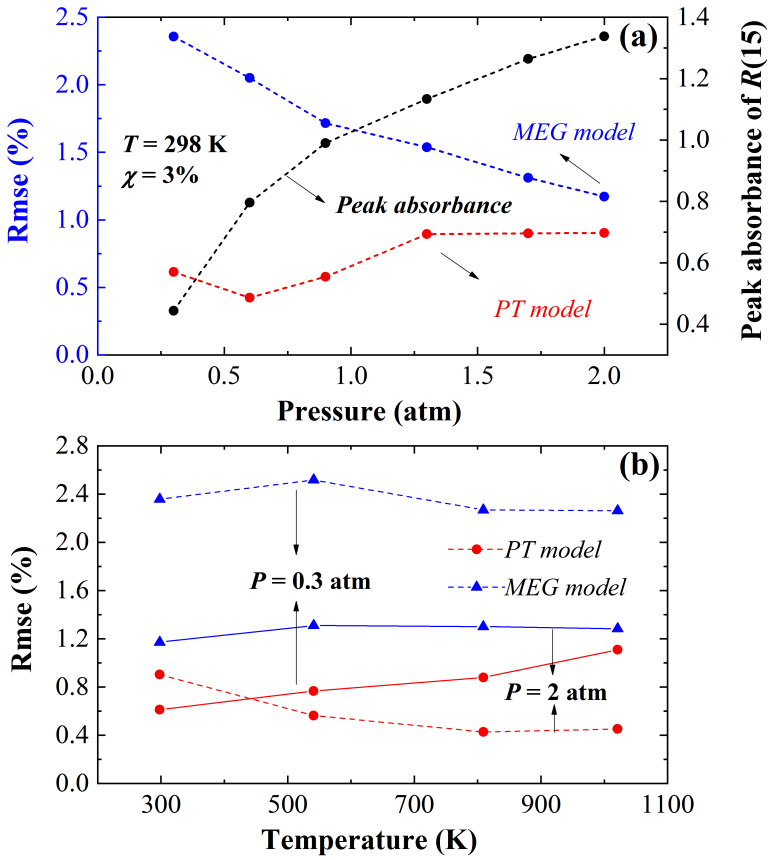

Figure 21 – (a) Root mean square error (RMSE) from the best-fits of the PT model and the MEG model at pressures from 0.3 atm to 2.0 atm at ambient temperature. (b) RMSE from the best-fits of the PT model and the MEG model at various temperatures (298 K, 541 K, 809 K and 1021 K) at 0.3 atm and 2.0 atm. RMSE calculated as % of the peak absorbance.

lineshape profile, as shown in Fig. 24. Similar to the room temperature results, the first-order line mixing model is shown to capture the spectra well at these higher temperatures, yielding low residuals near 3%. Line mixing coefficients at temperatures higher than 1050 K were measured in the shock tube. A representative measured absorbance and best-fit first-order line mixing model at 1610 K are shown in Fig. 25 with a simulation not accounting line mixing for reference.

An examination of the line mixing contributions by specific transitions, designated by C'' $\alpha'' \rightarrow \alpha'$, reveal notable differences among the clusters comprising the $R(15)$ manifold. The pressure dependencies of the line mixing coefficients obtained by the first-order PT model are displayed in Fig. 26 with polynomial fits for the transitions spanning $\nu = 3166.05\ \mathrm{cm}^{-1}$ to $3166.16\ \mathrm{cm}^{-1}$ in Fig. 26(a) and linear fits for the F_1 1→55 ($3166.727\ \mathrm{cm}^{-1}$) and F_2 1→54 ($3166.733\ \mathrm{cm}^{-1}$) transitions in Fig. 26(b). The line mixing coefficients increase dramatically as pressure increases, reaching 10^3 for the F_2 4→57 ($3166.08\ \mathrm{cm}^{-1}$) and F_2 4→58 ($3166.10\ \mathrm{cm}^{-1}$) transitions while the coefficients are approximately linear with pressure for the F_1 1→55 ($3166.727\ \mathrm{cm}^{-1}$) and F_2 1→54 ($3166.733\ \mathrm{cm}^{-1}$) transitions, achieving a much smaller magnitude. The pressure dependence of the line mixing coefficients at 1021 K is depicted in Fig. 27(a), demonstrating a nominal decrease and more linear dependence on pressures compared with the values at ambient temperature. In general, the line mixing coefficients with smaller magnitudes have a more linear pressure dependence, consistent with the approximation of the relaxation matrix in the first-order line mixing model based on perturbation theory; however, Eq. 14 does not appear valid in this regime, since the coefficients with larger magnitudes increase significantly and nonlinearly with pressure.

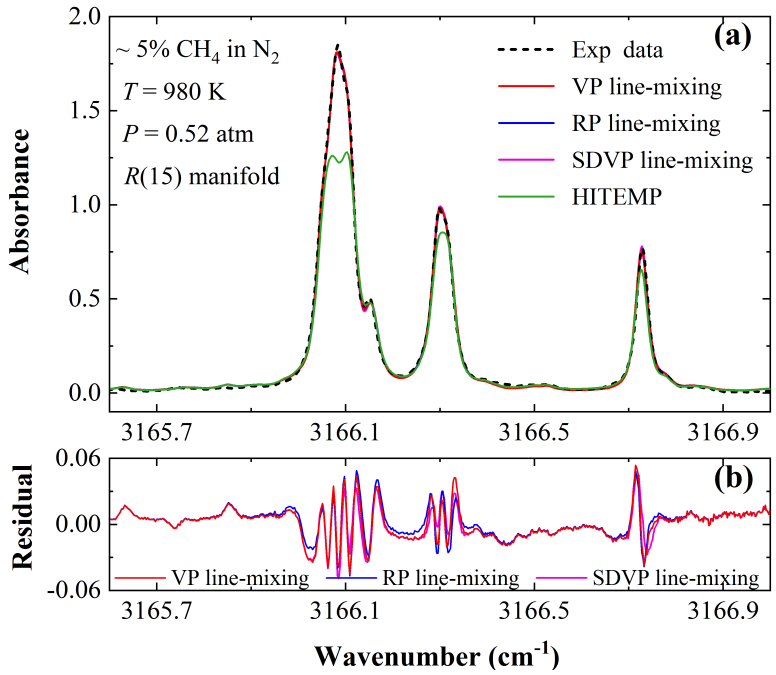

Figure 22 – (a) Measured absorbance of the $R(15)$ manifold at 980 K and 0.52 atm with corresponding best-fits from the first order line mixing model using Voigt, Rautian and speed-dependent lineshape profiles. Note: The air-broadening coefficients and their temperature exponents in HITEMP were used in place of N_2-broadening. (b) Residuals from the best-fit of the three models.

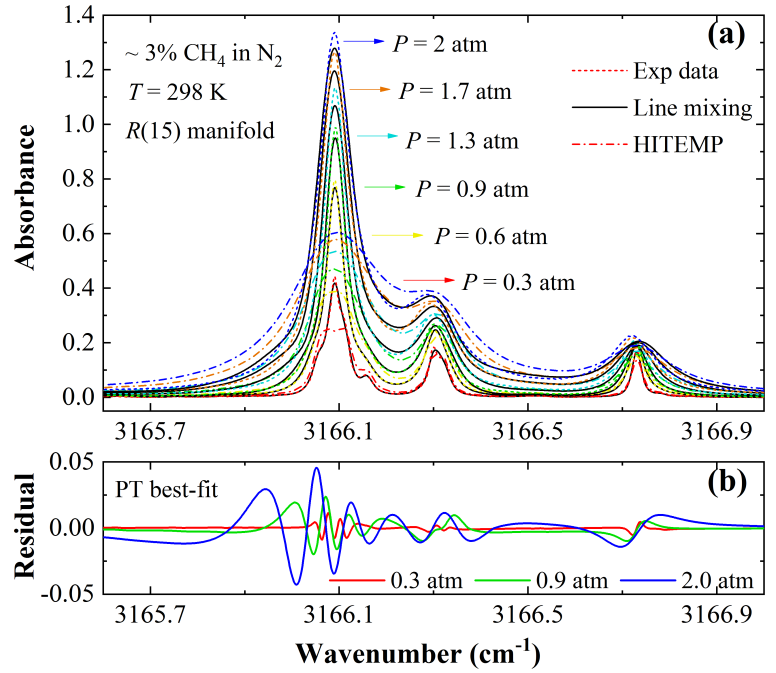

Figure 23 – (a) Measured absorbance in the $R(15)$ manifold from 0.3 atm to 2 atm at 298 K with corresponding best-fits from the first-order line mixing model using the Voigt profile. Predicted absorbance using HITEMP (not considering line mixing) also shown for reference. Note: The air-broadening coefficients and their temperature exponents in HITEMP were used in place of N_2-broadening. (b) Residuals for the pressures of 0.3 atm, 0.9 atm and 2.0 atm.

To check that the non-linear pressure dependence of the mixing coefficients was a not an issue of over-fitting too many free parameters, a multispectrum fitting routine [61] was used to fit the spectra over a range of pressures from 0.3 atm to 2.0 atm, constraining the pressure dependence of the line

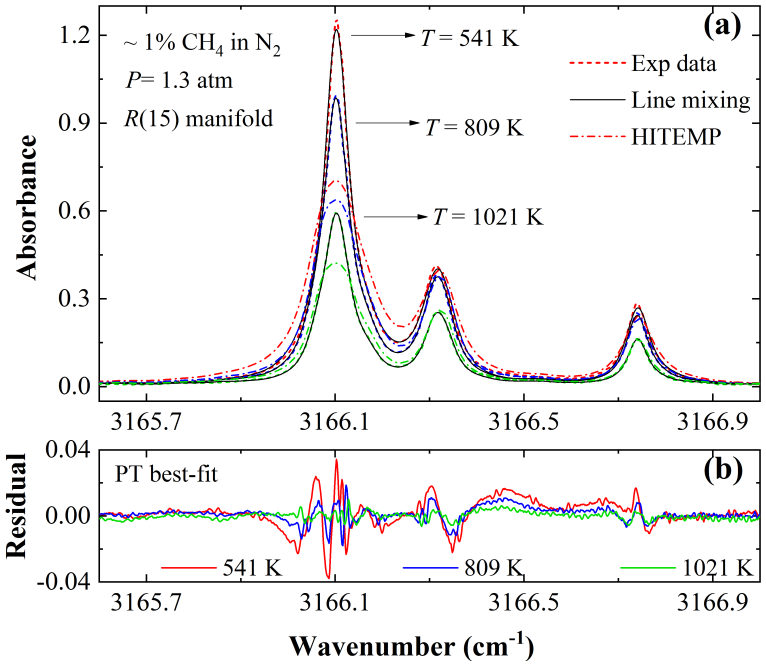

Figure 24 – (a) Measured absorbance of the $R(15)$ manifold at 541 K, 809 K and 1021 K and 1.3 atm with corresponding best-fits from the first-order line mixing model using the Voigt profile. Predicted absorbance using HITEMP (not considering line mixing) also shown for reference. Note: The air-broadening coefficients and their temperature exponents in HITEMP were used in place of N_2-broadening. (b) Residuals from the fits to the experimental data at each temperature.

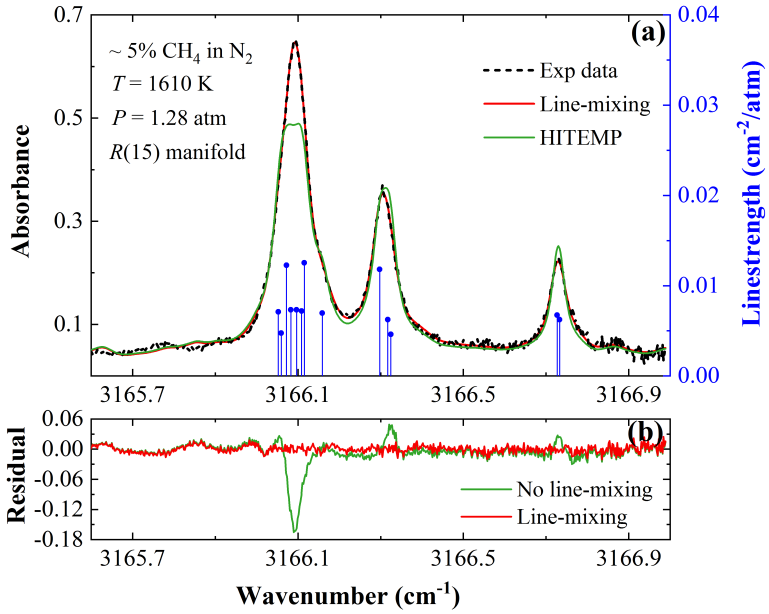

Figure 25 – (a) Measured absorbance of the $R(15)$ manifold at 1610 K and 1.28 atm with corresponding best-fits from the first order line mixing model using the Voigt lineshape profile. Predicted absorbance using HITEMP (not considering line mixing) is shown for reference. Note: The air-broadening coefficients and their temperature exponents in HITEMP were used in place of N_2-broadening. (b) Residuals from the fits with line mixing and calculations without line mixing.

mixing coefficients, with units of [atm^{-1}], to be strictly linear. However, the absorbance spectrum at each pressure could not be fit well, yielding peak residuals typically larger than 10%, reaching 20% at the lowest measured pressure of 0.3 atm. The nonlinear dependence of Y_i parameters on pressure

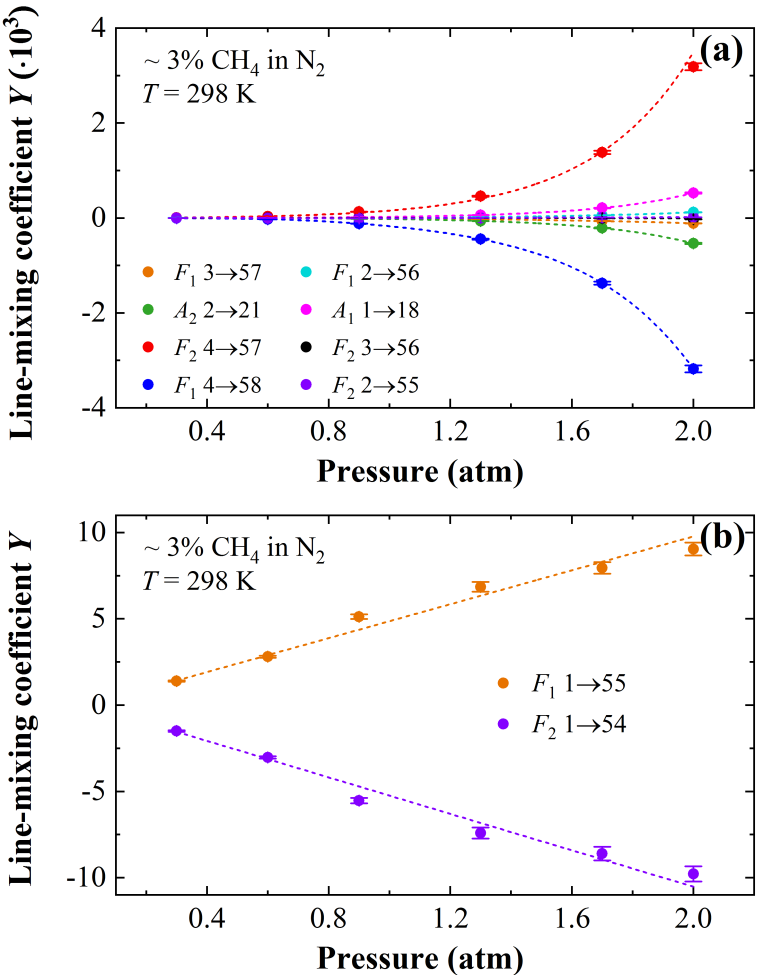

Figure 26 – Pressure dependence of the measured line mixing parameter Y_i given by the first order model using the Voigt profile for the transitions (a) spanning 3166.052 cm^{-1} to 3166.158 cm^{-1}. (b) F_1 1→55 at 3166.727 cm^{-1} and F_2 1→54 at 3166.733 cm^{-1}. Here, T = 298 K and the pressures from 0.3 atm to 2.0 atm.

is similar to the Dicke narrowing coefficients in Rautian and Galatry profiles [95, 96] with the growth rate increasing with increasing pressure. The retrieved Dicke narrowing coefficients also deviate from the dynamic friction coefficients due to the neglect of the correlations between velocity-changing and state-changing collisions [97], which is similar to the deviation between the measured Y_i parameters and the values calculated by the Eq. 14. Thus, a line mixing model based on first-order perturbation theory may not be sufficient to physically characterize the transitions exhibiting this nonlinear mixing behavior with increasing pressure, and a higher-order line mixing model may better describe the observed trends. Nonetheless, a modified first-order PT-based model (allowing for some non-linearity of Y_i parameters with pressure) captures the CH_4 line mixing satisfactorily, and may be more simply used as an empirical approach (as opposed to a higher order model) to simulate the spectra over a range of conditions, despite potential non-physicality.

These results may be further examined in the context of previous line mixing studies. The line mixing coefficients in the $R(15)$ manifold are observed to be relatively large, achieving values up to ~4.4 at 0.3 atm. These values are much greater than those in the lower J-manifolds, such as those measured by Ghysels et al [73], who observed a maximum line mixing coefficient of 0.5 among the transitions comprising the $R(6)$ manifold at atmospheric pressure and ambient temperature. Significant line mixing effects among the transitions comprising high-J'' manifolds (J'' >15)—such as $R(17)$ and $R(19)$—have also been documented by Grivoriev et al [68], who noted that the absorbance predicted

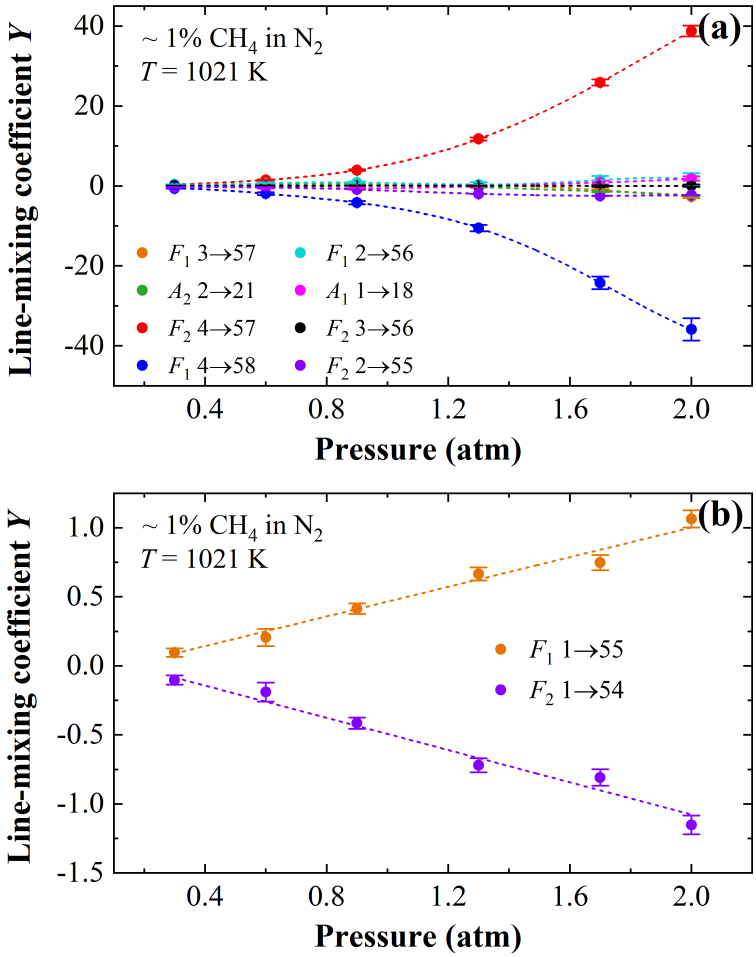

Figure 27 – Pressure dependence of the measured line mixing parameter Y_i given by the first order model using Voigt profile for the transitions (a) spanning 3166.052 cm^{-1} to 3166.158 cm^{-1}. (b) F_1 1⟶55 at 3166.727 cm^{-1} and F_2 1⟶54 at 3166.733 cm^{-1}. Here, T = 1021 K and the pressures from 0.3 atm to 2.0 atm.

by the summation of isolated lines underestimated the experimentally measured value by a factor of 2, similar to the results for the $R(15)$ manifold. The authors cautioned that the Y_i parameters obtained in the fit were unlikely to be reliable, despite that the calculated and observed absorbance were in good agreement [68]. Unlike the current work, no pressure or temperature dependence was investigated, precluding more detailed comparison beyond ambient conditions.

For the current work capturing the $R(15)$ manifold, Y_i parameters with their uncertainties at the pressures of 0.3, 0.6, 1.3 and 2.0 atm are presented in Table. 2. The listed uncertainties for each parameter are calculated according to the methods detailed in **??**. A polynomial fit may be implemented to describe the pressure dependence of Y_i, so that the parameters at pressures other than those listed in Table 2 can also be obtained. The temperature dependence exponent n in Eq. 29 for each line mixing parameter Y_i was determined by a power-law fit, using the Y_i parameters evaluated at atmospheric pressure. These empirical relationships readily enable calculation of spectrally-resolved absorbance in the $R(15)$ manifold for broader CH_4 sensing applications.

To test the validity of the empirical model, the line mixing parameters were used to calculate the absorbance at P = 0.97 atm and T = 298 K for comparison with the measured and calculated results from Tran et al [70] as shown in Fig. 28. As with the literature comparison for the MEG law coefficients, the spectrally-resolved absorption coefficient (α/P_{CH_4} [cm^{-1}/atm]) for $R(15)$ reported in that study was multiplied by the partial pressure of CH_4 and the pathlength of the experiments in

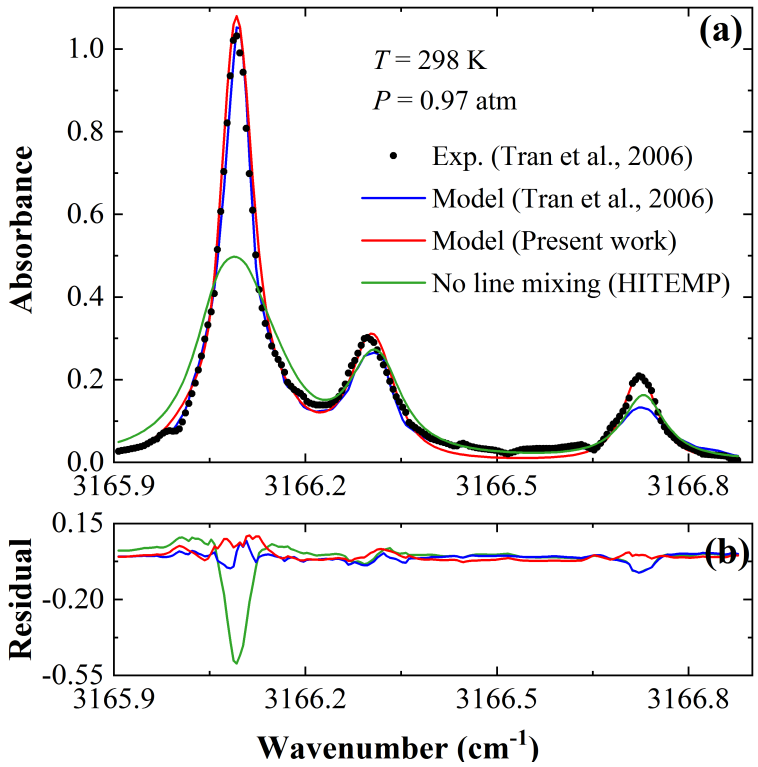

Figure 28 – (a) Absorbance (X = 0.03, L = 9.4 cm) calculated from the absorption coefficient α/P_{CH_4} [cm^{-1}/atm] reported by Tran et al [70] at P = 0.97 atm and ambient temperature for $R(15)$. Measured values (black points) shown alongside calculations by the model of Tran et al [70] (blue), the first-order model in the present work (red), and calculated values without line mixing (green). Note: The air-broadening coefficients and their temperature exponents in HITEMP were used in place of N_2-broadening in the present work while the N_2-broadening was deduced by multiplying the air-broadening in HITRAN by a factor of 1.02 [64, 70]. (b) Residuals from the two line mixing models and calculations without line mixing.

the present investigation to obtain a comparable spectral absorbance α_ν. As no experiments were conducted at exactly 0.97 atm in this study, the Y_i parameters for P = 0.97 atm were obtained using a 3-order polynomial fit of the parameters with respect to pressure at ambient temperature in Table. 2.

Table 2 – Measured first-order line mixing coefficient and temperature dependence for CH_4 $R(15)$ manifold.

J' C' α'	J'' C'' α''	ν [cm^{-1}]	Y_i (0.3 atm) [no unit]	Y_i (0.6 atm) [no unit]	Y_i (1.3 atm) [no unit]	Y_i (2.0 atm) [no unit]	n_0
16 F_2 57	15 F_1 3	3166.05235	0.05 ± 0.02	-0.43 ± 0.06	-27.39 ± 0.70	-112.83 ± 2.81	3.48
16 E 38	15 E 2	3166.05948	-0.54 ± 0.04	-2.20 ± 0.11	2.49 ± 0.48	14.00 ± 0.30	0.49
16 A_1 21	15 A_2 2	3166.07227	0.46 ± 0.03	-3.10 ± 0.10	-64.08 ± 2.31	-536.66 ± 15.75	3.41
16 F_1 57	15 F_2 4	3166.08286	4.38 ± 0.06	31.88 ± 0.30	457.90 ± 10.32	3185.10 ± 73.80	2.54
16 F_2 58	15 F_1 4	3166.09674	-4.29 ± 0.07	-26.99 ± 0.45	-446.09 ± 10.00	-3178.60 ± 73.48	2.54
16 F_2 56	15 F_1 2	3166.10877	0.73 ± 0.06	1.00 ± 0.31	16.73 ± 1.18	118.39 ± 2.36	3.53
16 A_2 18	15 A_1 1	3166.11530	-0.72 ± 0.03	2.17 ± 0.10	61.75 ± 2.26	526.22 ± 15.39	4.37
16 F_1 56	15 F_2 3	3166.15875	-0.03 ± 0.01	-0.30 ± 0.03	-1.26 ± 0.44	-25.41 ± 2.20	1.68
16 A_1 20	15 A_2 1	3166.29768	0.28 ± 0.01	0.91 ± 0.04	1.01 ± 0.03	1.17 ± 0.03	1.48
16 F_1 55	15 F_2 2	3166.31721	-0.96 ± 0.22	-3.74 ± 0.43	-0.23 ± 0.02	14.92 ± 0.53	1.05
16 E 37	15 E 1	3166.32460	0.55 ± 0.04	2.27 ± 0.11	-2.56 ± 0.50	-14.44 ± 0.31	0.49
16 F_2 55	15 F_1 1	3166.72679	1.38 ± 0.03	2.62 ± 0.06	6.95 ± 0.13	9.63 ± 0.37	2.23
16 F_1 54	15 F_2 1	3166.73280	-1.50 ± 0.04	-2.84 ± 0.07	-7.51 ± 0.15	-10.42 ± 0.44	2.23

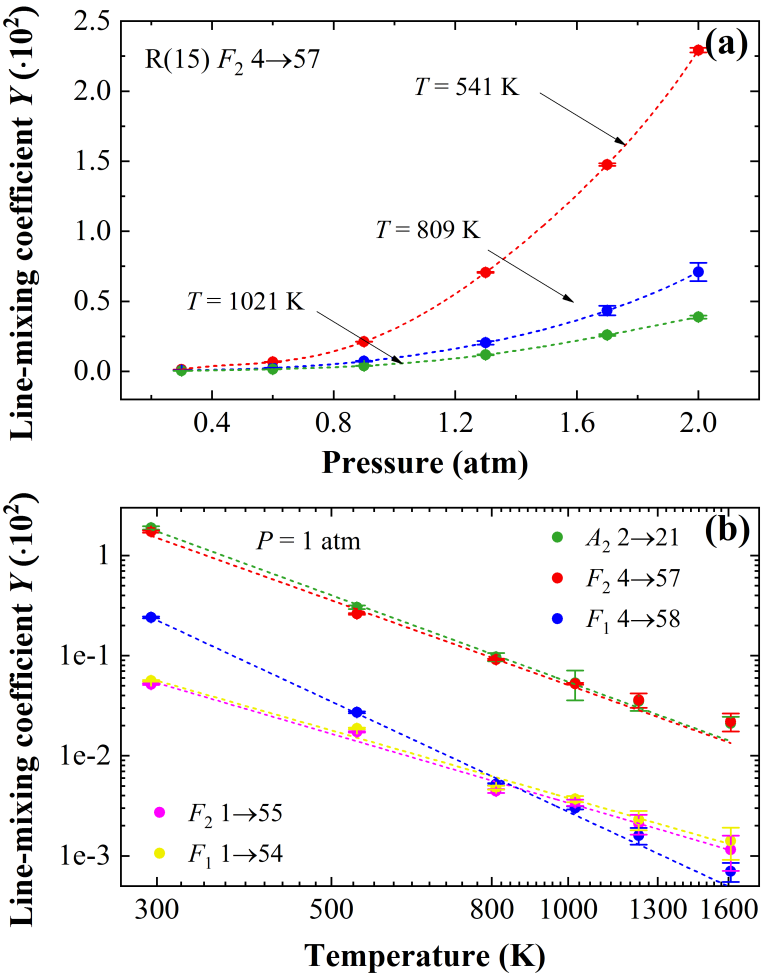

Figure 29 – (a) Pressure dependence of the line mixing parameter Y_i for the F_2 4⟶57 transition at various temperatures (298 K, 541 K, 809 K, 1021 K). (b) Temperature dependence of the line-mixing coefficients Y and power law fits for transitions (A_2 2⟶21, F_2 4⟶57, F_1 4⟶58, F_2 1⟶55, F_1 1⟶54) in the $R(15)$ manifold at 1 atm.

Graphical depictions of the polynomial fits used to obtain Y_i at 0.97 atm are shown in Fig. 26. The predicted spectrum from the first-order line mixing model in the present work is in good agreement with the absorbance measured by Tran et al [70] and shows some improved accuracy in capturing the effects of line mixing among the F_1 1⟶55 (3166.727 cm^{-1}) and F_2 1⟶54 (3166.733 cm^{-1}) transitions relative to the model presented in that study. It should be noted that the prior work was using an older and more sparse database. As expected, both models show much better agreement than the prediction which does not consider line mixing near the most prominent cluster of lines.

Finally, we examine the temperature dependence of the first-order PT-based model for the transitions comprising the $R(15)$ manifold based on data from both the heated gas cell and shock tube experiments. Fig. 29(a) shows the line mixing coefficient for the prominent F_2 4⟶57 transition near 3166.083 cm^{-1} at the temperatures 541 K, 809 K and 1021 K over the range of pressures studied. The magnitudes of the line mixing coefficients for this transition and the others decrease dramatically with increasing temperature, exhibiting a more approximately linear pressure dependence. Fig. 29(b) shows the line mixing coefficients determined at different temperatures spanning 298 K to 1610 K at P = 1 atm for several representative transitions in the $R(15)$ manifold. As discussed previously, the Y_i coefficients were fit with a power law using Eq. 29 to obtain the temperature-dependent exponent n for each transition, and the resulting fits are also plotted in Fig. 29(b). The power law formulation

captures the temperature dependence of the line mixing coefficients reasonably well, demonstrating its applicability for predicting CH_4 spectra across a wide range of temperatures. The temperature-dependent exponent n determined at atmospheric pressure for each transition is listed in Table 2 along with associated uncertainties calculated according to the methods detailed in **??**.

3. Conclusion

Empirically-derived line mixing parameters and associated temperature-dependence exponents are reported for the R branch of the v_3 band of CH_4 perturbed by N_2 in the 3024–3200 cm^{-1} region. Experiments were conducted over a wide range of temperatures from 300 K to 1600 K, utilizing a heated gas cell and a shock tube facility. High-temperature experiments were coupled with an FTIR survey of the R-branch from 2–25 atm and a more focused laser absorption spectroscopy investigation of the R(15) manifold at lower pressures. Two empirical models were tested and found appropriate for different ranges of gas density. A modified exponential gap (MEG) law, with manifold-specific coefficients, was found to capture line mixing in the R branch manifolds from $R(0)$ to $R(18)$ with very good accuracy at the higher pressures (<3% max residual at 25 atm) and increased error with decreasing pressure and gas density. Despite residual error, the MEG law model offers significant improvement over conventional modeling that neglects line mixing and reasonable agreement down to 2 atm, with temperature scalability to 1020 K. Line mixing of the $R(15)$ manifold was examined at lower pressures of 0.3–2 atm and at higher temperatures up to 1610 K using a narrow-band interband cascade laser. A first-order line mixing model based on perturbative treatment theory was developed to improve spectral simulation and scaling with temperature and pressure compared to the MEG law. The temperature dependence of the PT model coefficients follows the power law while the pressure dependence is nonlinear for some transitions in $R(15)$, and requires interpolation between pressure-specific coefficients for scaling. In aggregate, this work represents a novel investigation of CH_4 line mixing at elevated temperatures and, perhaps more importantly, the temperature-scalable empirical models which were developed in this work will enable quantitative interpretation of absorption spectroscopy measurements in high-temperature environments.

4. 3D Methane Imaging Utilizing Line Mixing Effects

4.1. Introduction

Laboratory-scale flames often serve as simplified experiments to develop and validate models of the coupling of transport phenomena and chemical kinetics for more complex combustion systems [**?**]. With regard to fuels, methane (CH_4) provides an accessible theoretical, experimental, and computational benchmark for understanding hydrocarbon combustion in flames. As a principal component of natural gas, an intermediate in the oxidation of larger hydrocarbons, and a potent greenhouse gas, CH_4 plays an outsized role in energy systems globally, and will remain important as the power and transportation sectors work to meet increasingly stringent emissions targets. As such, the spatial and temporal evolution of CH_4 in flames (as a fuel, intermediate, or byproduct) is of acute interest in combustion research, and methods with which to non-intrusively and quantitatively assess CH_4 evolution in flames are needed for model development and validation.

Despite the high level of methane utilization for fundamental combustion and flame studies, there is a relative dearth of diagnostic methods available for quantitative and spatially-resolved in situ CH_4 detection. With careful optical filtering, calibration, and an estimation of gas composition, Raman scattering techniques have provided quantitative CH_4 concentration in select flame environments [**? ? ? ?** 98]. However, the relatively very weak Raman cross-sections for CH_4 require cumbersome and costly high power light sources that yield localized point or line measurements with

spatial resolution limited by the opto-mechanical translation of the experiment. Although historically weak in spatial resolution capability due to its line-of-sight measurement, laser absorption spectroscopy (LAS) offers a highly quantitative and calibration-free technique for non-intrusive species and temperature sensing [32]. Coupled with tomographic reconstruction methods—LAS has enabled some quantitative multidimensional measurements of CH_4 in select combustion flows with compact, low-power sources [99, 100]. Using near-infrared sources and a multiplicity of laser lines-of-sight, this approach provides somewhat coarse spatial resolution relative to the thin (mm) reaction zones of flames. Recently, our group introduced a mid-infrared laser absorption imaging (LAI) technique, with application to hydrocarbon fuels via access to the fundamental C-H stretch vibrational bands, enabling flame scale (< cm) application [28, 30, 24]. This method provides species-specificity and very high spatial resolution (<100 μm) via 2D imaging of an expanded laser beam, but has lacked quantitative interpretation due to complexities in the convoluted spectral line clusters and their acute temperature dependence within flames.

In this work, we employ volumetric laser absorption imaging in conjunction with a temperature-dependent spectral line-mixing model for the ν_3 band of methane to obtain quantitative, simultaneous temperature and methane spatial distributions within laboratory-scale flames. We first describe the methods, including the volumetric LAI optical setup and line-mixing model, as well as the tomographic data interpretation techniques used to obtain temperature and concentration field distributions. We then demonstrate the diagnostic method experimentally on a non-axisymmetric methane-oxygen laminar flame doublet, examining variations in requisite projection angles and regularization constraints to produce high-resolution quantitative 3D images of methane and temperature in the fuel decomposition regions of partially premixed flames.

4.2. Methods

4.2.1. Volumetric Laser Absorption Imaging

Laser absorption tomography (LAT) is a non-intrusive diagnostic method that enables spatially-resolved thermochemistry measurements in reacting flows from a multitude of lines of sight [1]. Recent advances in mid-wave infrared lasers have enabled LAT at the fundamental vibrational frequencies of many combustion species of interest, facilitating high-sensitivity detection [101, 102] and enabling quantitative investigations of small-diameter (<1 cm) flames [103, 104, 36]. Laser absorption imaging (LAI) is a complimentary method designed to capture scenes backlit with tunable laser radiation at very high spatial resolution using high-speed infrared cameras to yield spatio-temporally rich datasets, typically with thousands of lines of sight collected simultaneously [28]. Fig. 30 shows the LAI optical setup used in this work.

4.2.2. Optical Setup

The experimental configuration for this study was adapted from previous demonstrations of LAI by our research group [28, 30, 24] and utilizes a high-speed infrared camera (Telops FAST-M3K) to image a flowfield backlit with tunable laser radiation in the mid-wave infrared, as shown in Fig. 30. An interband cascade laser (ICL) near 3.16 μm (Nanoplus GmbH) with a nominal output power of 15 mW is used to scan across the R(15) manifold of the R-branch of the ν_3 band of methane [105]. The beam is horizontally expanded with a cylindrical lens and re-collimated with a concave mirror, then pitched through the flow-field comprising two Bunsen-style flames, each with flame brushes approximately 3 mm in diameter. The beam is spectrally isolated with a bandpass filter (Spectrogon, 3160 ± 60 nm), and a plano-convex lens focuses the expanded beam onto the detector array of the camera. The beam

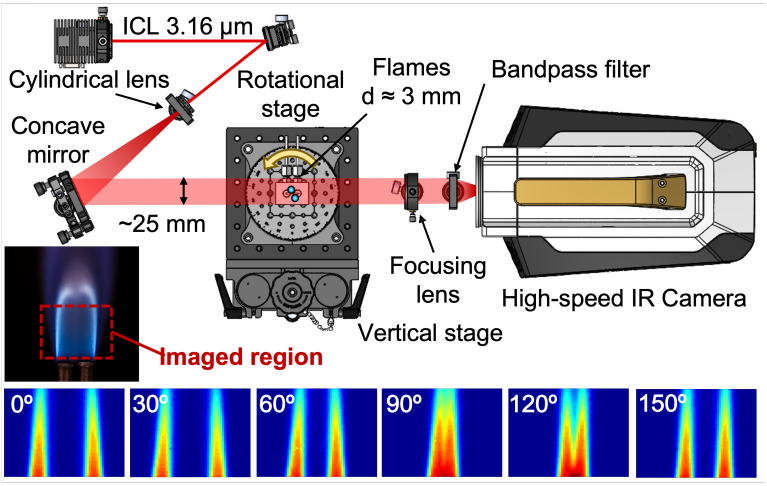

Figure 30 – Optical setup for this work, showing ICL beam alignment through the cylindrical lens, concave mirror, laminar flame doublet mounted atop translation stage assembly, focusing lens, and bandpass filter into camera detector array and corresponding transmission image. Resulting projected absorbance images of CH_4 shown as insets with respective angle of the Bunsen-style flames.

is captured in the camera detector subwindow of size 64×48 pixels with a frame rate of 40 kHz and integration time of 5 μs. The laser is injection-current tuned using a sawtooth waveform at 400 Hz, resulting in 100 points per scan for subsequent spectral fitting. The camera frame rate is maximized while maintaining a subwindow large enough to capture the flowfield of interest. The laser scan rate is selected to mitigate diffraction noise [30] while allowing for adequate spectral resolution at the camera frame rate. For each projection angle measurement, data are collected at two heights using a vertical translation stage and later combined after deleting overlapping pixels, yielding 64×72 lines of sight to capture the whole flame brush. A total of 6 projection angles (evenly distributed within a total 150° angle segment) were collecting, yielding an aggregate of 27,648 unique lines of sight. Each projection image is collected and averaged over 1 s (400 scan average), an interval over which the flames are assumed steady. Spatial resolution was evaluated by imaging a wire mesh with known dimensions backlit with laser light [29], and was determined to be ~70 μm per pixel in both horizontal and vertical direction.

4.2.3. Masked 3D Tikhonov Regularization

The Beer-Lambert law in Eq. 24 provides the spectrally-dependent absorbance α_ν in a gas medium along a line-of-sight l [cm] for a specific frequency ν [cm^{-1}] as a function of the ratio of incident intensity, I_0, and the transmitted intensity, I_t, of the laser light through the gas [1]:

$$\alpha_\nu = -\ln\left(\frac{I_t}{I_0}\right)_\nu = \int_0^L \kappa_\nu(l)\mathrm{d}l \tag{24}$$

α_ν depends on the line-of-sight-integration (over aggregate pathlength L [cm]) of the local spectral absorption coefficient, κ_ν [cm^{-1}], which is in turn dependent on the local thermodynamic conditions (e.g., temperature, pressure, gas composition) at position l and frequency ν. The path-integrated nature of LAS requires that local values of $\kappa_\nu(l)$ must be inferred from measurements of α_ν, and in this study the gas medium is not spatially uniform over L.

For the LAI optical setup shown in Fig. 30, Eq. 24 applies to the line-of-sight collected by *each* camera pixel, resulting in 2D images for α_ν, as shown in Fig. 31. Volumetric tomography aims

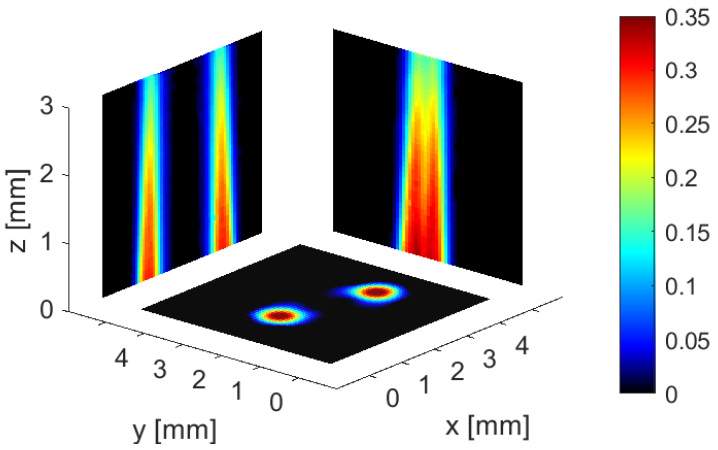

Figure 31 – Schematic showing 2 orthogonal projection measurements α_{ν_A} and reconstructed local absorbance from 6 projection angles at plane z = 1.56 mm.

to reconstruct the 3D field of local absorbance coefficients κ_ν from 2D projection measurements α_ν. In this case, the flow field is discretized into a $64 \times 64 \times 72$ cubic voxels probed by 64×72 parallel lines of sight from 6 projection angles. Writing Eq. 24 for all $6 \times 64 \times 64$ lines of sight in a given plane yields a system of linear equations:

$$\mathbf{W}\boldsymbol{\kappa}_\nu = \boldsymbol{\alpha}_\nu \tag{25}$$

where $\boldsymbol{\alpha}_\nu$ contains projection measurements and $\boldsymbol{\kappa}_\nu$ represent 3D field of discrete absorption coefficients, respectively, both in vector form. $\mathbf{W}$ is the 3D projection weight matrix, where W_{ij} represents the absorption length for the ith beam passing through the jth voxel. Due to limited-angle measurements, matrix $\mathbf{W}$ is rank-deficient (and inherently ill-posed), which is typically addressed with Tikhonov regularization [1, 106, 13]. In this approach, the rank-deficient matrix equation is augmented by a second set of equations, $\lambda\mathbf{L} = 0$, and the local absorbance field κ_ν is determined by find the least-squares solution to the combined set of equations:

$$\boldsymbol{\kappa}_{\nu,\lambda} = \arg\min \left\| \begin{bmatrix} \mathbf{W} \\ \lambda\mathbf{L} \end{bmatrix} \boldsymbol{\kappa}_\nu - \begin{bmatrix} \boldsymbol{\alpha}_{\nu,\text{proj}} \\ 0 \end{bmatrix} \right\| \tag{26}$$

where $\mathbf{L}$ is the discrete 3D gradient matrix [9] that is used to enforce the smoothness condition and n_i is the number of neighboring pixels. λ is the regularization parameter that controls the relative importance of the smoothness term compared to the residual norm. In this study, λ was chosen to yield a value that pads the small singular values but does not overwhelm the large nontrivial singular values [106].

To further address the ill-posed inversion problem, a 3D masking method [9] is applied to constrain the reconstruction volume. In this approach, 2D masks are defined by the user (by setting a threshold value) on the projected absorption area images and backprojected into a 3D mask as shown in the black regions of Fig. 31. Projection data below the threshold associated with nonvalid rays, and the corresponding rows of the weight matrix $\mathbf{W}$, are deleted from the optimization process per equation 26. In this study, the suitable masking threshold was chosen to yield a solution residual norm within 1% of the baseline residual norm from the regularization [9]. This process is not only useful for reducing the blurring effects from Tikhonov regularization, but also helps to confine the artifacts in the reconstructed volumes as demonstrated in previous volumetric reconstruction measurements [107, 9]. To account for the effects of the discretization of the domain and the regularization methods on the

final spatial resolution, numerical studies [24] have been conducted by the authors using sharp-edge phantom fields that are similarly distributed as the targeted flame doublet. Following the modulation-transfer-function (MTF) based definition [**?** **?**], the final spatial resolution from reconstruction is estimated by setting a 10% threshold on the MTF of the reconstructed edge and is determined to be ~200 μm. 3D distributions of temperature and mole fraction can then be determined by fitting the local spectra κ_ν using a line-mixing model for each voxel, as detailed in Sections 2.2 and 2.3.

4.3. Line Mixing Spectral Model

Though the simplest stable hydrocarbon, CH_4 poses many spectroscopic modeling challenges, particularly at elevated temperatures and pressures. Despite recent availability of computationally-tractable high-temperature line lists for CH_4 [59], significant disagreement in spectral absorbance—relative to predictions by conventional lineshape summation of individual transitions—can be observed for measured CH_4 spectra at even ambient pressures and temperatures. This is largely attributed to *line mixing*, a band- or manifold-narrowing effect in spectrally dense regions caused by collision-induced changes in the populations of energy states [60]. In this work, we take advantage of line mixing effects to enhance the sensitivity of temperature measurements within the narrowband tuning range of a distributed feedback interband cascade laser.

When targeting the R(15) manifold in the v_3 band of CH_4, quantitative inference of methane mole fraction and temperature requires an accurate model of line mixing effects. The governing equations of line mixing and associated spectroscopic data at elevated temperatures for the R-branch of the v_3 band of CH_4 are detailed extensively in a prior work [105], and so we only briefly review key elements here for reader comprehension of the imaging strategy. The spectral absorption coefficient, κ_ν, can be written within the impact approximation accounting for first-order line mixing effects and assuming a Voigt lineshape profile [60]:

$$\kappa_\nu = N \sum_i \left(\frac{S_i(T)}{\Delta\nu_{D,i}}\right)\sqrt{\frac{\ln(2)}{\pi}}\times \\ (\mathrm{Re}[c(\nu, x_i, y_i)]+Y_i \cdot \mathrm{Im}[c(\nu, x_i, y_i)]) \tag{27}$$

where N [molec·cm^{-3}] is the number density, $S_i(T)$ [cm^{-1}/(molec.·cm^{-2})] is the temperature-dependent linestrength, and $\Delta\nu_{D,i}$ [cm^{-1}] is the Doppler half-width for each spectral line i of the absorbing species. c is the complex error function, with:

$$x_i = \frac{\nu - \nu_{0,i} - \delta_i}{\Delta\nu_{D,i}}\sqrt{\ln(2)} \\ y_i = \frac{\Delta\nu_{c,i}}{\Delta\nu_{D,i}}\sqrt{\ln(2)} \tag{28}$$

$\nu_{0,i}$ [cm^{-1}], $\Delta\nu_{c,i}$ [cm^{-1}], and δ_i [cm^{-1}] are the linecenter, collisional width, and pressure shift, respectively, for each transition i. Transition linestrength, $S_i(T)$, as well as $\nu_{0,i}$, $\Delta\nu_{c,i}$, and δ_i are obtained from the HITEMP database [59], with only air- and self-broadening considered in the calculation of $\Delta\nu_{c,i}$. Y_i is the dimensionless line mixing coefficient accounting for the influences of nearby transitions j within the same manifold, such that $j \neq i$. The temperature dependence of the line-mixing parameter Y_i is approximated by a power law,

$$Y_i(T) = Y_i(T_0)\left(\frac{T_0}{T}\right)^{n_i} \tag{29}$$

where n_i is a temperature-dependent exponent and $Y_i(T_0)$ is the value of Y_i at a reference temperature of T_0=296 K. Values of $Y_i(T_0)$ and n_i for 13 CH_4 transitions comprising the spectral domain of interest have been determined previously [105], and can be used to model the spectral absorption coefficient of the R(15) manifold of CH_4 from 296 K to 1600 K.

Fig. 32 shows spectral absorbance by CH_4 in a heated optical gas cell with an N_2 bath gas at 800 K and 0.9 atm alongside predictions both considering and neglecting line mixing. Notably,

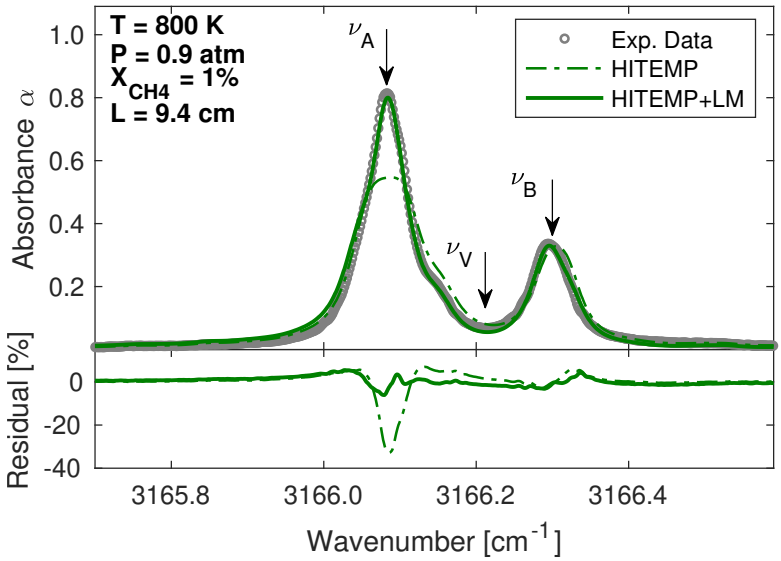

Figure 32 – Measured absorbance in the $R(15)$ manifold at 0.9 atm and 800 K in a heated optical cell, alongside predictions with and without the line-mixing model by Li et. al [105] and corresponding residuals. Frequencies used for ratiometric thermometry annotated by ν_A, ν_B, and ν_V.

neglecting line mixing results in under-prediction of peak absorbance near ν_A=3166.1 cm^{-1} by over 20% at 800 K. When accounting for line mixing, the peak absorbance near ν_B=3166.3 cm^{-1} and local minimum absorbance near ν_V=3166.2 cm^{-1} are only moderately under-predicted and over-predicted, respectively. Clearly, line mixing in this spectral domain must be considered to provide reasonably accurate and quantitative LAS-based measurements of temperature and CH_4 concentration in the decomposition regions of flames.

4.4. Ratiometric thermometry and spectral fitting

With a temperature- and concentration-scalable spectral model for κ_ν established, the measured and reconstructed fields of κ_ν can be interpreted to yield fields of temperature and CH_4 concentration. Previous demonstrations of LAI have used ratios of measured spectrally-integrated absorption coefficients to determine flowfield thermochemistry (temperature, mole fraction) [28, 9]; however, such an approach was not sufficiently robust to reliably extract flowfield thermochemistry in this study, because the targeted R(15) manifold transitions all possess similar lower state energies (between E_i'' = 1250.83 cm^{-1} and E_i'' = 1252.07 cm^{-1}). To overcome this challenge, we developed a ratiometric thermometry method which leverages the temperature sensitivity (caused by temperature-dependent line mixing) of the absorption feature near ν_A and temperature-insensitive feature near ν_B shown in Fig. 32 to obtain the thermochemistry of the reacting flowfield.

A ratio of the relative peak-to-valley spectral absorption for ν_A and ν_B relative to ν_V for a given location l can be defined by:

$$R(l) = \frac{\kappa_{\nu_A}(l) - \kappa_{\nu_V}(l)}{\kappa_{\nu_B}(l) - \kappa_{\nu_V}(l)} \tag{30}$$

Fig. 33 shows simulated values of R as a function of temperature for cases both considering and neglecting line mixing effects, alongside corresponding numerically-computed values of normalized temperature sensitivity, $(dR/R)/(dT/T)$. It can be noted that including line mixing effects is shown

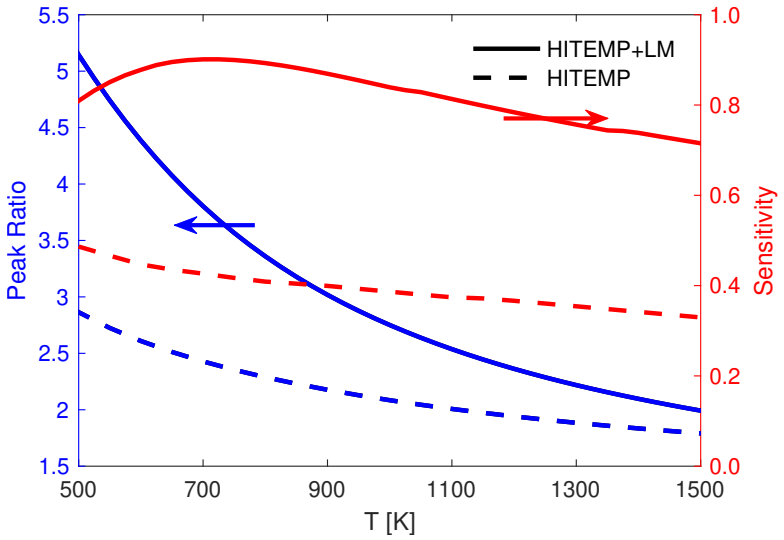

Figure 33 – Peak ratio and temperature sensitivity as function of temperature

to increase R by over 25% at 1100 K and over 50% at 500 K, yielding a larger change in R over the temperature range. Correspondingly, the temperature sensitivity is approximately doubled from 600–1500 K, providing for sensitive temperature measurements over the target temperature range for fuel decomposition and preheating in flames. R is only weakly dependent on CH_4 mole fraction, as shown in Fig. 34, owing to the influence of self-broadening at elevated concentrations of CH_4 on κ_ν at ν_A, ν_B, and ν_V. Thus, spectrally-resolved measurements of local absorption in different regions of the reacting

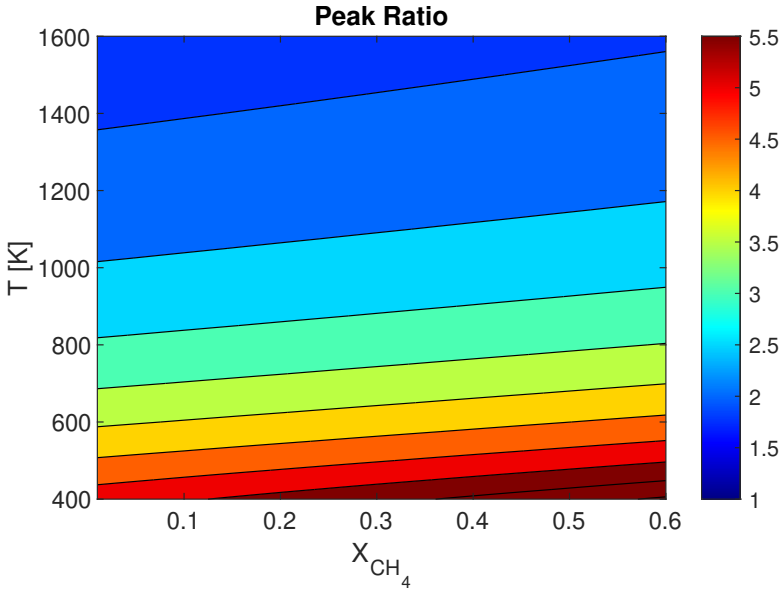

Figure 34 – Peak ratio as a function of temperature and mole fraction.

flowfield provide for sensitive temperature measurements even if local CH_4 mole fraction is unknown *a priori*. The foregoing analysis indicates a clear increase in temperature sensitivity (particularly with regards to ν_A) associated with line mixing effects, which is utilized in this measurement strategy for enhanced thermometry.

A ratiometric technique is coupled with spectral fitting to obtain the flowfield thermochemistry at every spatial location l. We first compute $R(l)$ from the reconstructed fields of $\kappa_\nu(l)$ and compare these observations to values of $R(l)$ simulated assuming X_{CH_4}=0.4, providing for an initial temperature uncertainty of ~ ±100 K. Regions with very low $\kappa_\nu(l)$ (SNR < 5 for κ_{ν_B})—typically in the regions of the flames where CH_4 has largely been consumed—were excluded from this calculation owing to non-physical results. Following this, we fit the line mixing model described in Section 2.2 to the observed spectra, with CH_4 mole fraction X_{CH_4} and a broadening multiplier for all $\Delta\nu_{c,i}$ as free parameters and temperature and pressure as fixed parameters. The broadening multiplier—applied to all transitions i equally—accounts for collision partners other than air or CH_4 in the reacting flowfield, and was found to be ~1.3 throughout most of the flowfield in this study, which corresponds with most combustion species having a higher broadening coefficient than nitrogen. Representative spectral fits on experimentally-obtained κ_ν and accompanying residuals are shown in Fig. 35 for two locations in the flame, demonstrating that the temperature-dependent line mixing model can adequately describe the observed spectra.

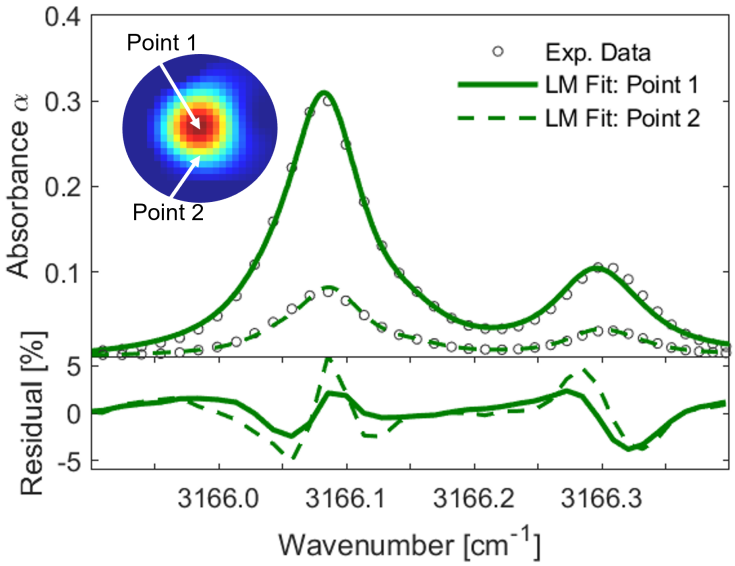

Figure 35 – Reconstructed spectra and corresponding spectral fits for two points in the plane at z = 1.56 mm, with (1) a high CH_4 concentration near the flame center, and (2) a lower CH_4 concentration away from the flame center.

4.5. Results

4.5.1. Demonstration on 3D flame doublet

The quantitative methane and temperature imaging method was demonstrated and evaluated experimentally on a partially-premixed methane-oxygen flame doublet. The flame pair was mounted on a rotational stage to image the flow-field from a variety of angles, as shown in Fig. 30. The partially premixed flames were controlled via thermal mass flow controllers (MKS MFC GE50A) with combined reactant flow rates of 150 sccm CH_4 and 100 sccm O_2. This corresponds to a fuel-rich mixture with a molar fuel-oxygen equivalence ratio of $\phi \approx 3$ prior to mixing with ambient air. After the flows were split to the two burners, one flow was measured with a rotameter to ensure equal flow through each burner. The exit velocity of each flow was 0.33 m/s and the jet exits of the stainless steel burners were 1.6 mm in diameter, providing a laminar jet Reynolds number of ~36.

Experimental volumetric laser absorption imaging of temperature and CH_4 mole fraction are

shown in Figs. 36 through 38 using the methods discussed in Section 2. Neither temperature nor mole fraction were resolved in regions with very low absorption coefficient (SNR < 5 for κ_{ν_B}), and these regions are not plotted for clarity. Quantitative 3D LAI results for CH_4 mole fraction and temperature are shown in Fig. 36 based on six projection angles. Specific $x-z$, $y-z$, and $x-y$ planes have been

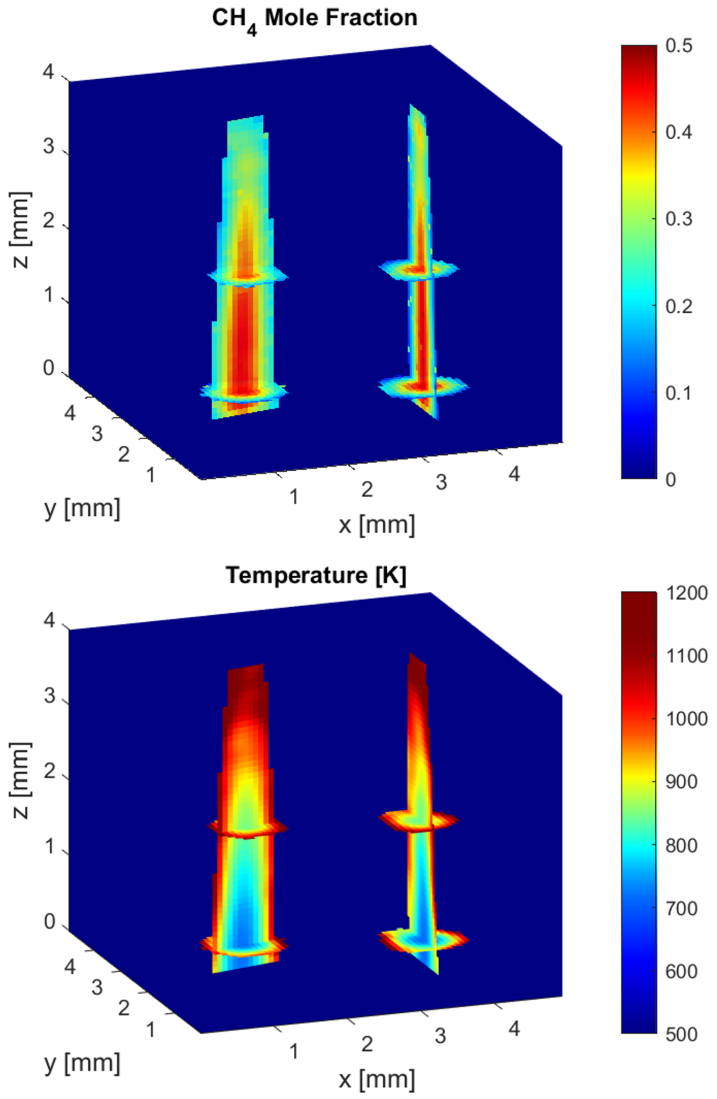

Figure 36 – Three-dimensional tomographic reconstructions of CH_4 *(top)* and temperature *(bottom)* generated from six unique projection angles. Specific x-z, y-z, and x-y planes have been highlighted to display internal flame structure.

highlighted in Fig. 36 to display cross-sectional flame structure. It is observed that the concentration of CH_4 drops rapidly in the flame as temperature increases above 900 K. The CH_4 in the reacting flowfield is confined into relatively small jets in the flames' centers, despite the significant overlap of the flame brushes seen in the photographic inset of Fig. 30. Moreover, the 3D images produced by the VLAI technique have a high enough spatial resolution to indicate that the CH_4 jets tilt slightly towards one another, possibly due to buoyancy-induced flow acceleration in the center of the overlapping flame brushes.

4.5.2. Influence of view angles

In laser absorption tomography, increasing the number of projection angles generally improves spatial resolution and the ability to resolve steep thermochemical gradients associated with the reaction zones of flames [9]. In this subsection, the effect of number of projection angles is examined. As a benchmark, a Tikhonov-regularized Abel inversion [6] was applied to a projection measurement of an isolated single flame to reconstruct the radial temperature and mole fraction profiles assuming steady, axisymmetric conditions. These reference profiles were positioned at the measured centroid of each flame within the doublet configuration. Notably, comparison with this Abel inversion reference is only valid at low z planes where interaction between the two flames is minimized. The reference is compared to those generated by 3D masked Tikhonov regularization using both six and three projection angles in Fig. 37 for a representative 2D cross section. It can be seen that incorporating

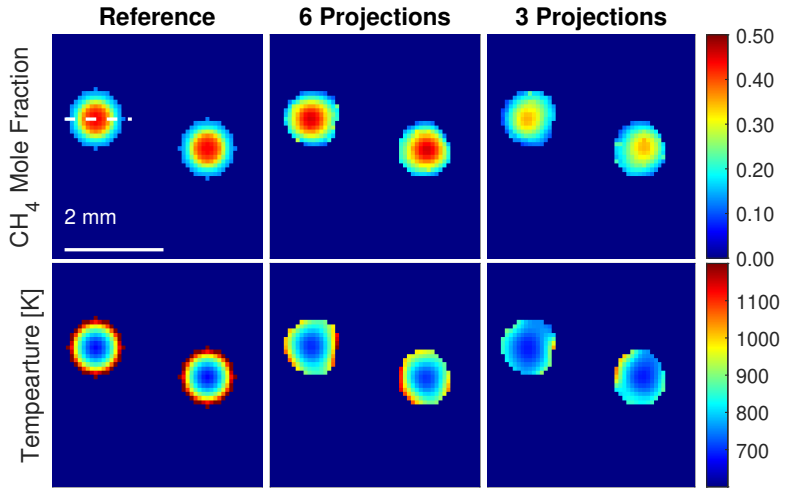

Figure 37 – Comparison of reconstruction accuracy for mole fraction *(top)* and temperature *(bottom)* of the z = 1.56 mm horizontal plane with 1D Abel inversion as a reference *(left)*.

additional projection angles into the reconstruction results in high spatial gradients in mole fraction and temperature that are more representative of the reference reconstruction.

To better compare the reconstruction quantitatively, we can plot the thermochemistry as a function of distance from a single flame's axis of symmetry. Fig. 38 compares 1D radial profiles of temperature and CH_4 mole fraction for a single flame in the flow, obtained from both 3D Tikhonov regularization and reference Abel inversion. The 1D radial profiles from 3D tomography were generated using the 1D profile marked by the white line on Fig. 37. Six projection angles were found to reduce the differences between the 3D regularization results and the reference reconstruction as well as resolve high spatial gradients within the flame compared to the result using three projection angles. The steep spatial gradients associated with the methane and temperature profiles resolved with this technique imply a spatial resolution of ~200 μm is achieved.

4.5.3. Quantitative references

While the flow-field examined here is not perfectly known, some reference quantities can be compared to the results. In the left of Fig. 38, the reconstructed temperature field from VLAI of CO in the flames [9] using 11 projection angles is provided for reference for regions with sufficient CO absorbance (SNR > 5). The temperature fields agree within experimental uncertainty (see Section 3.4 for details) in the overlapping regions, providing confidence in the line mixing model employed for CH_4, and highlighting a former gap in measurement capability filled by this imaging strategy.

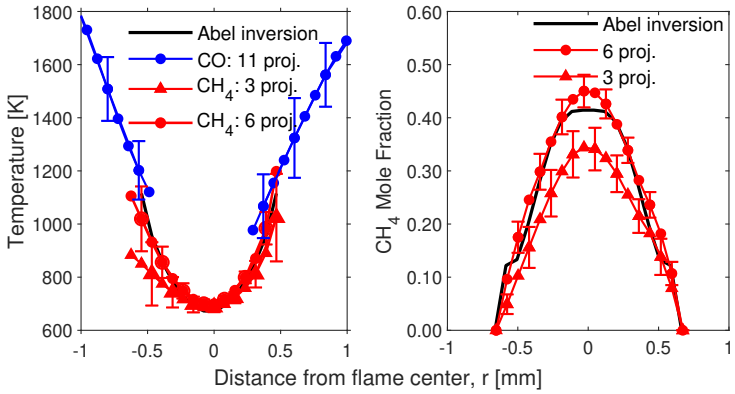

Figure 38 – One-dimensional radial profiles of temperature *(left)* and CH_4 mole fraction *(right)* generated from different number of projection angles compared to reference profiles generated from the Abel transform. Temperature measurement from CO in same the flames using 11 projection angles is also provided for reference.

Regarding the species fields, for an equivalence ratio of $\phi \approx 3$, we expect the maximum possible mole fraction leaving the burner to be $X_{CH_4} \approx 0.6$; however, the actual mole fraction is expected to be lower given mixing with ambient air prior to combustion. A maximum reconstructed value of $X_{CH_4} \approx 0.47$ was observed in the flow-field, corroborating this expectation.

4.6. Uncertainty analysis

In this paper, we follow the Taylor series method (TSM) of uncertainty propagation presented in previous LAT works [104, 36]. In this work, the temperature is measured by comparing the field of reconstructed peak-to-valley ratio R defined in Eq. 30 to the modeled ratio. Therefore the temperature uncertainties were calculated considering both uncertainties:

$$\left(\frac{\Delta T}{T}\right)^2 = \left[\left(\frac{\Delta R_{rec}}{R_{rec}}\right)^2 + \left(\frac{\Delta R_{model}}{R_{model}}\right)^2\right] \times \left(\frac{dT/T}{dR/R}\right)^2 \tag{31}$$

where ΔR_{rec} is the uncertainty in reconstructed ratio associated with a flow-field orientation uncertainties of ± 1°from the rotational stage [108], and ΔR_{model} is the uncertainty in modeled ratio due to the pre-assumed mole fraction. The uncertainties in mole fraction can then be calculated using Eq. 32 based on the line-mixing model in Eq. 27:

$$\left(\frac{\Delta X_{\text{abs}}}{X_{\text{abs}}}\right)^2 = \left(\frac{\Delta \kappa_\nu}{\kappa_\nu}\right)^2 + \left(\frac{\Delta S_i(T)}{S_i(T)}\right)^2 + \left(\frac{\Delta Y_i}{Y_i}\right)^2 \tag{32}$$

where $\Delta\kappa_\nu/\kappa_\nu$ accounts for uncertainty in reconstructed spectra associated with the flow-field orientation uncertainties, $\Delta S_i(T)/S_i(T)$ accounts for linestrength uncertainties from the HITEMP database as well as temperature uncertainties, and $\Delta Y_i/Y_i$ is the uncertainty from the line-mixing coefficients reported by Li et al [105]. Representative uncertainties of temperature and mole fractions are plotted as error bars in Fig 38, with typical values of ± 50–150 K and ± 6–10%, respectively.

4.7. Conclusion

This work involved the development and demonstration of a high-resolution quantitative volumetric laser absorption imaging technique for methane and temperature with application to laboratory flames. The technique utilizes and accurately accounts for complex spectral line mixing effects in order to enable sensitive and quantitative measurements in the preheat and fuel decomposition zones of flames. Quantitative VLAI of methane in such flame regions fills a gap in existing imaging capability, with significant advantages in spatial resolution, dimensionality, and accessibility relative to established Raman scattering methods. Targeting the community's benchmark hydrocarbon fuel and an important intermediate for larger hydrocarbons, this method will enable many new studies seeking to develop and validate combustion models of the coupling of transport phenomena and chemical kinetics. To expand the volumetric LAI method to time-resolved capability, as has been demonstrated previously in two dimensions [30], multiple projection angles must be imaged simultaneously and adaptations of regularization methods [109] are needed to resolve more complex flowfields.

Project Summary

Overall, the YIP project has achieved significant advancements in quantitative, spatially-resolved measurement capability for species and temperature at combustion conditions. At the beginning of the project, the LAI method had been demonstrated in 1D. The method has been evolved to perform volumetric and time-resolved measurements, providing novel capability to quantitatively examine combustion dynamics in a 3D domain. Advancements in dimensionality were enabled in part by deep learning methods and other data science tools that produced efficient image reconstructions. Additionally, the spectroscopic phenomena and characteristics of carbon monoxide, carbon dioxide, and methane have been revealed at high-pressures and temperatures for select infrared wavelength regions targeted for detection at extreme combustion conditions. Line mixing and line broadening were shown to be prominent at elevated gas densities, and these effects were quantified to enable laser absorption sensing over a wide range of conditions. Detailed models were developed to capture these spectroscopic effects and enable prediction at supercritical conditions. As discussed in this report, such line mixing effects were utilized to perform quantitative imaging of methane in 3D reacting flows, representing a combination of the laser absorption imaging and high-pressure spectroscopy advancements. Future work is expected to push LAI to even more extreme conditions (higher-pressures) and to the 4D domain relevant for turbulent combustion. Notably, the YIP project involved ten journal publications, three graduate students, and a postdoc, providing meaningful training opportunities and scientific impact.

References

[1] W. Cai and C. F. Kaminski, "Tomographic Absorption Spectroscopy for the study of Gas Dynamics and Reactive Flows," *Progress in Energy and Combustion Science*, vol. 59, pp. 1–31, 3 2017.

[2] J. R. Howell, M. P. Mengüç, K. Daun, and R. Siegel, "Inverse Problems in Radiative Transfer," in *Thermal Radiation Heat Transfer*, ch. 18, pp. 825–863, Boca Raton, FL: CRC Press, 7th ed., 2021.

[3] L. Ma, X. Li, S. T. Sanders, A. W. Caswell, S. Roy, D. H. Plemmons, and J. R. Gord, "50-kHz-rate 2D imaging of temperature and H2O concentration at the exhaust plane of a J85 engine using hyperspectral tomography," *Optics express*, vol. 21, pp. 1152–62, 1 2013.

[4] F. Stritzke, S. van der Kley, A. Feiling, A. Dreizler, and S. Wagner, "Ammonia concentration distribution measurements in the exhaust of a heavy duty diesel engine based on limited data absorption tomography," *Optics Express*, vol. 25, no. 7, p. 8180, 2017.

[5] K. J. Daun, S. J. Grauer, and P. J. Hadwin, "Chemical species tomography of turbulent flows: Discrete ill-posed and rank deficient problems and the use of prior information," *Journal of Quantitative Spectroscopy and Radiative Transfer*, vol. 172, pp. 58–74, 2016.

[6] K. J. Daun, K. A. Thomson, F. Liu, and G. J. Smallwood, "Deconvolution of axisymmetric flame properties using Tikhonov regularization," *Applied Optics*, vol. 45, p. 4638, 7 2006.

[7] J. Song, Y. Hong, G. Wang, and H. Pan, "Algebraic tomographic reconstruction of two-dimensional gas temperature based on tunable diode laser absorption spectroscopy," *Applied Physics B*, vol. 112, no. 4, pp. 529–537, 2013.

[8] C. Liu, L. Xu, J. Chen, Z. Cao, Y. Lin, and W. Cai, "Development of a fan-beam TDLAS-based tomographic sensor for rapid imaging of temperature and gas concentration," *Optics Express*, vol. 23, no. 17, p. 22494, 2015.

[9] C. Wei, K. K. Schwarm, D. I. Pineda, and R. M. Spearrin, "Volumetric laser absorption imaging of temperature, CO and CO2 in laminar flames using 3D masked Tikhonov regularization," *Combustion and Flame*, vol. 224, pp. 239–247, 2021.

[10] Y. Bao, R. Zhang, G. Enemali, Z. Cao, B. Zhou, H. McCann, and C. Liu, "Relative Entropy Regularized TDLAS Tomography for Robust Temperature Imaging," *IEEE Transactions on Instrumentation and Measurement*, vol. 70, 2021.

[11] N. A. Malarich and G. B. Rieker, "Resolving nonuniform temperature distributions with single-beam absorption spectroscopy. Part I: Theoretical capabilities and limitations," *Journal of Quantitative Spectroscopy and Radiative Transfer*, vol. 260, 2021.

[12] K. J. Daun, S. L. Waslander, and B. B. Tulloch, "Infrared species tomography of a transient flow field using Kalman filtering," *Applied Optics*, vol. 50, no. 6, pp. 891–900, 2011.

[13] S. J. Grauer, J. Emmert, S. T. Sanders, S. Wagner, and K. J. Daun, "Multiparameter gas sensing with linear hyperspectral absorption tomography," *Measurement Science and Technology*, vol. 30, p. 105401, 10 2019.

[14] J. D. Christopher, O. A. Doronina, D. Petrykowski, T. R. Hayden, C. Lapointe, N. T. Wimer, I. Grooms, G. B. Rieker, and P. E. Hamlington, "Flow parameter estimation using laser absorption spectroscopy and approximate Bayesian computation," *Experiments in Fluids*, vol. 62, no. 2, pp. 1–20, 2021.

[15] X. Liu, J. B. Jeffries, and R. K. Hanson, "Measurement of nonuniform temperature distributions using line-of-sight absorption spectroscopy," *AIAA Journal*, vol. 45, no. 2, pp. 411–419, 2007.

[16] L. H. Ma, L. Y. Lau, and W. Ren, "Non-uniform temperature and species concentration measurements in a laminar flame using multi-band infrared absorption spectroscopy," *Applied Physics B*, vol. 123, p. 83, 3 2017.

[17] D. Wen and Y. Wang, "Spatially and temporally resolved temperature measurements in counterflow flames using a single interband cascade laser," *Optics Express*, vol. 28, no. 25, p. 37879, 2020.

[18] D. Wu, K. Kim, G. El Fakhri, and Q. Li, "Iterative low-dose CT reconstruction with priors trained by artificial neural network," *IEEE Transactions on Medical Imaging*, vol. 36, no. 12, pp. 2479–2486, 2017.

[19] X. Zheng, I. Y. Chun, Z. Li, Y. Long, and J. A. Fessler, "Sparse-View X-Ray CT Reconstruction Using l1 Prior with Learned Transform," *arXiv*, 11 2017.

[20] T. Ren, M. F. Modest, A. Fateev, G. Sutton, W. Zhao, and F. Rusu, "Machine learning applied to retrieval of temperature and concentration distributions from infrared emission measurements," *Applied Energy*, vol. 252, p. 113448, 10 2019.

[21] J. Huang, H. Liu, and W. Cai, "Online in situ prediction of 3-D flame evolution from its history 2-D projections via deep learning," *Journal of Fluid Mechanics*, vol. 875, p. R2, 9 2019.

[22] Y. Jin, W. Zhang, Y. Song, X. Qu, Z. Li, Y. Ji, and A. He, "Three-dimensional rapid flame chemiluminescence tomography via deep learning," *Optics Express*, vol. 27, p. 27308, 9 2019.

[23] T. Ren, H. Li, M. F. Modest, and C. Zhao, "Efficient two-dimensional scalar fields reconstruction of laminar flames from infrared hyperspectral measurements with a machine learning approach," *Journal of Quantitative Spectroscopy and Radiative Transfer*, vol. 271, p. 107724, 9 2021.

[24] C. Wei, K. K. Schwarm, D. I. Pineda, and R. M. Spearrin, "Deep neural network inversion for 3D laser absorption imaging of methane in reacting flows," *Optics Letters*, vol. 45, p. 2447, 4 2020.

[25] Y. Jiang, J. Si, R. Zhang, G. Enemali, B. Zhou, H. McCann, and C. Liu, "CSTNet: A dual-branch convolutional network for imaging of reactive flows using chemical species tomography," *arXiv*, pp. 1–9, 2020.

[26] J. Huang, H. Liu, J. Dai, and W. Cai, "Reconstruction for limited-data nonlinear tomographic absorption spectroscopy via deep learning," *Journal of Quantitative Spectroscopy and Radiative Transfer*, vol. 218, pp. 187–193, 2018.

[27] J. Si, G. Li, Y. Cheng, R. Zhang, G. Enemali, and C. Liu, "Hierarchical Temperature Imaging Using Pseudo-Inversed Convolutional Neural Network Aided TDLAS Tomography," *arXiv*, 6 2021.

[28] C. Wei, D. I. Pineda, C. S. Goldenstein, and R. M. Spearrin, "Tomographic laser absorption imaging of combustion species and temperature in the mid-wave infrared," *Optics Express*, vol. 26, p. 20944, 8 2018.

[29] R. J. Tancin, R. M. Spearrin, and C. S. Goldenstein, "2D mid-infrared laser-absorption imaging for tomographic reconstruction of temperature and carbon monoxide in laminar flames," *Optics Express*, vol. 27, p. 14184, 5 2019.

[30] K. K. Schwarm, C. Wei, D. I. Pineda, and R. M. Spearrin, "Time-resolved laser absorption imaging of ethane at 2 kHz in unsteady partially premixed flames," *Applied Optics*, vol. 58, p. 5656, 7 2019.

[31] R. M. Spearrin, C. S. Goldenstein, I. A. Schultz, J. B. Jeffries, and R. K. Hanson, "Simultaneous sensing of temperature, CO, and CO2 in a scramjet combustor using quantum cascade laser absorption spectroscopy," *Applied Physics B*, vol. 117, pp. 689–698, 11 2014.

[32] C. S. Goldenstein, R. M. Spearrin, J. B. Jeffries, and R. K. Hanson, "Infrared laser-absorption sensing for combustion gases," *Progress in Energy and Combustion Science*, vol. 60, pp. 132–176, 5 2017.

[33] L. Rothman, I. Gordon, R. Barber, H. Dothe, R. Gamache, A. Goldman, V. Perevalov, S. Tashkun, and J. Tennyson, "HITEMP, the High-Temperature Molecular Spectroscopic Database," *Journal of Quantitative Spectroscopy and Radiative Transfer*, vol. 111, pp. 2139–2150, 10 2010.

[34] K. B. McGrattan, R. J. McDermott, C. G. Weinschenk, and G. P. Forney, "Fire Dynamics Simulator, Technical Reference Guide, Sixth Edition," Tech. Rep. Special Publication (NIST SP) - 1018, National Institute of Standards and Technology, Gaithersburg, MD, 2016.

[35] C. K. Law, *Combustion Physics*. New York: Cambridge University Press, 2006.

[36] D. I. Pineda, L. Paxton, N. Perakis, C. Wei, S. Luna, H. Kahouli, M. Ihme, F. N. Egolfopoulos, and R. M. Spearrin, "Carbon oxidation in turbulent premixed jet flames: A comparative experimental and numerical study of ethylene, n-heptane, and toluene," *Combustion and Flame*, vol. 221, pp. 371–383, 11 2020.

[37] M. Mann, C. Jainski, M. Euler, B. Böhm, and A. Dreizler, "Transient flame-wall interactions: Experimental analysis using spectroscopic temperature and CO concentration measurements," *Combustion and Flame*, vol. 161, no. 9, pp. 2371–2386, 2014.

[38] T. Neill, D. Judd, E. Veith, and D. Rousar, "Practical uses of liquid methane in rocket engine applications," *Acta Astronautica*, vol. 65, no. 5-6, pp. 696–705, 2009.

[39] F. A. Bendana, D. D. Lee, S. A. Schumaker, S. A. Danczyk, and R. M. Spearrin, "Cross-band infrared laser absorption of carbon monoxide for thermometry and species sensing in high-pressure rocket flows," *Applied Physics B*, vol. 125, p. 204, 11 2019.

[40] R. Sur, S. Wang, K. Sun, D. F. Davidson, J. B. Jeffries, and R. K. Hanson, "High-sensitivity interference-free diagnostic for measurement of methane in shock tubes," *Journal of Quantitative Spectroscopy and Radiative Transfer*, vol. 156, pp. 80–87, 2015.

[41] A. Karion, C. Sweeney, G. Pétron, G. Frost, R. Michael Hardesty, J. Kofler, B. R. Miller, T. Newberger, S. Wolter, R. Banta, A. Brewer, E. Dlugokencky, P. Lang, S. A. Montzka, R. Schnell, P. Tans, M. Trainer, R. Zamora, and S. Conley, "Methane emissions estimate from airborne measurements over a western United States natural gas field," *Geophysical Research Letters*, vol. 40, no. 16, pp. 4393–4397, 2013.

[42] O. Schneising, J. P. Burrows, R. R. Dickerson, M. Buchwitz, M. Reuter, and H. Bovensmann, "Remote sensing of fugitive methane emissions from oil and gas production in North American tight geologic formations," *Earth's Future*, vol. 2, no. 10, pp. 548–558, 2014.

[43] D. J. Jacob, A. J. Turner, J. D. Maasakkers, J. Sheng, K. Sun, X. Liu, K. Chance, I. Aben, J. McKeever, and C. Frankenberg, "Satellite observations of atmospheric methane and their value for quantifying methane emissions," *Atmospheric Chemistry and Physics*, vol. 16, no. 22, pp. 14371–14396, 2016.

[44] M. G. Tomasko, B. Bézard, L. Doose, S. Engel, and E. Karkoschka, "Measurements of methane absorption by the descent imager/spectral radiometer (DISR) during its descent through Titan's atmosphere," *Planetary and Space Science*, vol. 56, no. 5, pp. 624–647, 2008.

[45] E. Karkoschka and M. G. Tomasko, "Methane absorption coefficients for the jovian planets from laboratory, Huygens, and HST data," *Icarus*, vol. 205, no. 2, pp. 674–694, 2010.

[46] R. Nassar and P. Bernath, "Hot methane spectra for astrophysical applications," *Journal of Quantitative Spectroscopy and Radiative Transfer*, vol. 82, pp. 279–292, 11 2003.

[47] M. R. Swain, G. Vasisht, and G. Tinetti, "The presence of methane in the atmosphere of an extrasolar planet," *Nature*, vol. 452, no. 7185, pp. 329–331, 2008.

[48] S. E. M. Fletcher and H. Schaefer, "Rising methane: A new climate challenge," *Science*, vol. 364, no. 6444, pp. 932–933, 2019.

[49] G. Plant, E. A. Kort, C. Floerchinger, A. Gvakharia, I. Vimont, and C. Sweeney, "Large Fugitive Methane Emissions From Urban Centers Along the U.S. East Coast," *Geophysical Research Letters*, vol. 46, no. 14, pp. 8500–8507, 2019.

[50] V. Nagali, S. I. Chou, D. S. Baer, R. K. Hanson, and J. Segall, "Tunable diode-laser absorption measurements of methane at elevated temperatures," *Applied Optics*, vol. 35, no. 21, p. 4026, 1996.

[51] V. Ebert, T. Fernholz, C. Giesemann, H. Pitz, H. Teichert, J. Wolfrum, and H. Jaritz, "Simultaneous diode-laser-based in situ detection of multiple species and temperature in a gas-fired power plant," *Proceedings of the Combustion Institute*, vol. 28, no. 1, pp. 423–430, 2000.

[52] R. Sur, K. Sun, J. B. Jeffries, and R. K. Hanson, "Multi-species laser absorption sensors for in situ monitoring of syngas composition," *Applied Physics B*, vol. 115, pp. 9–24, 4 2014.

[53] S. H. Pyun, J. Cho, D. F. Davidson, and R. K. Hanson, "Interference-free mid-IR laser absorption detection of methane," *Measurement Science and Technology*, vol. 22, no. 2, 2011.

[54] M. B. Sajid, T. Javed, and A. Farooq, "High-temperature measurements of methane and acetylene using quantum cascade laser absorption near 8μm," *Journal of Quantitative Spectroscopy and Radiative Transfer*, vol. 155, pp. 66–74, 2015.

[55] M. B. Sajid, T. Javed, and A. Farooq, "Shock tube/laser absorption measurements of methane, acetylene and ethylene during the pyrolysis of n-pentane and iso-pentane," *Combustion and Flame*, vol. 164, pp. 1–9, 2016.

[56] G. Zhang, K. Khabibullin, and A. Farooq, "An IH-QCL based gas sensor for simultaneous detection of methane and acetylene," *Proceedings of the Combustion Institute*, vol. 37, no. 2, pp. 1445–1452, 2019.

[57] M. Ghysels, S. Vasilchenko, D. Mondelain, S. Béguier, S. Kassi, and A. Campargue, "Laser absorption spectroscopy of methane at 1000K near 1.7 µm: A validation test of the spectroscopic databases," *Journal of Quantitative Spectroscopy and Radiative Transfer*, vol. 215, pp. 59–70, 2018.

[58] A. Borysov, J. P. Champion, U. G. Jørgensen, and C. Wenger, "Towards simulation of high temperature methane spectra," *Molecular Physics*, vol. 100, pp. 3585–3594, 11 2002.

[59] R. J. Hargreaves, I. E. Gordon, M. Rey, A. V. Nikitin, V. G. Tyuterev, R. V. Kochanov, and L. S. Rothman, "An Accurate, Extensive, and Practical Line List of Methane for the HITEMP Database," *The Astrophysical Journal Supplement Series*, vol. 247, no. 2, p. 55, 2020.

[60] J. M. Hartmann, C. Boulet, and D. Robert, *Collisional Effects on Molecular Spectra*. Elsevier, 2008.

[61] D. C. Benner, C. P. Rinsland, V. M. Devi, M. A. H. Smith, and D. Atkins, "A Multispectrum Least Fitting Technique," *Journal of Quantitative Spectroscopy and Radiative Transfer*, vol. 53, no. 6, pp. 705–721, 1995.

[62] A. Pine, "Line mixing sum rules for the analysis of multiplet spectra," *Journal of Quantitative Spectroscopy and Radiative Transfer*, vol. 57, pp. 145–155, 2 1997.

[63] A. Pine, "N2 and Ar broadening and line mixing in the P and R branches of the v3 band of CH4," *Journal of Quantitative Spectroscopy and Radiative Transfer*, vol. 57, pp. 157–176, 2 1997.

[64] D. Pieroni, Nguyen-Van-Thanh, C. Brodbeck, C. Claveau, A. Valentin, J. M. Hartmann, T. Gabard, J.-P. Champion, D. Bermejo, and J.-L. Domenech, "Experimental and theoretical study of line mixing in methane spectra. I. The N2-broadened $\nu 3$ band at room temperature," *The Journal of Chemical Physics*, vol. 110, pp. 7717–7732, 4 1999.

[65] D. Pieroni, Nguyen-Van-Thanh, C. Brodbeck, J.-M. Hartmann, T. Gabard, J.-P. Champion, D. Bermejo, J.-L. Domenech, C. Claveau, A. Valentin, M. V. Tonkov, I. M. Grigoriev, and R. Le Doucen, "Experimental and theoretical study of line mixing in methane spectra. II. Influence of the collision partner (He and Ar) in the v3 IR band," *The Journal of Chemical Physics*, vol. 111, pp. 6850–6863, 10 1999.

[66] A. S. Pine and T. Gabard, "Speed-dependent broadening and line mixing in CH4 perturbed by Ar and N2 from multispectrum fits," *Journal of Quantitative Spectroscopy and Radiative Transfer*, vol. 66, no. 1, pp. 69–92, 2000.

[67] I. M. Grigoriev, N. N. Filippov, M. V. Tonkov, T. Gabard, and R. Le Doucen, "Estimation of line parameters under line mixing effects: The v3 band of CH4 in helium," *Journal of Quantitative Spectroscopy and Radiative Transfer*, vol. 69, no. 2, pp. 189–204, 2001.

[68] I. M. Grigoriev, N. N. Filippov, M. V. Tonkov, J. P. Champion, T. Gabard, and R. Le Doucen, "Line parameters and shapes of high clusters: R branch of the $\nu 3$ band of CH4 in He mixtures," *Journal of Quantitative Spectroscopy and Radiative Transfer*, vol. 74, no. 4, pp. 431–443, 2002.

[69] A. S. Pine and T. Gabard, "Multispectrum fits for line mixing in the v3 band Q branch of methane," *Journal of Molecular Spectroscopy*, vol. 217, no. 1, pp. 105–114, 2003.

[70] H. Tran, P. M. Flaud, T. Gabard, F. Hase, T. von Clarmann, C. Camy-Peyret, S. Payan, and J. M. Hartmann, "Model, software and database for line-mixing effects in the $\nu 3$ and $\nu 4$ bands of CH4 and tests using laboratory and planetary measurements-I: N2 (and air) broadenings and the earth atmosphere," *Journal of Quantitative Spectroscopy and Radiative Transfer*, vol. 101, no. 2, pp. 284–305, 2006.

[71] H. Tran, P. M. Flaud, T. Fouchet, T. Gabard, and J. M. Hartmann, "Model, software and database for line-mixing effects in the $\nu 3$ and $\nu 4$ bands of CH4 and tests using laboratory and planetary measurements-II: H2 (and He) broadening and the atmospheres of Jupiter and Saturn," *Journal of Quantitative Spectroscopy and Radiative Transfer*, vol. 101, no. 2, pp. 306–324, 2006.

[72] D. Mondelain, S. Payan, W. Deng, C. Camy-Peyret, D. Hurtmans, and A. W. Mantz, "Measurement of the temperature dependence of line mixing and pressure broadening parameters between 296 and 90 K in the $\nu 3$ band of 12CH4 and their influence on atmospheric methane retrievals," *Journal of Molecular Spectroscopy*, vol. 244, no. 2, pp. 130–137, 2007.

[73] M. Ghysels, L. Gomez, J. Cousin, H. Tran, N. Amarouche, A. Engel, I. Levin, and G. Durry, "Temperature dependences of air-broadening, air-narrowing and line-mixing coefficients of the methane $\nu 3$ R(6) manifold lines—Application to in-situ measurements of atmospheric methane," *Journal of Quantitative Spectroscopy and Radiative Transfer*, vol. 133, pp. 206–216, 2014.

[74] J. Mendonca, K. Strong, K. Sung, V. M. Devi, G. C. Toon, D. Wunch, and J. E. Franklin, "Using high-resolution laboratory and ground-based solar spectra to assess CH4 absorption coefficient calculations," *Journal of Quantitative Spectroscopy and Radiative Transfer*, vol. 190, pp. 48–59, 2017.

[75] V. M. Devi, D. C. Benner, R. R. Gamache, H. Tran, M. A. H. Smith, and R. L. Sams, "Multispectrum analysis of air-broadened spectra in the $\nu 3$ Q branch of 12CH4," *Journal of Quantitative Spectroscopy and Radiative Transfer*, vol. 206, pp. 409–429, 2018.

[76] A. Pine, "Speed-dependent line mixing in the $\nu 3$ band Q branch of methane," *Journal of Quantitative Spectroscopy and Radiative Transfer*, vol. 224, pp. 62–77, 2 2019.

[77] P. Rosenkranz, "Shape of the 5 mm oxygen band in the atmosphere," *IEEE Transactions on Antennas and Propagation*, vol. 23, pp. 498–506, 7 1975.

[78] G. Millot, B. Lavorel, and J. I. Steinfeld, "Collisional broadening, line shifting, and line mixing in the stimulated Raman $2\nu 2$ Q branch of CH4," *The Journal of Chemical Physics*, vol. 95, pp. 7938–7946, 12 1991.

[79] G. J. Rosasco, L. A. Rahn, W. S. Hurst, R. E. Palmer, and S. M. Dohne, "Measurement and prediction of Raman Q -branch line self-broadening coefficients for CO from 400 to 1500 K," *The Journal of Chemical Physics*, vol. 90, pp. 4059–4068, 4 1989.

[80] F. A. Bendana, D. D. Lee, C. Wei, D. I. Pineda, and R. M. Spearrin, "Line mixing and broadening in the v(1→3) first overtone bandhead of carbon monoxide at high temperatures and high pressures," *Journal of Quantitative Spectroscopy and Radiative Transfer*, vol. 239, p. 106636, 12 2019.

[81] D. D. Lee, F. A. Bendana, A. P. Nair, D. I. Pineda, and R. M. Spearrin, "Line mixing and broadening of carbon dioxide by argon in the ν3 bandhead near 4.2 μm at high temperatures and high pressures," *Journal of Quantitative Spectroscopy and Radiative Transfer*, vol. 253, p. 107135, 9 2020.

[82] J. C. Polanyi and K. B. Woodall, "Mechanism of rotational relaxation," *The Journal of Chemical Physics*, vol. 56, no. 4, pp. 1563–1572, 1972.

[83] M. L. Koszykowski, L. A. Rahn, R. E. Palmer, and M. E. Coltrin, "Theoretical and experimental studies of high-resolution inverse Raman spectra of N2 at 1-10 atm," *Journal of Physical Chemistry*, vol. 91, pp. 41–46, 1 1987.

[84] J. Li, Y. Du, Z. Peng, and Y. Ding, "Measurements of spectroscopic parameters of CO2 transitions for Voigt, Rautian, galatry and speed-dependent voigt profiles near 1.43 μm using the WM-DAS method," *Journal of Quantitative Spectroscopy and Radiative Transfer*, vol. 224, pp. 197–205, 2019.

[85] J. Li, Z. Peng, and Y. Ding, "Wavelength modulation-direct absorption spectroscopy combined with improved experimental strategy for measuring spectroscopic parameters of H2O transitions near 1.39μm," *Optics and Lasers in Engineering*, vol. 126, no. August 2019, p. 105875, 2020.

[86] E. W. Smith, "Absorption and dispersion in the O2 microwave spectrum at atmospheric pressures," *The Journal of Chemical Physics*, vol. 74, pp. 6658–6673, 6 1981.

[87] A. Ben-Reuven, "Impact Broadening of Microwave Spectra," *Physical Review*, vol. 145, pp. 7–22, 5 1966.

[88] J. I. Steinfeld, P. Ruttenberg, G. Millot, G. Fanjoux, and B. Lavorel, "Scaling laws for inelastic collision processes in diatomic molecules," *The Journal of Physical Chemistry*, vol. 95, pp. 9638–9647, 11 1991.

[89] K. K. Schwarm, H. Q. Dinh, C. S. Goldenstein, D. I. Pineda, and R. M. Spearrin, "High-pressure and high-temperature gas cell for absorption spectroscopy studies at wavelengths up to 8 μm," *Journal of Quantitative Spectroscopy and Radiative Transfer*, vol. 227, pp. 145–151, 4 2019.

[90] L. R. Brown, K. Sung, D. C. Benner, V. M. Devi, V. Boudon, T. Gabard, C. Wenger, A. Campargue, O. Leshchishina, S. Kassi, D. Mondelain, L. Wang, L. Daumont, L. Régalia, M. Rey, X. Thomas, V. G. Tyuterev, O. M. Lyulin, A. V. Nikitin, H. M. Niederer, S. Albert, S. Bauerecker, M. Quack, J. J. O'Brien, I. E. Gordon, L. S. Rothman, H. Sasada, A. Coustenis, M. A. Smith, T. Carrington, X. G. Wang, A. W. Mantz, and P. T. Spickler, "Methane line parameters in the HITRAN2012 database," *Journal of Quantitative Spectroscopy and Radiative Transfer*, vol. 130, pp. 201–219, 2013.

[91] D. I. Pineda, F. A. Bendana, K. K. Schwarm, and R. M. Spearrin, "Multi-isotopologue laser absorption spectroscopy of carbon monoxide for high-temperature chemical kinetic studies of fuel mixtures," *Combustion and Flame*, vol. 207, pp. 379–390, 9 2019.

[92] J. D. Anderson, *Modern Compressible Flow*. McGraw-Hill, 3rd ed., 2002.

[93] M. F. Campbell, S. Wang, C. S. Goldenstein, R. M. Spearrin, A. M. Tulgestke, L. T. Zaczek, D. F. Davidson, and R. K. Hanson, "Constrained reaction volume shock tube study of n -heptane oxidation: Ignition delay times and time-histories of multiple species and temperature," *Proceedings of the Combustion Institute*, vol. 35, no. 1, pp. 231–239, 2015.

[94] D. York, N. M. Evensen, M. L. Martinez, and J. De Basabe Delgado, "Unified equations for the slope, intercept, and standard errors of the best straight line," *American Journal of Physics*, vol. 72, pp. 367–375, 3 2004.

[95] D. Lisak, J. T. Hodges, and R. Ciuryło, "Comparison of semiclassical line-shape models to rovibrational H2O spectra measured by frequency-stabilized cavity ring-down spectroscopy," *Physical Review A - Atomic, Molecular, and Optical Physics*, vol. 73, no. 1, pp. 1–13, 2006.

[96] J. Li, Y. Du, Y. Ding, and Z. Peng, "Experimental and simulated study of line-shape models for measuring spectroscopic parameters using the WM-DAS method — part I: Collisional broadening and absorption coefficients of H2O-Ar system," *Journal of Quantitative Spectroscopy and Radiative Transfer*, vol. 254, p. 107216, 2020.

[97] C. S. Goldenstein and R. K. Hanson, "Diode-laser measurements of linestrength and temperature-dependent lineshape parameters for H2O transitions near 1.4μm using Voigt, Rautian, Galatry, and speed-dependent Voigt profiles," *Journal of Quantitative Spectroscopy and Radiative Transfer*, vol. 152, pp. 127–139, 2015.

[98] L. Wehr, W. Meier, P. Kutne, and C. Hassa, "Single-pulse 1D laser Raman scattering applied in a gas turbine model combustor at elevated pressure," *Proceedings of the Combustion Institute*, vol. 31, pp. 3099–3106, 1 2007.

[99] T. Kamimoto, Y. Deguchi, N. Zhang, R. Nakao, T. Takagi, and J. Z. Zhang, "Real-time 2D concentration measurement of CH4 in oscillating flames using CT tunable diode laser absorption spectroscopy," *Journal of Applied Nonlinear Dynamics*, vol. 4, no. 3, pp. 295–303, 2015.

[100] S. A. Tsekenis, D. Wilson, M. Lengden, J. Hyvönen, J. Leinonen, A. Shah, Andersson, and H. McCann, "Towards in-cylinder chemical species tomography on large-bore IC engines with pre-chamber," *Flow Measurement and Instrumentation*, vol. 53, pp. 116–125, 2017.

[101] R. Villarreal and P. L. Varghese, "Frequency-resolved absorption tomography with tunable diode lasers," *Applied Optics*, vol. 44, no. 31, pp. 6786–6795, 2005.

[102] P. Nau, J. Koppmann, A. Lackner, K. Kohse-Höinghaus, and A. Brockhinke, "Quantum cascade laser-based MIR spectrometer for the determination of CO and CO2 concentrations and temperature in flames," *Applied Physics B: Lasers and Optics*, vol. 118, no. 3, pp. 361–368, 2015.

[103] X. Liu, G. Zhang, Y. Huang, Y. Wang, and F. Qi, "Two-dimensional temperature and carbon dioxide concentration profiles in atmospheric laminar diffusion flames measured by mid-infrared direct absorption spectroscopy at 4.2 μm," *Applied Physics B*, vol. 124, p. 61, 4 2018.

[104] C. Wei, D. I. Pineda, L. Paxton, F. N. Egolfopoulos, and R. M. Spearrin, "Mid-infrared laser absorption tomography for quantitative 2D thermochemistry measurements in premixed jet flames," *Applied Physics B*, vol. 124, p. 123, 6 2018.

[105] J. Li, A. P. Nair, K. K. Schwarm, D. I. Pineda, and R. Mitchell Spearrin, "Temperature-dependent line mixing in the R-branch of the v3 band of methane," *Journal of Quantitative Spectroscopy and Radiative Transfer*, vol. 255, p. 107271, 11 2020.

[106] K. Daun, "Infrared species limited data tomography through Tikhonov reconstruction," *Journal of Quantitative Spectroscopy and Radiative Transfer*, vol. 111, pp. 105–115, 1 2010.

[107] F. Nicolas, V. Todoroff, A. Plyer, G. Le Besnerais, D. Donjat, F. Micheli, F. Champagnat, P. Cornic, and Y. Le Sant, "A direct approach for instantaneous 3D density field reconstruction from background-oriented schlieren (BOS) measurements," *Experiments in Fluids*, vol. 57, no. 1, pp. 1–21, 2016.

[108] A. Guha and I. M. Schoegl, "Tomographic Imaging of Flames: Assessment of Reconstruction Error Based on Simulated Results," *Journal of Propulsion and Power*, vol. 30, pp. 350–359, 3 2014.

[109] K. J. Daun, S. J. Grauer, and P. J. Hadwin, "Chemical species tomography of turbulent flows: Discrete ill-posed and rank deficient problems and the use of prior information," *Journal of Quantitative Spectroscopy and Radiative Transfer*, vol. 172, pp. 58–74, 2016.